Mesospheric water vapor; Variability at different timescales observed by ground-based microwave spectroscopy.

Dissertation

zur

Erlangung des akademischen Grades

doctor rerum naturalium (Dr. rer. nat.)

der Mathematisch-Naturwissenschaftlichen Fakultät der Universität Rostock

vorgelegt von

Kristofer Hallgren, geb. am 19.07.1979 in Malmö

aus Malmö, Schweden

Rostock, 29.06.2010

Contents

Summary

Water vapor is a key element in Earth's atmosphere - it is an important green-house gas and plays a major role in the middle atmospheric chemistry. Knowledge of the long term behavior of atmospheric water vapor is therefore of importance. There are indications of a decrease in the water vapor levels in the atmosphere, but to what extent is still a matter of debate. Furthermore, short term behavior such as the tidal variability of water vapor and dynamical events such as sudden stratospheric warmings are still largely unexplored.

A new, ground-based, microwave spectrometer measuring both vertical and horizontal polarization has been developed. It is based on the successful WASPAM instrument but has a much higher sensitivity. Currently, four instruments have been manufactured and are spread over Northern Europe (ALOMAR in Norway and Kühlungsborn, Katlenburg-Lindau and Zugspitze in Germany). A short description of the instrument as well as design choices and calibration are discussed in the thesis. Furthermore, a comparison which shows good agreement to satellite data is also included.

The dataset from the new instrument is still limited but it could be merged with older data from WASPAM. This allowed an analysis of the long term behavior of water vapor above ALOMAR. The full dataset covers more than a solar cycle and a middle atmospheric water vapor climatology for ALOMAR was compiled.

The increased sensitivity of the new instrument greatly improved the temporal resolution of the water vapor retrievals. The better time resolution make it is possible to resolve the temporal behavior of dynamical events such as sudden stratospheric warmings to a much higher degree than before.

One of the design goals of the instrument was to be able to observe a tidal behavior of water vapor distribution. The long chemical lifetime of water vapor in the middle atmosphere imply that such behavior is caused by transport processes. These tides have, for the first time, been observed with a ground-based microwave instrument. Despite the short dataset covering less than two years it is possible to draw some conclusions on the seasonal behavior of the tides.

The new instrument and the growing dataset has opened many doors into new and exciting science. Although the synergic advantages of several identical instruments spread over Europe are still largely unexplored the initial results from each instrument are promising.

1 Introduction

1.1 Motivation

The middle atmosphere is an intriguing part of the Earth's atmosphere. It is usually defined to encompass the stratosphere and mesosphere (approximately between 12 km and 85 km), although sometimes the lower part of the thermosphere is also included which would extend the upper limit to ~100 km. Our understanding of the region have expanded greatly in recent years, but a lot of processes are still not fully understood. Its complexity makes modeling hard and increase the need for reliable observations.

In order to better resolve the short term variability of middle atmospheric water vapor a new ground-based microwave spectrometer has been developed. It is based on an earlier successful instrument, WASPAM[1]. Water vapor is a key component in the middle atmospheric chemistry and thus important for the general behavior in that region. It is the most important source of hydrogen radicals, which are formed in the mesosphere by photo-dissociation of water caused by the solar Lyman-α radiation. Phenomena specific for the polar mesosphere such as noctilucent clouds and polar mesospheric summer echoes are also strongly influenced by the available amounts of water vapor. In order to fully understand these a better understanding of the dynamics controlling the water vapor is needed.

There is a general scientific agreement on the trend of many parameters in the middle atmosphere, among others the amount of ozone, methane and mean temperatures. However there are also parameters where such a consensus have not been reached. Laštovička (2009) and Garcia et al. (2007) identify the long term change of water vapor as such a problematic issue with inconsistencies between observational datasets and model results. This could indicate that we do still not fully understand the dynamics governing the water vapor in the region. Garcia et al. (2007) explain this by sporadic and/or low-frequency events such as volcanic eruptions and the El Niño-Southern oscillation on the middle atmospheric amount of water vapor. Such events and long-term oscillations could influences shorter observational datasets. The longest observational dataset that exists today ranges back to 1980 and consist of hygrosonde measurements done over Boulder, Colorado. For global coverage there is the HALOE instrument onboard the NASA UARS mission which dates back to 1992. Another troublesome issue is the fact that there are also small differences between the observational datasets. The polar regions play an important role in the dynamics of the middle atmosphere and up until now there has been a lack of a long term, ground-based, data-set.

Water vapor has a long chemical lifetime in the middle atmosphere and variations

[1] Wasserdampf und Spurengasmessungen in der Atmosphäre mit Mikrowellen

in the distribution are assumed to be caused by tidal transport mechanisms. The new instrument is more sensitive than the former and it is expected to be able to resolve variabilities on the order of a couple of hours. Study of tides in the middle atmosphere is important for a variety of reasons. The amplitudes are among the largest natural oscillations in the atmosphere (Manson and Meek 1986), although being seasonally variable they still present a very regular and persistent wavelike behavior. It has been shown that they have a significant impact on the distribution of atmospheric constituents (Shepherd et al. 1998), and by modulating the flux of propagating gravity waves they can affect the momentum balance in the middle atmosphere. Tidal structures in the middle atmospheric region are very complex, and to correctly model them a thorough understanding of the dynamical and chemical processes in the region is needed. As opposed to measurements of the tidal components of the wind where each component (zonal, meridional and vertical) is separately analyzed the water vapor observations are sensitive to the sum of these wind fields.

1.2 Outline of the thesis

The aim of the thesis is to describe and analyze observations of the water vapor distribution in the middle atmosphere at different timescales. In Chapter 2 a short, introductory, background to microwave spectroscopy and the middle atmosphere will be given. Thereafter a description of the instrument follows, the hardware in Chapter 3 and a discussion on the data retrieval in Chapter 4. Although a substantial part of the thesis time have been spent on instrument calibration, optimization and software development these chapters are cut relatively short.

The second part of the thesis is the actual analysis of the observational data. For the short term behavior and high time-resolution analysis of sudden stratospheric warmings data from the new instrument are used. Such a warming was analyzed with the old instrument by Seele and Hartogh (2000) although at the time there was only observations available from one location. A brief comparison of the behavior of water vapor at a polar (ALOMAR) and mid-latitude (Zugspitze) location is also carried out. This comparison is constrained by the small dataset available from the mid-latitude location but show interesting differences nevertheless. The general behavior of the water vapor distribution is covered in Chapter 5 whereas Chapter 6 focus on the tidal behavior of the water vapor.

The last chapter, Chapter 7, summarizes the results and offer a brief outlook to possible future investigations using the expanding dataset.

2 Introductory physics

The work conducted for this thesis demanded knowledge of two separate disciplines; initially microwave spectroscopy and the involved instrumentation and thereafter atmospheric physics with a focus on the middle atmosphere in order to correctly analyze the retrieved data. In this first chapter I will therefore give a short introduction to the most important concepts relevant to each field. The first part will touch upon the relations and physics that enable us to retrieve a vertical distribution profile of water vapor in the atmosphere by means of microwave spectroscopy. In the next part I will introduce some terms and definitions which are used in Chapter 3 to describe the new instrument. The last part is intended to give the reader a general background to the middle atmosphere, and to present some important processes in the middle atmosphere relevant for water vapor and transport of tracers.

2.1 Radiative transfer

Classical radiative transfer theory was originally developed by Chandrasekhar (1960) and describes propagation of electromagnetic radiation in a general sense, taking into account absorption, scattering and emission. The theory is based on the description of the specific intensity, $\mathcal{I}_\nu(s)$, and its transfer equation for a point s,

$$\frac{d\mathcal{I}_\nu(s)}{ds} = -\mathcal{I}_\nu(s)\alpha_\nu(s) + S_\nu(s), \tag{2.1}$$

where α_ν is the absorption coefficient and S_ν is the source term. For an emitter in local thermodynamic equilibrium the source term in Equation 2.1 can be rewritten as:

$$S_\nu(s) = \alpha_\nu(s)B_\nu(s), \tag{2.2}$$

where $B_\nu(s)$ is the radiation by a black-body in thermal equilibrium. According to the Planck function it can be described by:

$$B_\nu(T) = \frac{2h\nu^3}{c^2}\frac{1}{\exp(\frac{h\nu}{kT}) - 1}, \tag{2.3}$$

where h denotes Planck's constant, ν the frequency, c the speed of light, k Boltzmann's constant, and T the temperature of the radiating body. Equation 2.1 can now be written as:

$$\frac{d\mathcal{I}_\nu(s)}{ds} = \alpha_\nu(s)(B_\nu(s) - \mathcal{I}_\nu(s)) \tag{2.4}$$

2.1.1 Forward modeling

In order to be able to invert a retrieved spectrum to a vertical water vapor distribution profile a forward model is needed. The task of the model is to accurately describe how a given water vapor distribution profile, in a given atmosphere, would translate into a spectral line. The model used here was initially described in Jarchow (1998) and has been successfully compared to other models[1]. Furthermore, the model has been successfully applied to earlier datasets, for example (Hartogh and Jarchow 1995b, Hartogh et al. 2004, Seele and Hartogh 1999, 2000) and Sonnemann et al. (2008).

In the case of water vapor emission at 22.235 GHz the atmosphere can be assumed to be in local thermodynamical equilibrium. The emission line is a pure rotational line and below ≈100 km its distribution controlled by kinetic collisions which are far more energetic than the weak rotational transition (Curtis and Goody 1956). Additionally, the impact of scattering depends on the particle size and wavelength of radiation, and can be ignored when $2\pi r \ll \lambda$, where r marks the radius of the scattering particle and λ the wavelength[2]. The inequality hold for most of the microwave region and scattering can generally be ignored (Janssen 1993). Thus α in Equation 2.1 can be described as a scalar parameter dependent on the loss of radiation energy to the medium.

2.1.1.1 Discretization of the radiative transfer equation

As discussed in the Section 2.1.1, for water vapor at 22.235 GHz the Equation 2.4 is a valid equation for the involved radiative transfer. Thus for an arbitrary point s along the path it can be written as:

$$\mathcal{I}_\nu(s) = \mathcal{I}_\nu(s_0)\exp(-\tau(s_0, s)) + \int_{s_0}^{s} B_\nu(s')\exp(-\tau(s', s))\alpha ds', \tag{2.5}$$

where τ is the optical depth. For practical reasons the radiative transfer equation (Eq. 2.5) is linearized in the forward model. By convention the measuring device is assumed to be located at the origin, $s = 0$. At the outer boundary, $s = s_0$, the intensity is given by $\mathcal{I}_\nu(s_0)$. The distance over which the intensity is integrated is denoted by Δs_i $(i = 1, 2, 3 \ldots, m)$ and represent one atmospheric layer. The temperature, T_i, and absorption, α_i are treated as constants within each atmospheric layer. Then the optical depth can be described by:

$$\tau(s_i, s_m) = \int_{s_i}^{s_m} ds''\alpha(s'') = \sum_{k=i+1}^{m} \alpha_k \Delta s_k. \tag{2.6}$$

[1]The results can be found here `http://wvms.nrl.navy.mil/NDSC/ndsc.html`

[2]It should however be noted that although there is no appreciable scattering by hydrometeors they can absorb a large portion of the radiation.

Using Equation 2.6, the right-hand integral in Equation 2.5 can be calculated for each layer[3]:

$$\int_{s_{i-1}}^{s_i} B(s')\exp(-\tau(s',s))\alpha ds' = B\alpha\exp(-\tau(s_i,s_m))\int_{s_{i-1}}^{s_i} ds'\exp(-\alpha\int_{s'}^{s_i} ds'') \quad (2.7a)$$

$$= B\alpha\exp(-\tau(s_i,s_m))\int_{s_{i-1}}^{s_i} ds'\exp(-\alpha(s_i-s')) \quad (2.7b)$$

$$= B\underbrace{(1-exp(-\alpha_i\cdot(s_i-s_{i-1})))}_{(1-exp(-\alpha_i\Delta_{s_i})}\exp(-\tau(s_i,s_m)) \quad (2.7c)$$

Thus the linearized radiative transfer equation for m layers can be written as:

$$\mathcal{I}(s_m) = \mathcal{I}(s_0)\exp(-\tau(s_0,s_m)) + \sum_{i=1}^{m} B(1-exp(-\alpha_i\Delta_{s_i}))\exp(-\tau(s_i,s_m)). \quad (2.8)$$

In the case of optically thin layers, *i.e.* $\alpha_i\Delta s_i \ll 1$, and no self absorption in the line ($\tau \approx 0$), Equation 2.8 can be further reduced to:

$$\mathcal{I}(s_m) = \mathcal{I}(s_0) + \sum_{i=1}^{m} B\alpha_i\Delta s_i, \quad (2.9)$$

where $\mathcal{I}(s_0)$ is the radiation at the beginning of the path. In the case of ground-based remote sensing of the atmosphere $\mathcal{I}(s_0)$ is the cosmic background radiation, a constant term which can be accounted for in the inversion, see Section 4.1.3. Equation 2.9 can then be rewritten in vector form. Using the common notation from Rodgers (1976) Equation 2.9 becomes:

$$\boldsymbol{y} = \boldsymbol{K}\cdot\boldsymbol{x}, \quad (2.10)$$

where $\boldsymbol{y}$ is the measured intensity, $\boldsymbol{K}$ is a state matrix describing the state of the atmosphere and $\boldsymbol{x}$ the unknown number density.

The absorption coefficient, α, which is needed in the radiative transfer equation (*cf.* Eq. 2.9) can generally be described by

$$\alpha = n\mathcal{I}_{LI}\frac{\nu}{\nu_0}f(\nu,\nu_0), \quad (2.11)$$

where n is the number density, $\mathcal{I}_{LI}$ is the line intensity[4] and $f(\nu,\nu_0)$ is line-shape, see Section 2.1.1.2. $\mathcal{I}_{LI}$ includes the dipole moments and quantum mechanical matrix elements involved in the fine structure of the line. Numerous sources exist for it and by default for our retrievals the JPL-catalog is used Pickett et al. (1998).

2.1.1.2 The line-shape

Ambient pressure and temperature will affect the shape of the line emitted by a molecule. In an optically thin case the spectral line-width is proportional to the ambient pressure. It

[3]From hereon the subscript ν is left out for readability.

[4]Not to be confused with the radiant intensity.

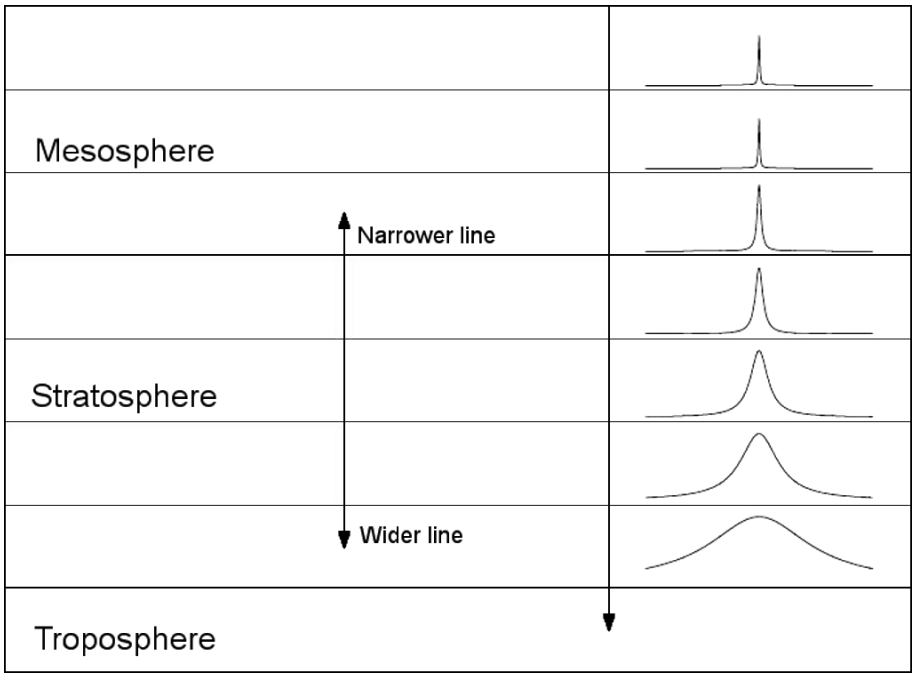

Figure 2.1: A qualitative description of how the pressure in the atmosphere affects the line-shape. The initially narrow line is broadened by the increasing pressure in the atmosphere as the line is observed from a lower altitude.

is therefore possible to deduce an altitude distribution of the observed species by correlating the shape of the line to the different broadening processes. A qualitative example can be seen in Figure 2.1. In addition to pressure broadening the spectra is also affected by the Brownian motion of the molecule (Doppler broadening). Both processes are much larger than the natural line-width. The latter arises from Heisenberg's uncertainty principle ($\Delta t \cdot \Delta E > h$) and the finite lifetime, Δt, of the excited state, which introduce a small uncertainty of the emitted frequency, $\Delta\nu = \Delta E/h$.

- **Pressure broadening**, or collisional broadening, is caused by nearby particles which disturb or disrupt the emission process by impacting the emitting particle. The timescale of the impacts is shorter than the actual emitting process. A basic treatment of the pressure broadening produce a Lorentzian line-shape, $f(\nu, \nu_0)$. In the pressure dominated region it can be estimated by:

$$f_L(\nu, \nu_0) = \frac{1}{\pi} \cdot \frac{\Delta\nu_c}{(\nu - \nu_0)^2 - \Delta\nu_c^2} \tag{2.12}$$

  where $\Delta\nu_c$ is the pressure broadening constant, giving the HWHM[5] line-width (see Fig. 2.2) (Janssen 1993). The basic treatment is only valid for low pressures such as the stratosphere and mesosphere where $\nu \approx \nu_0$. As the pressure increase in the troposphere the line-shape needs the more exact form estimated by the *Van-Vleck-Weisskopf line-shape*[6]. The Van-Vleck-Weisskopf line-shape reduces to the

[5] *Half-width at Half Maximum*

[6] which takes into account quantum mechanical effects of absorbing molecules in a collisional environment

Lorentzian at low pressures. $\Delta\nu_0$ is related to the pressure and temperature as:

$$\Delta\nu_c = \Delta\nu_0 \cdot \frac{p}{p_0} \cdot \left(\frac{T}{T_0}\right)^{\chi}, \tag{2.13}$$

where p and T are the ambient pressure and temperature, while χ and $\Delta\nu_0$ are experimentally determined parameters, specific for the line at T_0 and p_0.

- **Doppler broadening** stems from the kinetic behavior of the emitting specie. An unperturbed gas at a temperature T have a Gaussian distribution of the velocity components along the line of sight. In the thermally, or Doppler, broadened region the different velocities of each molecule will slightly shift the radiation frequency and broaden the line. The shape of a Doppler broadened line can be described by

$$f_D(\nu, \nu_0) = \frac{1}{\Delta\nu_D} \cdot \sqrt{\frac{\ln 2}{\pi}} \cdot \exp\left[-\ln 2 \cdot \left(\frac{\nu - \nu_0{}^2}{\Delta\nu_D}\right)\right]. \tag{2.14}$$

  The Doppler shape factor, $\Delta\nu_D$, is mainly dependent on the frequency, ν_0, of the line and less on the ambient temperature (see Fig. 2.2). It is given by

$$\Delta\nu_D = \nu_0 \cdot \sqrt{2 \cdot (\ln 2)} \cdot \sqrt{\frac{kT}{mc^2}}, \tag{2.15}$$

  where m denotes the mass of the emitting (or absorbing) particle, k is Boltzmann's constant and c is the speed of light.

The *Voigt* shape is the convolution of both shapes and is used throughout the whole altitude range,

$$f_V(\nu, \nu_0) = \int_{-\infty}^{+\infty} f_L(\nu, \nu') \cdot f_D(\nu', \nu_0) d\nu'. \tag{2.16}$$

Altitude information deduced by the line-shape As indicated in Equation 2.13 the pressure broadening is linearly correlated to the pressure. In other words the retrieved spectral signal at a certain distance from the center frequency is related to a specific altitude. The Doppler broadening on the other hand is depends on the root of the temperature and is relatively stable throughout the middle atmosphere. The effects of pressure and Doppler broadening on the two rotational water vapor lines (22.235 and 183.31 GHZ) are illustrated in Figure 2.2. The tabulated parameters needed in Equation 2.13 to produce Figure 2.2 were taken from Waters (1976). The pressure broadening is almost identical for both frequencies, whereas the Doppler broadening differs significantly between the two lines. On the other hand the Doppler broadening is almost constant over the altitude range for each line (reflecting the slightly varying vertical temperature). It should be noted that the pressure broadening constant used in Equation 2.13 is different depending on the emitting molecule and the main atmospheric collider[7] It is only possible to retrieve the vertical distribution as long as the pressure broadening is greater than the Doppler broadening. For the rotational transition of water vapor at 22.235 GHz this limit is located at approximately 85 km, whereas for the 183.31 GHz line the threshold is located already at approximately 70 km.

[7]For example it differs greatly between the terrestrial planets and the gas giants.

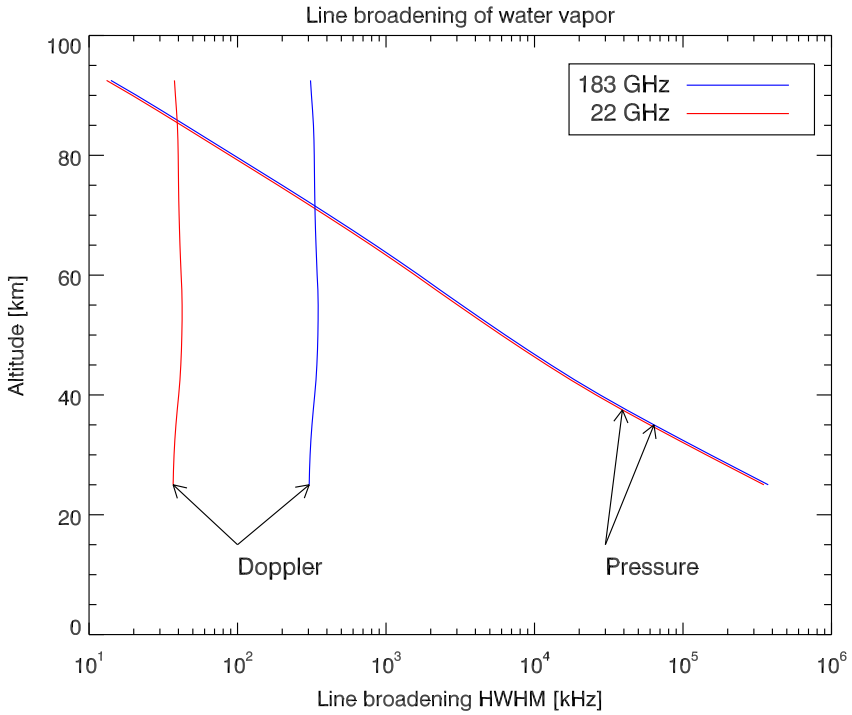

Figure 2.2: Pressure and Doppler broadening for the water vapor line at 22.235 (red, dashed) and 183.31 GHz (blue, solid). The broadening on the x-axis is defined as the HWHM of the line at the corresponding altitude. It can be seen that the altitude at which the pressure broadening becomes larger than the Doppler broadening is much higher for the 22.235 GHz line which makes it more suitable for observations of water vapor in the upper part of the middle atmosphere.

Background continuum Water vapor also has a less understood "continuum" term. Different tables of water vapor parameters treat and explain it differently. Either as the far wings of water vapor infrared emission, as a collision induced absorption or the radiation from water dimers (Janssen 1993). The water vapor continuum is however of less importance for the low pressures in the strato- and mesosphere and can be treated as an offset term in the inversion.

2.2 Heterodyne microwave spectroscopy

Microwave spectroscopy can be used to deduce information from a radiatively active source (or region), active in the sense that it emits or absorbs radiation. Heterodyne systems are typically divided into two sections; a frontend which handles the detection and frequency translation of the signal (usually called receiver) and a backend, performing for the actual spectral analysis. The system measures the radiated power of the observed process which is usually given in units of *brightness temperature*, T_b.

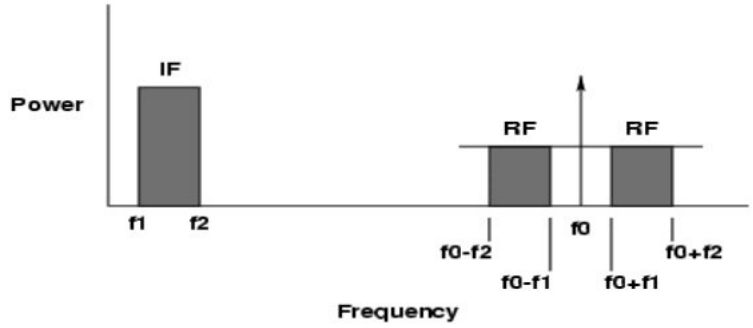

Figure 2.3: Frequency translation for a broadband signal by heterodyne technique. f_0 is the mixer (LO) frequency and the two RF bands above and below the LO frequency are the upper and lower sidebands. *Adapted from Janssen (1993)*

2.2.1 Heterodyne receivers

Heterodyne (microwave) spectroscopy is a special branch of spectroscopy in which the frequency of the received signal is down-converted by means of mixing. The original signal at microwave frequencies is difficult, if not impossible, to handle with direct electronic processing techniques and therefore down-conversion greatly simplifies the electronics involved. Figure 2.3 describes the basic function well. After the antenna has successfully coupled the input signal, usually denoted RF (*Radio Frequency*), to a transmission line it is multiplied with the LO-signal (*Local Oscillator*) using a non-linear element, the mixer. In Figure 2.3 the LO is marked f_0. One of the resulting signals is the difference between the LO and the RF frequency. This signal is called the IF signal (Intermediate Frequency) and it has the important property that its power is proportional to the power of the RF frequency, provided that the LO is much stronger than the RF signal. As can be seen in Figure 2.3 the RF signal is effectively folded around the LO frequency, producing the sidebands. In the case of a *single sideband* (SSB) instrument one of the sidebands is filtered out. The detector which converts the power of the IF-signal to a linearly related voltage is located at the end of the transmission line. In the case of this instrument the detector is a spectrometer which provides a power spectrum of the down-converted signal.

2.2.2 Fundamentals of microwave remote sensing

2.2.2.1 Brightness temperature

The concept of brightness temperature, T_b, is commonly used in microwave remote sensing to denote the power output of the measured species (Janssen 1993). For large optical depth and in LTE Equation 2.5 approaches:

$$I_\nu = B_\nu(T). \tag{2.17}$$

In the Rayleigh-Jeans limit[8], $h\nu \ll kT$, the Planck function (Eq. 2.3) can be approximated to:

$$B_\nu(T) \approx \frac{2\nu^2 kT}{c^2} \tag{2.18a}$$

$$\approx \frac{2kT}{\lambda^2}, \tag{2.18b}$$

where λ is the wavelength. Thus a linear relationship between the radiated power and the brightness of the radiation source can be described. From Equation 2.18 and 2.17 the *microwave* brightness temperature can be *defined* as:

$$T_b \equiv \frac{\lambda^2}{2k} \mathcal{I}_\nu. \tag{2.19}$$

It is important to remember that T_b is related to the intensity of the observed object, and do not necessarily reflect the physical temperature of the object.

2.2.2.2 Antenna temperature

An antenna is used to receive (and emit) electromagnetic waves. The concept of *antenna temperature*, T_a, is introduced to define how much noise the antenna produce. It is not the physical temperature of the antenna, nor is it an intrinsic parameter of the antenna. It is rather a combination of the gain pattern of the antenna and the thermal environment it is submitted to. In the case where the object of observation covers the full antenna beam the antenna temperature is only dependent on the incident radiation,

$$T_a = T_b. \tag{2.20}$$

2.2.2.3 Radiometer noise formula

The sensitivity of a radiometric system can be estimated with the radiometric noise formula. Assuming that the noise in the retrieved signal is stochastic, thus the noise power depends on the bandwidth B and the integration time t. The *system temperature*[9], T_s, is the total noise of the system, that is the total output power from the antenna and the system specific noise, or *receiver temperature* T_r.

$$T_s = T_a + T_r. \tag{2.21}$$

T_r is a measure of the internally generated power according to the Nyquist's formula as:

$$P = kT, \tag{2.22}$$

It can be derived from Planck's equation and describes the noise power P generated by a resistive component with a temperature T. T_r is therefore a figure of merit which should be kept as low as possible.

[8] Which generally can be used for microwave spectroscopy in Earth's atmosphere

[9] Note that this system temperature differs from the one commonly used and defined in radio astronomy.

It can be shown (Ulaby et al. 1981) that the smallest change in T_a (defined as ΔT_a) detectable by a radiometric system is given by:

$$\Delta T_a = K \cdot \frac{T_s}{\sqrt{Bt}}, \tag{2.23}$$

where K is a sensitivity constant which is dependent on the receiver configuration. For a *total power receiver* the sensitivity constant is 1, the total power of the signal is measured. Other receiver types are for example *Dicke*, or *Switched receiver* and *correlation receiver* in which the incoming signal is switched between, or compared to another incoming signal.

2.3 The middle atmosphere

The middle atmosphere of the Earth is a commonly used name for the stratosphere and mesosphere, approximately extending from 12 to 85 km altitude. For a long time the middle atmosphere was one of the least explored and understood parts of Earth's atmosphere. Being in the middle was the problem: on the one hand the high altitude and low density makes balloon measurements impossible, on the other hand the density is to high for satellites, which resulted in a general lack of in-situ measurements. Sounding rockets have been available from the second half of the 20th century but are limited in temporal and geographical coverage. With technological advances in remote sensing the possibilities to probe the middle atmosphere have greatly improved. Today radars, LIDARs and other ground-based instruments continuously measure a multitude of parameters in the middle atmosphere and although it is no longer called the *ignorosphere*, there are still a lot of open questions.

The following section will introduce the basic structure and some of the most important dynamical phenomena of the atmosphere in general but with a focus on the middle part. The polar mesosphere and atmospheric tides will receive extra attention due to their importance for the work in the thesis. In the end the role of water vapor in the middle atmosphere will be discussed. If nothing else is explicitly mentioned, the introduction given below is based on Holton et al. (1995), Geller (1979) and Shepherd (2000).

2.3.1 General structure

The middle atmosphere can in general be characterized by a stable stratification and an exponential decrease of density with altitude. This general structure has the effect that waves propagating from the troposphere and upward are supported in their vertical propagation. Due to conservation of energy the amplitude of the waves will increase with the decrease in density of the ambient atmosphere.

2.3.1.1 Temperature structure

An average temperature profile of the atmosphere can be seen in Figure 2.4. The atmosphere is divided into different regions according to its structure. In the lowermost layer, the troposphere, the main heat source is the surface of the Earth, and as the altitude increases the temperature decreases. The next layer, the stratosphere, is characterized by

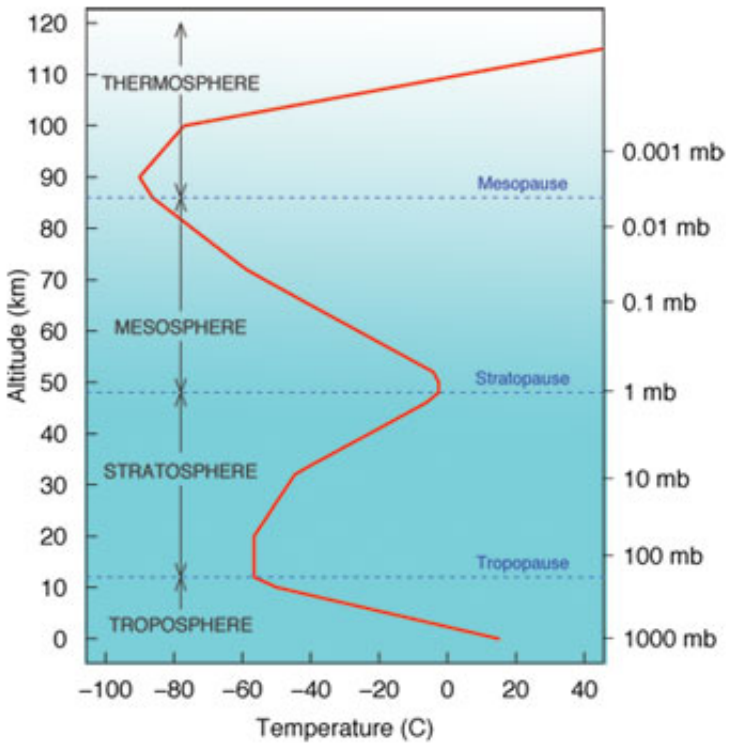

Figure 2.4: A typical temperature profile for Earth's atmosphere. The middle atmosphere is usually defined as the area between the two local minima, the tropopause and the mesopause. *Source: ©2006. Steven C. Wofsy, Abbott Lawrence Rotch Professor of Atmospheric and Environmental Science, lecture notes.*

an approximate equilibrium between heating due to absorption of solar UV and radiative cooling at IR wavelengths. However the net temperature gradient in this layer is positive due to the enhanced absorption by ozone. At about 50 km the temperature gradient is again reversed, marking the bottom of the mesosphere. Here radiative cooling primarily by CO_2, NO and O is responsible for the net cooling of the atmosphere. The mesosphere extends up to about 85 km and is of particular interest in polar latitudes due to the peculiar processes and phenomena discovered here (see Section 2.3.3). Above the mesopause the temperature rapidly increases again due to strong absorption of solar UV particularly by atomic and molecular oxygen. This region, the upper atmosphere, comprises the thermosphere and the exosphere. It is very sensitive to solar activity with temperatures between 500 and 2000 K. The dominant transport process here is molecular diffusion which results in a layered structure with the heavier elements in the lower part.

2.3.2 Dynamics of the middle atmosphere

The below description of various concepts important in the middle atmospheric dynamics is by no means a complete review of the complex dynamical behavior. It should be seen as a short and general introduction to the main dynamical processes in the middle atmosphere region. If nothing else is said, it is based on the general introductory books by Lindzen (2005) and Volland (1988). In addition the reviews of Forbes (1995) and Fritts

and Alexander (2003) have been used.

2.3.2.1 Mean transport

The motion in the atmosphere of the Earth is almost solely caused by either differential heating by the sun or the rotation of the planet[10]. The mean flow in the stratosphere and mesosphere is mainly driven by a difference in the ozone-layer heating and subsequent radiative cooling. However tropospheric forcing can significantly affect the middle atmospheric zonal state. There is a mean meridional flow with rising air near the summer pole, a high altitude meridional drift towards the winter pole where the air descends to lower altitudes. The effect of the Coriolis torque on this circulation gives rise to mean zonal easterlies in the summer hemisphere and westerlies in the winter hemisphere. These are in approximate thermal equilibrium with the zonal mean temperature field.

Concerning the general circulation of the atmosphere, it is often useful to discuss deviations from the mean flow as waves or eddies. The long term, time-dependent, deviations from the mean flow will be shortly described below. Faster oscillations, such as diurnal and semidiurnal tides will be discussed in detail in Section 2.3.4.

The quasi-biannual oscillation (QBO) The equatorial mean wind in the stratosphere exhibits an approximately 27-month oscillation between east- and westward flow. The cause for this behavior, and especially its odd periodicity is somewhat complex, but can be fundamentally described by a wave-mean flow interaction. Assume there are two sets of waves in the lower atmosphere, one with eastward phase speed and momentum, and the other is westward. They are absorbed by the background flow when they encounter a critical level (zero intrinsic phase speed). With a background wind carrying eastward vertical shear the eastward wave will be absorbed at low altitude, whereas the westward waves can propagate higher where they break and deposit westward momentum. Over time, the eastward high-altitude wind will slow down and eventually turn westward, and the westward waves will dissipate at lower altitudes. Eventually, the low-level eastward flow will have turned westward and the eastward waves will propagate higher and the cycle is restarted, in the opposite direction. The QBO mainly affect the stratosphere, but has shown to have an influence on tides in the upper mesosphere in numerical simulations. Mayr and Mengel (2005) observed that modulations of the tides below 50 km and above 80 km can be attributed to the QBO. They argue that the QBO signature is weaker in between due to interference with the strong seasonal changes although there are indications that the water vapor is affected at 70 km (Sonnemann et al. 2009).

The semi-annual oscillation (SAO) Semi-annual oscillations of the equatorial mean wind is a global phenomena that mainly extends from the upper stratosphere to the lower mesosphere. It peaks around the stratopause in the zonal wind. During solstice, easterly anomalies occur, and westerly anomalies during equinoxes. Even though bundled into the same oscillatory process, it seems that the easterly and westerly maxima are forced by different processes. The easterly accelerations on the one hand are forced by meridional advection of easterlies from the summer hemisphere across the equator, occurring

[10] Waves caused by volcanic eruptions excluded.

in general after the solstice. The westerlies on the other hand are thought to be forced by fast Kelvin waves and breaking internal gravity waves that deposit their momentum in the upper stratosphere. Due to the local minimum around 65 km it is sometimes divided into the Mesospheric Semi-Annual Oscillation (MSAO) and the Stratospheric Semi-Annual Oscillation (SSAO). The MSAO show similar amplitudes in the zonal wind as the SSAO, but with a 180° phase shift.

Sudden stratospheric warmings Very strong increases in stratospheric temperatures for a short period of time, usually known as *Sudden Stratospheric Warmings* (SSW), were first observed in the 1950s. The heating is much too fast and strong to be caused by radiation alone, and it was not until 1971 that an explanation for this behavior was put forward (Matsuno 1971).

In essence they are caused by a change in the location of the angular momentum deposition by planetary waves from the climatological position in mid-latitudes to the polar regions. This leads to a deceleration of the polar zonal wind and a warming of the underlying regions. The process has a strong positive feedback which increases the strength of the warming, and the speed by which it develops. Planetary waves are primarily forced by topography and land-sea contrasts, and it has been shown that only planetary-scale Rossby waves can propagate into the middle atmosphere during winter. As these waves are the primary reason for the SSWs, it is normal to expect that SSWs are very rare on the southern hemisphere where there is not enough forcing of the planetary waves to initiate warmings on a regular basis.

There are two sudden stratospheric warmings visible in Figure 2.5.

2.3.2.2 Planetary size waves

Energy and momentum is principally distributed in the atmosphere by wave-like motions. These motions can be classified by their restoring force and are sometimes subdivided according to their propagation and wavelength. They are the main cause for the QBO, hemispheric asymmetries and stratospheric warmings to name only a few processes.

Planetary waves Planetary waves are, as the name implies, oscillations with global-scale wavelengths. They can be stationary or propagate with respect to the background zonal wind. The restoring mechanism is the latitudinal gradient of the potential vorticity. Only planetary waves with very long wavelengths can propagate into the stratosphere. This is further constrained by the background wind as propagation can only occur in moderate to weak westerly zonal winds. Shorter scale waves are therefore generally confined to the tropospheric and stratospheric winter hemisphere. During normal atmospheric conditions they are blocked from the upper mesosphere by easterly stratospheric winds. However they have been observed and found to have significant effects on the mesosphere and even higher.

Gravity waves Gravity waves are typically generated in the troposphere through the action of weather systems or orographic lifting of air-masses. The restoring force is buoyancy, thus gravity and stable stratification allow for their propagation. They are an important mechanism in the transport of energy and momentum from the lower to the

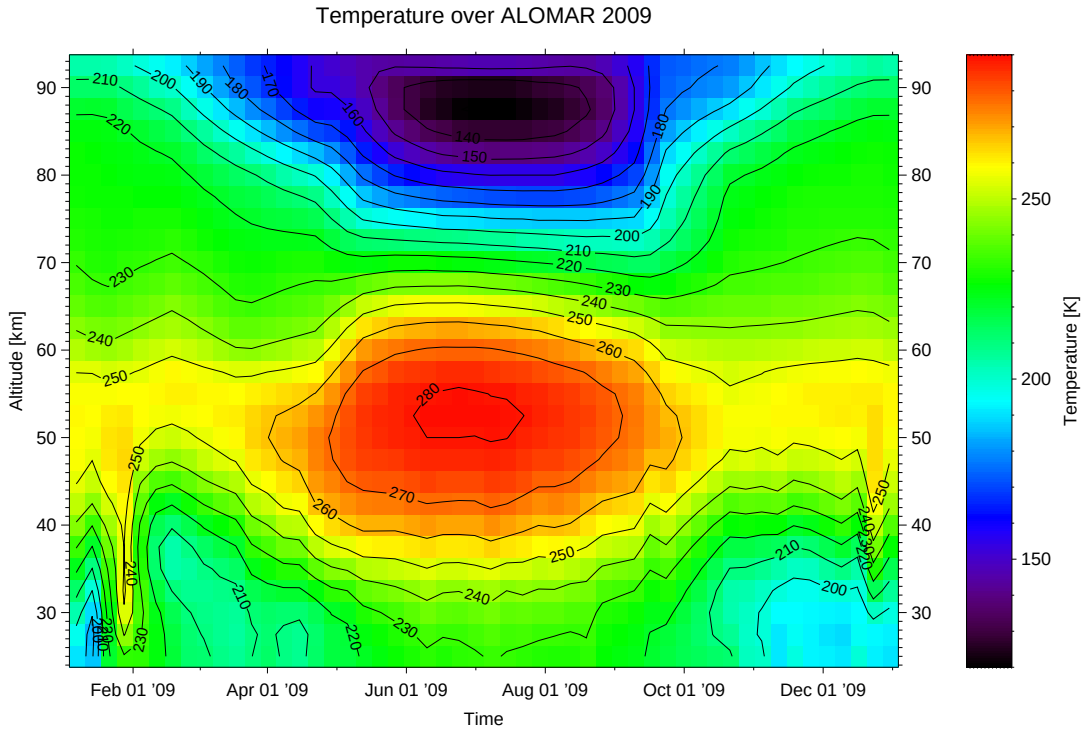

Figure 2.5: The middle atmospheric temperature over ALOMAR during 2009. Note the two stratospheric warmings in the beginning and end of the year. The temperatures in the upper part of the atmosphere are based on the CIRA86 model with additional correction from falling sphere data, whereas the lower part is real data from NCEP.

upper atmosphere. There is little doubt in their importance for the general energy and momentum balance in the atmosphere.

Kelvin waves Kelvin waves are uniquely equatorial waves. From the point of view of restoring force they are gravity waves. They are a special case in the sense that they do not have a meridional component and propagate eastward with a velocity in geostrophic balance with the latitudinal pressure gradient.

2.3.3 The polar mesosphere

The mesosphere in general, and the polar mesosphere in particular, is a transition region. The coldest temperatures of the Earth can be found here – the cold summer mesosphere, sandwiched between the relatively warm stratosphere and thermosphere. In addition, the turbopause, a border between the homogenous and heterogenous mixing in the atmosphere is located just above the mesosphere. Electrons and ionized plasma created by incoming solar radiation in the thermosphere may extend down to the polar mesosphere and give rise to aurorae.

The cold temperatures and water vapor give rise to the highest clouds on Earth – the noctilucent clouds or NLCs (sometimes called polar mesospheric clouds (PMC)).

Cold summer mesosphere If only governed by radiative processes, the thermally responsive middle atmosphere would be expected to show a latitudinal temperature structure, changing with the solar insolation at the time of the year. The continuously lit summer mesosphere should then be much warmer than the dark winter hemisphere. This is however not the case, in fact the opposite is observed. The situation can be seen in Figure 2.5 which shows the temperature over ALOMAR for 2009. This is in fact the same background atmosphere used for retrieving the data taken at ALOMAR (see Section 4.2.1.1 for a detailed description of the data). In the polar regions, the winter temperatures are up to 100 K higher than expected by a radiative equilibrium, a situation which indicates dynamic heating and cooling. The reason for this behavior can be found in angular momentum deposition by waves. Similar to the discussion of deposition of angular momentum and filtering of waves for the case of the QBO in Section 2.3.2.1, not all waves can propagate into the mesosphere. In the summer hemisphere, the background mean zonal flow is westward. Gravity waves carrying a westward momentum will therefore be absorbed at lower altitudes. Waves carrying eastward momentum can on the other hand propagate higher, and by depositing their angular momentum in the mesosphere the zonal flow will be slowed down, and eventually reversed. This forces a change of the global circulation pattern as the meridional wind will now flow from the winter pole in the low altitudes and back at high altitudes. Vertically rising air at the summer pole will adiabatically cool the mesosphere to the observed temperatures.

Noctilucent clouds (NLCs) Noctilucent clouds were first observed 1885, just after the Krakatoa eruption. Although the region is suspected to be quite sensitive to changes in the global climate (Rapp and Lübken 2004), the question whether the NLCs are related to the climate or not is still debated (von Zahn 2003, Thomas 1996, Thomas et al. 2003). They are the highest clouds in Earth's atmosphere, approximately located at 83 km altitude. Due to the difficulties associated with probing the general state of the region in which they occur, they can be used as tracers for some of the phenomena that takes place there. The particles making up the cirrus-like cloud mainly consist of water ice deposited on a nucleation core (usually smoke particles). They scatter light sufficiently to be observed by optical instruments (Gadsden and Schröder 1989). Before the ice-particles grow large enough for this to happen (>50 nm) they are visible to radars and are then called polar mesospheric summer echoes (PMSEs) (Rapp and Lübken 2004). They are only visible during summer, when the temperatures in the mesosphere are low enough, and there is enough ambient water available. There are indications that they strongly affect their environment in terms of redistributing trace gases (mainly water vapor) by freeze drying effects (von Zahn and Berger 2003). Furthermore, observations show that metal atoms, which are usually present in the mesopause region vanish in the presence of NLCs (Lübken and Höffner 2004), which could be an indication that these atoms can act as the condensation nuclei for the ice-particles.

2.3.4 Atmospheric tides

Global-scale oscillations with a period of a solar day, and their sub-harmonics, are usually referred to as atmospheric tides. Such oscillations are present in all dynamical fields; temperature, wind, density and pressure. They may be either east- or westward traveling

waves, but the largest components are the westward propagating waves which follow the apparent movement of the sun, the *migrating* tides. These global-scale waves represent a good example of "forced" atmospheric waves for which the period is quite well known. Chapman and Lindzen (1970) first described their general properties and also described their behavior analytically. In 1982 Forbes extended and numerically modeled the "classical" tide theory in two successive papers (Forbes 1982a,b).

Tides are thermally driven by the periodic absorption of solar radiation throughout the atmosphere, primarily the absorption of infrared radiation by water and water vapor in the troposphere and ultraviolet radiation by stratospheric ozone. Large-scale latent heat release by convective systems and non-linear interactions between global-scale waves are also important excitation sources of atmospheric tidal waves (Hagan and Forbes 2002, 2003). It is generally accepted that the tides, like gravity waves, play an important role in the dynamics and energy balance of the middle atmosphere.

Tidal behavior of winds are regularly observed by ground-based radars today. A large set of observations from the polar regions exists, and climatologies of the monthly mean tidal parameters for the different wind fields have been published (Portnyagin et al. 2004). As already mentioned, water vapor is a good tracer for the dynamics in the middle atmosphere and is therefore expected to show variability on a diurnal or semidiurnal scale. There is no production or destruction of water vapor at these timescales, hence all measured variation should be a result of transport. If a homogenous zonal distribution of water vapor is assumed, only meridional and vertical winds control the variability in the vertical profile, as measured by ground-based instruments. Up to now there has been no solid evidence of a tidal component in water vapor variability in the polar regions due to the inherently weak signal.

2.3.5 Water vapor in the middle atmosphere

Only three components make up more than 99% of Earth's atmosphere; nitrogen, oxygen and argon. Nevertheless, the less abundant species, the trace gases, do play an important role in the many different processes that govern the climate and dynamic behavior.

Water vapor is of great scientific interest due to its role throughout a major part of the atmosphere. In addition to being the most important green-house gas the latent heat associated with its phase transitions contributes substantially to the total energy transfer in the troposphere. Higher up, it has a key role the formation of aerosols and polar stratospheric clouds. Water is also an important component in the stratospheric chemistry. In the mesosphere water is still radiatively and chemically active. The formation of noctilucent clouds (Sec. 2.3.3) is also dependent on the available amounts of water vapor.

The water vapor mixing ratio decreases from the lower troposphere to the mesosphere by 4 orders of magnitude. A local minimum exists at the tropopause which acts as a cold trap where upwelling air is freeze dried. Above the tropopause the water vapor mixing ratio slowly starts to increase again due to oxidation of methane. This process peaks at approximately 60 km, and above 65 km all methane is assumed to be oxidized. Here the water vapor starts to photo-dissociate due to Solar Lyman-α radiation, an effect which becomes stronger with increasing altitude. Between 65 – 70 km, a weaker secondary autocatalytic source exists which gives rise to a secondary maximum. Higher up in the atmosphere, the Lyman-α radiation dissociates the water molecules, which results in the

decrease of the mixing ratio. The distribution of water vapor in the middle atmosphere is therefore a balance between the primary source, methane oxidation, transport (the general circulation) and the photo-dissociation sink above 60 km. The rate of photo-dissociation and methane oxidation is fairly well understood, thus measurements of water vapor distribution can be used to constrain the timescales of middle atmosphere transport.

2.3.5.1 Variation of water vapor in the middle atmosphere

The annual variability of water vapor in the upper parts of the middle atmosphere is determined primarily by the mean transport from the wetter lower atmosphere. It results in the annual oscillation, as reported by Seele and Hartogh (1999) and Nedoluha et al. (1996), and a semi-annual oscillation (Lossow et al. 2008). The period of the oscillation depends on the latitude; at higher latitudes it is primarily annual, whereas in the equatorial regions semi-annual. The oscillation depends on the mean of transport. If transport is mainly by advection, the water vapor distribution is expected to have an annual oscillation. During summer, the mean flow is upward, transporting water-rich air high up in the altitude. The flow is reversed during winters with a resulting decrease in high-altitude water vapor. If instead diffusion is dominant, the semi-annual oscillation in the water vapor will be the result. The turbulent diffusion is increased by breaking gravity waves, which are important during the equinoxes. Thus the maximum of such oscillation is during equinoxes.

3 Description of the measuring instrument

Water vapor is an important tracer in the middle atmosphere which can be detected by ground-based microwave observations. A multiple of transitions of the water molecule exist in the microwave region, but for ground-based spectroscopy only two are used; a relatively weak line at 22.235 GHz and a much stronger line at 183.31 GHz. However, due to the high opacity of the 183.31 GHz line it is less suitable for instruments located at sea level. On the other hand nearly continuous measurements could be made from high altitude sites such as the Atacama desert in Chile or the extremely cold dry conditions in Antarctica. As a consequence, for many of the locations in the world the weaker but optically thinner line at 22.235 GHz is used to monitor middle atmospheric water.

In order to determine the distribution and short term variability at high altitudes a very stable and sensitive instrument is needed. Since 1995 (Hartogh and Jarchow 1995b) a microwave spectrometer (WASPAM) has been measuring the water vapor distribution above ALOMAR, Andøya and in 2008 this instrument was followed by a new, more sensitive system (Hallgren et al. 2010) (cWASPAM[1]). The new system is based on the same principles but with a cooled, dual polarization, frontend and a double backend a higher sensitivity can be achieved. A simplified picture of the basic working principle can be seen in Figure 3.1.

An engineering 3D-sketch of the frontend can be seen in Figure 3.3. The input is alternated between either one of the internal loads, or the atmosphere by means of a rotating parabolic mirror. Together with two similar, statically mounted mirrors pointing at the calibration loads, the rotating mirror is mounted on a movable baseplate. In front of each mirror there is a window transparent in the microwave region, (see Figure 3.3). In order to split the incoming signal into its vertical and horizontal component an OMT (*ortho-mode transducer*) is connected to the wave-guide of the antenna. Before leaving

[1] cooled WASPAM

Table 3.1: The location of each of the instruments manufactured up to now. Data from cWASPAM2 is so far limited as it has been used as a testbed for debugging purposes.

Name	Location	Operated by
cWASPAM1	ALOMAR, Norway	MPS
cWASPAM2	Katlenburg-Lindau, Germany	MPS
cWASPAM3	UFS, Germany	MPS
MISI	Kühlungsborn, Germany	IAP

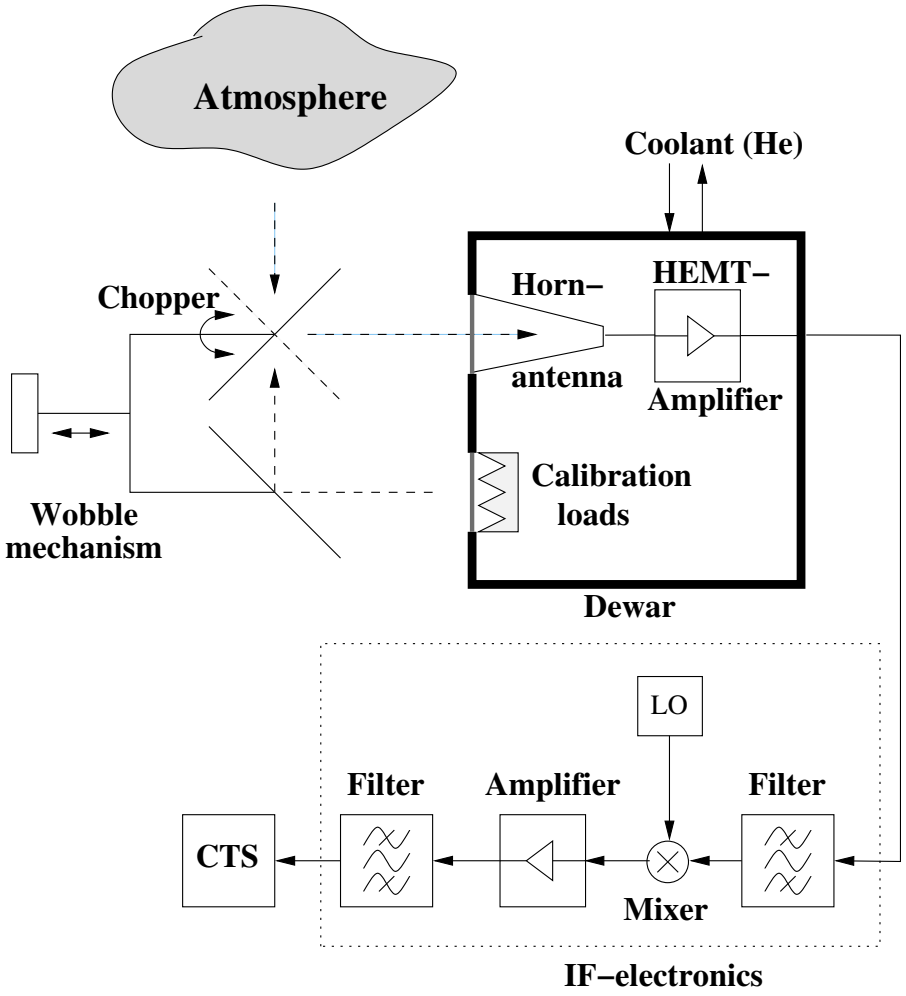

Figure 3.1: A schematic overview of the instrument. The main mirror can be rotated to switch the beam between the loads and the atmosphere. In the dewar the incoming signal is split into two identical signal chains (only one is shown for readability) where it is amplified, down-converted and filtered before analysis in the CTSs.

the dewar the signal is amplified twice, first by a cooled amplifier and then boosted by a second amplifier at room temperature. In the next stage, the IF stage, the signal is filtered, down-converted by means of heterodyne mixing and further amplified. The last step in the chain is the spectral analysis carried out by the backend spectrometers (one for each polarization). The resulting spectra are sent over a local network to the process- and house-keeping computer for temporary storage.

In total four almost identical instruments have been built which are spread around northern Europe, the name and number designation, location and responsible institute for each can be seen in Table 3.1.

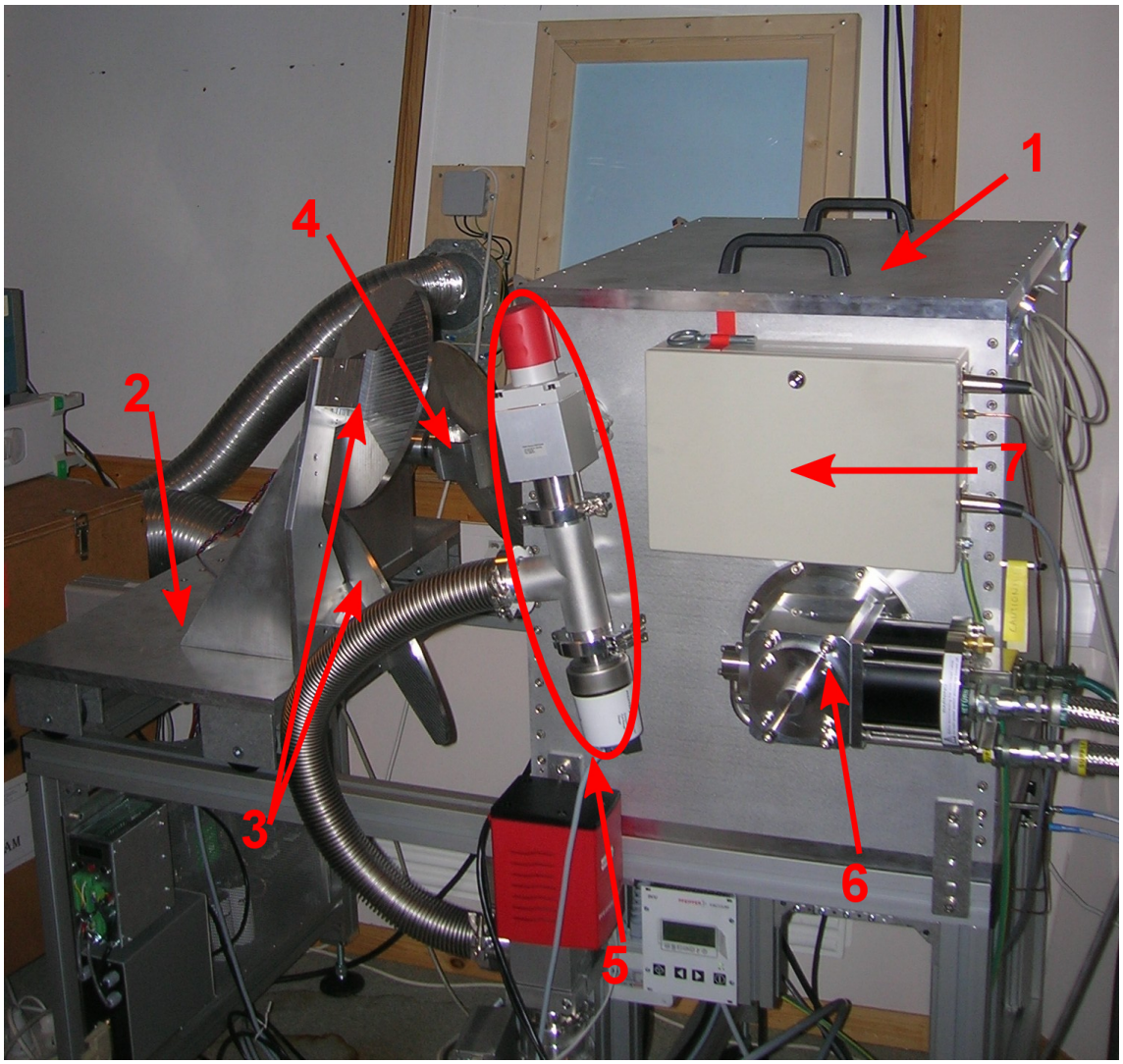

Figure 3.2: cWASPAM1 on location at ALOMAR, Andøya. The frontend dewar is the big metal box in the middle of the image (1), and the optical movable table (2) is visible to the left. The two mirrors in the left foreground are the static mirrors (3) pointing to the calibration loads while the backside of the rotating mirror (4) can be seen in the background between them. Safety valves and the pressure sensor for the vacuum setup (5) as well as the liquid helium in- and outlet hose (6) for the cooling compressor can be seen on the side of the dewar. The grey box (7) contains electronics for temperature readouts and power stages for dewar electronics.

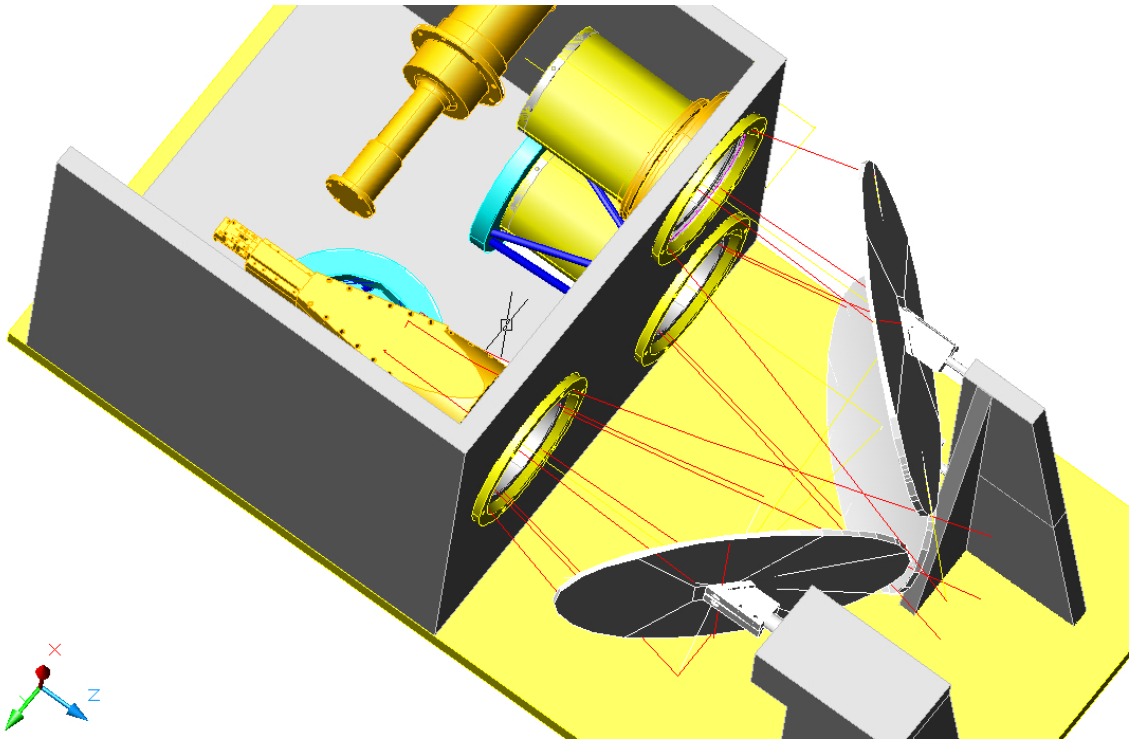

Figure 3.3: 3D engineering schematic of the frontend of the instrument. The three mirrors and their mounting in front of each window can be seen as well as the inside of the dewar. On the inside of the dewar the cold-finger from the helium compressor can be seen coming in from the side and the structural mounting of the loads and antenna.

3.1 The frontend

The water transition observed is weak, and to detect it the receiver frontend has been optimized in terms of sensitivity. It consists of a corrugated horn antenna, the OMT and two HEMT (*high electron mobility transistor*) amplifiers mounted into a dewar and cooled to a temperature of approximately 15 K. There is another set of amplifiers operating at room temperature which boost the signal before the down-conversion. This results in a receiver temperature of the system of only 30 K for each polarization (single side-band). The dewar also contains the internal calibration loads and is mounted together with the optical table on an aluminum baseplate. It is all integrated into an aluminum rack. A photo of the actual setup from the instrument at the ALOMAR observatory can be seen in Figure 3.2.

3.1.1 Instrument dewar

The dewar is a large aluminum cube that contains all the cooled parts of the frontend. In order to avoid air[2] to condense and freeze on the components the dewar is evacuated and kept under vacuum. A detailed description of the setup and design can be found in

[2] All the gases that makes up air will condense and freeze at the temperatures of the components in the dewar.

Appendix A.

3.1.2 Chopper and wobbler control

During measurements the incoming signal is alternated between the atmosphere and the two different calibration loads. This is achieved by rotating the main mirror between the atmosphere and the two mirrors pointing to the respective calibration load. A stand-alone unit, called the chopper controller, ensures the rotations are carried out correctly. In synchronization with the rotation of the mirror the whole optical table is moved back and forth. By fine tuning the speed and length of the wobbling movement standing waves in the optical path can be minimized. Both the chopper controller and the unit controlling the wobbling of the optical table are described in detail in Appendix A.

3.2 The backend – two chirp transform spectrometers

Whereas the reception of the observed specie with minimal noise is carried out in the frontend, the task of the backend is to transform a spectrum from the time domain to an integrated spectrum in the frequency domain. This instrument is using two Chirp transform spectrometers (CTS) with high spectral resolution, one for each polarization. They have a bandwidth of 40 MHz, a spectral resolution of 9.8 kHz and the data are evenly binned into 4096 channels of 14 kHz each (slightly oversampled) and a center frequency of 1350 MHz. Interprocess control, memory handling and the external Ethernet interface are handled by a PC104, an embedded computer. The CTSs and the process-control computer are mounted into a separate 19" rack, together with a multimeter that reads the temperature sensors on the calibration loads and a network router for the instrument network.

3.2.1 Chirp transform spectrometers

The Chirp transform spectrometer is a real-time spectrometer, real-time in the sense that it has a duty cycle of 100%. A high spectral resolution can be attained which is of interest especially in atmospheric sciences. The Doppler broadening of water vapor at 22.235 GHz is about 30 kHz and to retrieve the vertical profile up to this limit it is preferable to be able to resolve features smaller than this. Details about the distribution, pressure and temperature profiles as a function of altitude can be deduced from the line-shape of the observed molecule.

The first successful microwave spectroscopy measurement with a CTS was made in the 1980s when the rotational transition of the 142 GHz line of ozone was detected (Hartogh and Hartmann 1990). Since the mid-1990s a radiometer with a CTS backend has continuously been observing the middle atmospheric water vapor at ALOMAR (Hartogh and Jarchow 1995b). CTSs have also been used at the the Heinrich Hertz Submillimeter Telescope (HHSMT) at Mt. Graham, Arizona for astronomical applications (Villanueva 2004, Paganini and Hartogh 2007). The first[3] deep-space mission carrying an CTS is

[3] and only so far

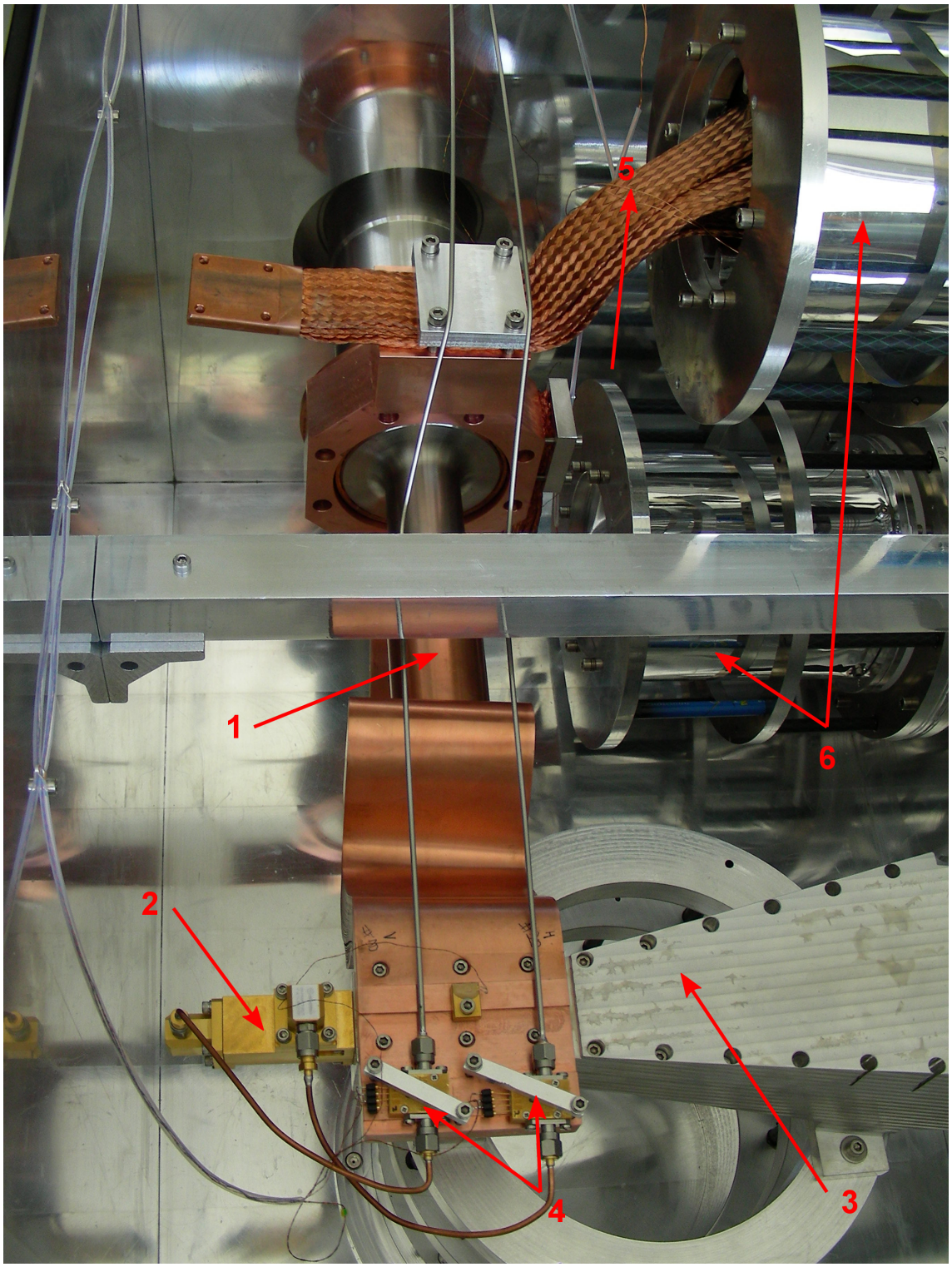

Figure 3.4: A picture from the inside of the dewar. The cold finger (1), horn antenna (3) and the loads (6) as well as the copper braids (5) connecting the loads to the cold finger can be seen. To the left the OMT (2) can be seen, and in the middle the HEMT amplifiers (4) mounted on top of an extension from the cold finger are visible.

MIRO on ROSETTA (Beaudin et al. 1998, Gulkis et al. 2007).[4]

3.2.1.1 Principles of the Chirp transform spectrometer

The Chirp transform spectrometer is based on the dispersive delay of acoustic surface waves of different frequencies on a piezoelectric crystal substrate. The actual dispersion is determined by the physical microstructure of the crystal, the SAW-filter (*Surface Acoustic Wave*). Acoustic waves propagate along the surface of the crystal and depending on their frequency the pathlength will differ which results in a time dispersion of the incoming signal. The impulse response of a dispersive line is a sweeping frequency at the output and by fine-tuning the dispersion properties a time-frequency transformation can be performed. In reality at least two SAW-filters are needed, one expander and one compressor. A crucial part of the CTS is the matching of the filters as the dynamical range and resolution is directly dependent on the matching parameter.

The incoming signal is mixed with a chirp signal and convolved with the impulse response of the compressor filter. Each Fourier component of the incoming signal is converted to a chirp with a time-frequency slope determined by the mixing chirp, but the starting frequency is defined by the Fourier component. The linear time-frequency correspondence in the system means that the differences in the frequency domain between the original components translates to time displacements in the resulting output. A preprocessor digitizes the analog output and computes the power output, taking into account both the real and imaginary part of the signal. Finally the signal is mapped to memory where it can be integrated and read out between each measurement period.

Mathematically the CTS is based on the Chirp transform (Klauder et al. 1960, Darlington 1964), an algorithm derived from the Fourier transform.

$$F(\omega) = \int_{-\infty}^{+\infty} f(t)e^{-j\omega t}, \tag{3.1}$$

with $\omega = 2\pi f$. By assuming a linear relation between frequency and time, $f = \mu\tau$, where μ is the chirp rate, *i.e.* the proportionality constant between the frequency and time, and by using the identity $2\tau t = t^2 + \tau^2 - (t-\tau)^2$ the "Chirp Transform",

$$F(2\pi\mu\tau) = e^{-j\pi\mu\tau^2} \int_{-\infty}^{+\infty} \left[f(t)e^{-j\pi\mu t^2}\right]\left[e^{-j\mu(\tau-t)^2}\right] dt \tag{3.2}$$

is obtained. If Equation 3.2 instead is presented as

$$(f * h)(t) = \int_{-\infty}^{+\infty} f(\tau)h(t-\tau)dt, \tag{3.3}$$

the mathematical representation of a convolution become apparent. The input signal, mixed with a chirp, ($f(t)e^{-j\pi\mu t^2}$) is convolved with the dispersive filter ($e^{-j\mu(\tau-t)^2}$). The term outside the integral, representing a constant phase shift needs to be corrected if the phase of the input signal should be retained. For a more detailed discussion on the complex Fourier transform, taking into account the finite time and bandwidth of the chirp see Jack et al. (1980) and Jack and Paige (1978).

[4]Originally there was also a CTS planned for the Herschel mission, but that was later scrubbed due to financial reasons.

3.3 Instrument control

An ordinary desktop PC running a Linux distribution[5] is used for process control and house-keeping purposes (from hereon denoted as the process control computer)). It controls the normal operation of the instrument, checks temperatures and pressures and acts as a first buffer for storing the data before download to the archives at MPS.

Temperature readouts Accurate temperatures of the loads are needed for correct calibration of the data. Furthermore, a record of room temperature as well as amplifier and dispersive delay filter temperatures are of interest for instrumental debugging purposes. These parameters are therefore continuously measured by a digital multimeter[6] (DMM) which is connected to the process control computer. Temperatures in the dewar are measured by cryogenic silicon diodes[7] whereas filter and room temperatures are measured by PT-100 platinum resistance thermometric sensors[8]. The multimeter measures voltages provided by the thermometric sensors, either from thermoresistivity, or as in the case of the diode where the forward voltage is proportional to the temperature. These voltages are converted into temperatures in the process control computer. Dewar pressure is measured by a compact FullRange™gauge from Pfeiffer Vacuum[9]. The multimeter reads a voltage from the sensor which is converted into pressure in the logging software. A possibility to control an electromagnetic valve[10] in the vacuum setup exist for safety reasons. Two logfiles of the instrumental parameters are kept in parallel; the raw voltages measured by the multimeter and calibrated units (temperature and pressure).

RTAI In a normal operating system the time it takes from an instruction being sent until it is actually carried out can vary quite a lot, depending on the current load of the system. The kernel in the process control computer has been patched with a Real-Time Application Interface (RTAI[11]) in order to achieve a deterministic behavior (crucial for the wobbler control, see Section A.3). RTAI provides latencies of the system of approximately 15 μs, which is much faster than the time needed to rotate the mirrors ($\approx$300 ms). The control of the of the system processes can therefore be assumed to be instantaneous.

3.3.1 Process control

The instrument control is build with a modular approach. This adds flexibility in case parts of the instrument need to be exchanged as well as facilitating debugging. The actual measurement process is run in a serial loop whereas data and process control logs are run separately. Wobbler and chopper control are carried out in parallel to the measurement process but can also be run independently for debugging purposes. The different steps in the process are:

[5] Opensuse 10.1 with kernel 2.6.24
[6] Agilent 34970A with AD converter for readout of analog voltages.
[7] Model CY7 from Omega Engineering Inc.
[8] From Lake Shore Cryotronic Inc.
[9] Model no. PKR 251
[10] Also this from Pfeiffer Vacuum, model no. PFA54505
[11] RTAI is free and can be downloaded from `www.rtai.org`. The version used is 3.6.1

1. Start wobbling motion, backward or forward depending on which step in the calibration and measurement cycle is carried out.
2. Start to integrate the measurement in the CTS.
3. Stop integration and send finished signal.
4. At the end of wobbling motion acknowledge signal sent from wobbler.
5. Rotate mirror to next position (following the Cold-Sky-Hot-Sky cycle, see Fig. 3.6), and send ready signal when in position.
6. Restart loop

During each measurement cycle CTS-data from the last cycle are downloaded to the process control computer. In parallel to this process house-keeping data are taken from the DMM. The DMM and CTS-data are stored together in the raw-data file. The house-keeping data are also stored in a separate house-keeping logfile for easy access. Note that the wobbling motion and integration by the CTS are two separate processes that need to be in sync in order to minimize the "dead-time" between each step in the cycle. More importantly, to achieve an optimal baseline reduction the mirror position and wobbling pathlength need to be synchronized so that each measurement cycle is carried out simultaneously with the movement of the optical table.

3.3.2 Interprocess communication

The spectrometers are autonomous computers and to enable contact between them and the process-control computer they are connected to a local network. For communication, data exchange and measurement control an internal socket server is setup on each of them. The DMM on the other hand does not have an Ethernet interface by itself and is therefore connected to a GPIB-Ethernet hub. This enables us to control the DMM and to retrieve the house-keeping data. For chopper and wobbler control the parallel ports are used as they demand a minimal amount of overheads for the control, essentially single 8 bit commands are used. Processes that run internally on the process control computer (calibration, storage control, overhead control etc.) communicate by pipes.

3.3.3 System monitoring and data storage

One development goal of the instrument was low maintenance requirements, thus a high degree of automation has been implemented. A buffer with calibrated data is kept in parallel to the long-term storage which can be used by a quick-look plotting software. This facilitates calibration and fine-tuning of the baseline removal. All data are saved in raw format together with system performance parameters to allow maximum flexibility in the analysis. The total amount of data adds up to approximately 500 MBytes every 24 hours. The raw data are saved in binary format whereas the logfiles are stored as ASCII-files.

In the case of harddisk failure on the process control computer a soft RAID1 mirroring array is administered. The array has enough space to store data of more than 50 days of continuous autonomous measurements.

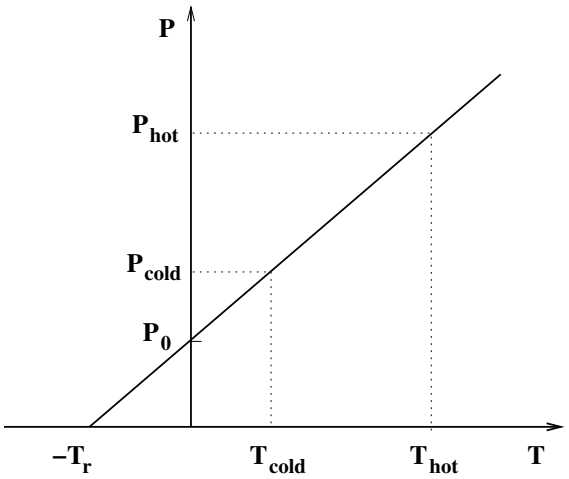

Figure 3.5: Calibration of measured antenna temperature with two loads at known temperature, T_{Cold} and T_{Hot}. The gain coefficient is given by the slope of the line and $-T_r$ can be determined by the power output at zero input temperature (P_0).

3.3.3.1 Parameter watchdogs

A three level approach controls the instrument operation; 1) instrument parameter check (*e.g.* dewar pressure and temperature of the amplifiers), 2) software control and 3) network availability.

During the logging process of the above mentioned instrument parameters all values are compared to a predefined "normal operations" condition table. If any value is outside the predefined range a warning email is sent to the operator. The measurement control software bundle consists of more than 10 different, simultaneously running, applications. Every hour a process acknowledge-test is performed. If a process fails to answer it is assumed to malfunction and a detailed warning email is sent. Non-operation critical applications such as the parameter-check and readout are automatically restarted and a notification is sent by email. Due to the fact that everything is controlled over Ethernet the outermost layer of control is a network check. The process control computer is regularly pinged and if it is not returned a computer or network problem is assumed, which has to be controlled.

All the above mentioned levels of continuous control, redundancy and a robust front- and backend give a reliable, virtually autonomous, system for high time resolution measurements of the middle atmosphere water vapor.

3.4 Instrument calibration

The CTS spectra have to be calibrated in order to retrieve the correct observed brightness temperature. Calibration deals with two separate parameters; an offset power which is generated within the system itself (uncoupled to the observed region) and the gain coefficient in the system.

The net IF power reaching the spectrometers can be divided into two parts; 1) the measured signal, proportional to the antenna temperature, T_a, and 2) the internally generated

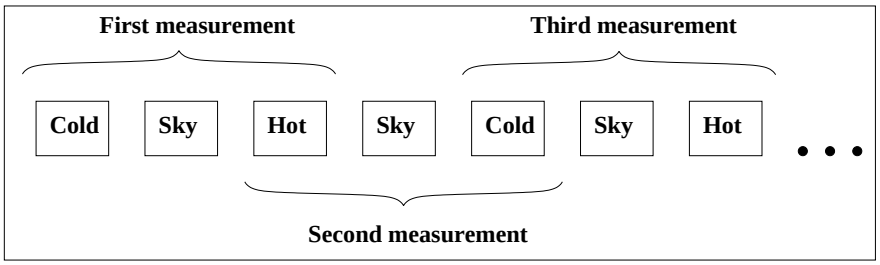

Figure 3.6: A graphical representation of the interleaved calibration technique where each load spectrum is used twice.

power, T_r, which needs to be calibrated on the same scale as the antenna temperature. The antenna is assumed to behave as a pencil beam antenna and $T_a = T_b$. Figure 3.5 shows the calibration principle, where the gain coefficient, Λ, and T_r can be determined by observing two (or more) blackbody emitters, provided the system has a linear output amplification in the measured range.

3.4.1 Initial calibration

There exists a small offset between the measured physical temperature of the calibration loads and their radiated temperature which needs to be accounted for. This is caused by a small temperature gradient between the back of the load where the sensor is mounted and the observed front. Additionally, the loads are not perfect black-bodies at 22 GHz, nor are the windows 100% transparent. By doing an initial calibration with liquid nitrogen and a microwave absorber at room temperature this offset can be calculated. The process itself follows the above given description of microwave calibration. The calculated offset is assumed to be constant within the typical temperature variability (< 5 K) of the calibration loads.

3.4.2 Continuous calibration

Two loads at well-known temperatures are used in a hot – cold load, interleaved, calibration scheme. The cold load is kept at $\approx$45 K, whereas the hot load is kept at $\approx$115 K. By keeping the load temperatures close to the expected atmospheric temperature range second order non-linearities can be minimized (Paganini and Hartogh 2009) and the effective noise temperature is kept at a low level (Jarchow 1998).

During normal operating mode every second spectrum is taken from a load, hot or cold alternatively, the other from the atmosphere. Each atmospheric spectrum is then calibrated against both the hot and cold load spectrum. In this way each load spectrum is used twice, once for the preceding atmospheric spectrum and once for the following one, see Figure 3.6. With each measurement having the same integration time such a routine results in a calibration duty cycle of 50% (Jarchow 1998). To correctly calibrate the retrieved signal the gain coefficient and receiver temperature of the system need to be known. They are correlated by the linear equation:

$$\hat{P}(\nu) = \Lambda(\nu) \cdot (P_a(\nu) + P_0(\nu)), \tag{3.4}$$

where $\hat{P}$ is the power provided by the antenna, P_a is the received power and P_0 is the internally generated receiver power. $\hat{P}$ and P_0 can be calculated from the linear relationship shown in Figure 3.5 by introducing the coordinates (P_{cold}, T_{cold}) and (P_{hot}, T_{hot}), where T_{cold} and T_{hot} are known temperatures of the calibration loads. This has to be done for every single channel of the spectrometer. The calibrated antenna temperature can now be written as:

$$T_a = T_{cold} + (T_{hot} - T_{cold}) \frac{P_a - P_{cold}}{P_{hot} - P_{cold}}. \tag{3.5}$$

In addition, the receiver temperature can be written as:

$$T_r = \frac{T_H P_C - T_C P_H}{P_H - P_C}. \tag{3.6}$$

4 Processing of retrieved data

4.1 Preprocessing of data

While Chapter 2, among other things, describes the theory behind microwave spectroscopy this chapter will shortly describe the actual steps taken to process the retrieved spectrum in order to deduce a vertical distribution of water vapor. The chapter is structured in a way similar to the data processing pipeline. It starts with calibration and data reduction, followed by a short description of the inversion method used – the "optimal estimation method" (the mathematical details can be found in Appendix C). The sometimes counter-intuitive results from this method are investigated and discussed in relation to the inversion process and the impact of the a priori profile and background atmosphere. In the last part an error analysis of the retrieval process is laid out.

4.1.1 Calibration

During the normal operations the physical temperature of the loads and the raw spectrum from the spectrometers are stored in the process control computer, one file for each spectrometer. Together with the known offset temperature the calibration from measured power to absolute power is straight-forward and follow the description in Section 2.2.2.

4.1.2 Data acquisition and averaging of spectra

In the first step the raw spectra from the loads and atmosphere are recalibrated to Rayleigh-Jeans brightness temperature. The outermost channels often contain systematic artifacts caused by switching between the two branches in the CTS. Thus, 96 channels are cut away, the 48 outermost at each side which corresponds to 480 kHz. By cutting the wings there are also more room available to shift the spectrum in frequency which simplifies the process of centering the measured line. Furthermore, spectra with a higher T_b than 250 K are not included in the integration as the assumption concerning the tropospheric correction is not valid for higher atmospheric temperatures than $\approx$ 250 K (Jarchow 1998), see Section 4.1.3.

Centering of the spectrum The output spectrum from the CTS is 40 MHz wide array with containing 4096 brightness temperatures, one for each channel. The exact frequency of each channel is defined by the filter characteristics (a $\frac{sin(x)}{x}$ function). A small offset in the sampling timer, or an LO-frequency which is not exactly correct, can offset the center of the line slightly. Thus the peak of the water vapor line is rarely found in the

center channel. In order to correctly average the two CTS with data from the horizontal and vertical polarization each position in the averaged arrays have to contain information from the same frequency range. Additionally the line center needs to be located in the center position of the array as this is not a free parameter in the inversion. The linefit algorithm does not search for the peak of the spectra, instead it expects the peak to be at the center of the array. If this is not the case and the line peak is offset with respect to the center channel the quality of the linefit will decrease and cause the retrieval to produce an incorrect profile. Being hardware defined the channel-frequency relation does not change over time[1]. An initial offset calibration is done to each spectrometer and is hardcoded into the retrieval algorithm.

Integration of spectrum Depending on the time requirement and the scientific question to be analyzed the spectra can be integrated[2] for shorter or longer times. For instance the search for rocket exhaust plumes may only require a few spectra to be integrated corresponding to an integration time on the order of minutes, others need a few hours up to a week. Normal mode integration simply integrates the spectra serially over the required time. A second method of averaging was developed in order to better resolve the weak daily variability which can be attributed to tidal behavior. It integrates all data from each month in a discrete, temporally defined, moving time frame scheme. For a more detailed description see Section 6.1.1.

4.1.2.1 Polarization averaging

After initial calibration the spectra from the two backends, one for each polarization, are averaged. As the underlying polarizations are orthogonal the retrieved spectra are uncorrelated and can be treated as separate instruments measuring the same spot in the atmosphere, thus the information can be averaged with a normal averaging technique. The standard way of combining two independent measurements (x_1 and x_2) is used:

$$\hat{x} = \left(\frac{1}{\sigma_1^2} + \frac{1}{\sigma_2^2}\right)^{-1} \left(\frac{x_1}{\sigma_1^2} + \frac{x_2}{\sigma_2^2}\right), \tag{4.1}$$

with $\hat{x}$ as the estimate of the combined measurements. The variance of each spectrometer (σ_i) is used as weight in the calculation. In other words the averaging takes into account the signal-to-noise ratio (SNR) of each polarization, the higher the SNR the higher the weight. The new variance, and hence the noise of the new signal can be described as

$$\frac{1}{\sigma_n} = \frac{1}{\sigma_1} + \frac{1}{\sigma_2}. \tag{4.2}$$

If $\sigma_1 \approx \sigma_2$ this results in:

$$\sigma_n = \frac{\sigma_1}{2}, \tag{4.3}$$

which is equivalent of dividing the time needed to reach a certain SNR by two, virtually doubling the time-resolution. In other words, by measuring both vertical and horizontal

[1] Very strong mesospheric winds could induce a Doppler shift on the line center and slightly offset it.

[2] The word integration is used here in the sense of temporally averaging many spectra.

polarization the effective system receiver temperature can be reduced with a square root of two (*cf.* Eq. 2.23)). Compared to the former microwave radiometer at ALOMAR and including design improvements this corresponds to an overall increase in sensitivity of a factor of ≈7, and an increase in the time-resolution of ≈49.

4.1.3 Tropospheric correction

Water vapor emissions from the middle atmosphere are attenuated in the troposphere mainly by water and oxygen. To retrieve a correct middle atmospheric signal this attenuation needs to be accounted for. The strong pressure broadening in the troposphere (>≈ 1 GHz) means that this instrument is insensitive to any vertical variability within the troposphere. Similar to the layer approach used in the forward model the troposphere can be assumed to be one layer, with an effective temperature T_{trpsh}. The transmission through the troposphere can thus be described as:

$$T_b(\nu) = \mathcal{T} \cdot T_{b0}(\nu) + (1 - \mathcal{T}) \cdot T_{trpsh}, \tag{4.4}$$

where $T_b(\nu)$ is the brightness temperature of the measured spectrum, $T_{b0}(\nu)$ the undamped spectrum (above the tropopause) and $\mathcal{T}$ denotes the transmission through the troposphere.

If the cosmic background radiation, the source term in Equation 2.9 also is included Equation 4.4 looks like:

$$T_b(\nu) = \mathcal{T}(T_{b0}(\nu) + T_{cb}) + (1 - \mathcal{T}) \cdot T_{trpsh}, \tag{4.5}$$

where T_{cb} denotes the cosmic background. Seele (1999) explores the impact of the extra term and finds it to be negligible and it is therefore not included[3].

It can be assumed that there is very little information from the strato- and mesosphere far away from the line center (at the line wings) – $T_{b0}(\nu) \approx 0$. Thus T_b(line-wing) only contains the background temperature T_{bgrd}.

$$T_{bgrd}(\nu) = (1 - \mathcal{T}) \cdot T_{trpsh}. \tag{4.6}$$

T_{trpsh} cannot be deduced from the measurements and needs to be manually added to the retrieval. It is however assumed to vary slowly over time thus a daily mean can be used in the retrieval process (Ingold et al. 1998). Transmission can now be calculated as:

$$\mathcal{T} = 1 - \frac{T_{bgrd}}{T_{trpsh}} \tag{4.7}$$

The spectral line at 22.235 GHz is very weak ($\lesssim$ 1 K), thus an average of the whole line can be used to improve the SNR. The original unattenuated signal can then be calculated as:

$$T_0(\nu) = \frac{1}{\mathcal{T}}(T(\nu) - T_{bgrd}). \tag{4.8}$$

[3]The tropospheric attenuation is systematically overestimated by ≈1% if the cosmic background is not taken into account

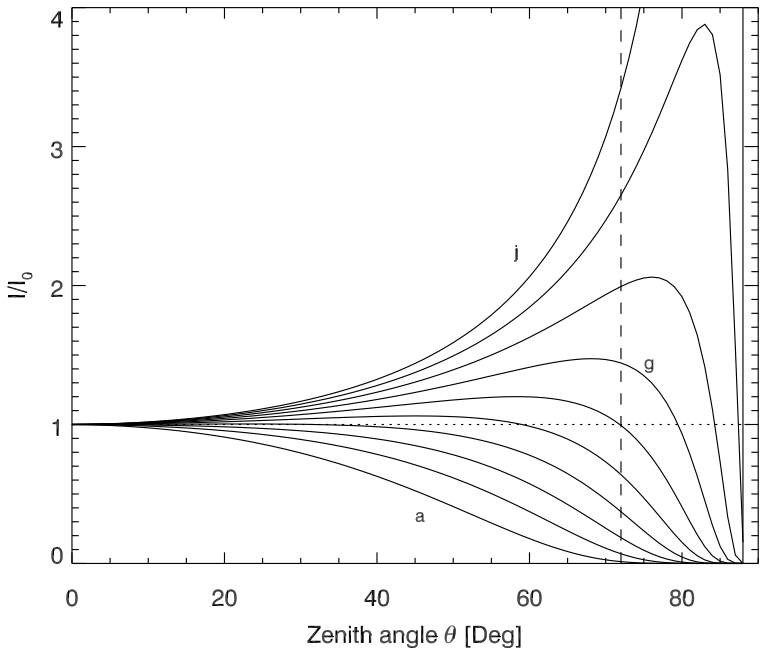

Figure 4.1: The impact of the zenith angle on the ratio between observed and original intensity for different transmissions, (T) (a,b ...j representing 0.1, 0.2 ... 1). The dotted line shows the one-to-one ratio, *i.e.* where an inclination in the observation angle have no impact on the observed intensity. A dashed line shows the chosen elevation angle (72°).

4.1.4 Elevation angle of the antenna beam

The elevation angle is the angle from the horizontal plane to the pointing of the beam. The measured water vapor signal is very weak and by observing the atmosphere at a low elevation angle the observed airmass, and therefore also the observed line amplitude, is increased. This increase in airmass needs to be accounted for in the retrieval. The effect of the increase can be calculated by introducing the airmass factor, m_a, defined as

$$m_a \approx \frac{1}{\cos\theta}, \tag{4.9}$$

where θ is the zenith angle. The above approximation is however only valid for a homogeneous plane-parallel atmosphere and is not accurate for zenith angles greater than $\approx 80°$.

4.1.4.1 The optimal elevation angle

With an increase in the total airmass there is a consequent increase in the tropospheric attenuation. The relation is not linear and is dependent on the tropospheric transmission. To find the optimal elevation angle the increase in line amplitude has to be weighted against the increase in tropospheric attenuation. Both Seele (1999) and Jarchow (1998) explore the mathematical background rigorously so it will only be briefly discussed here. The instrument measures water vapor emissions originating in the middle atmosphere,

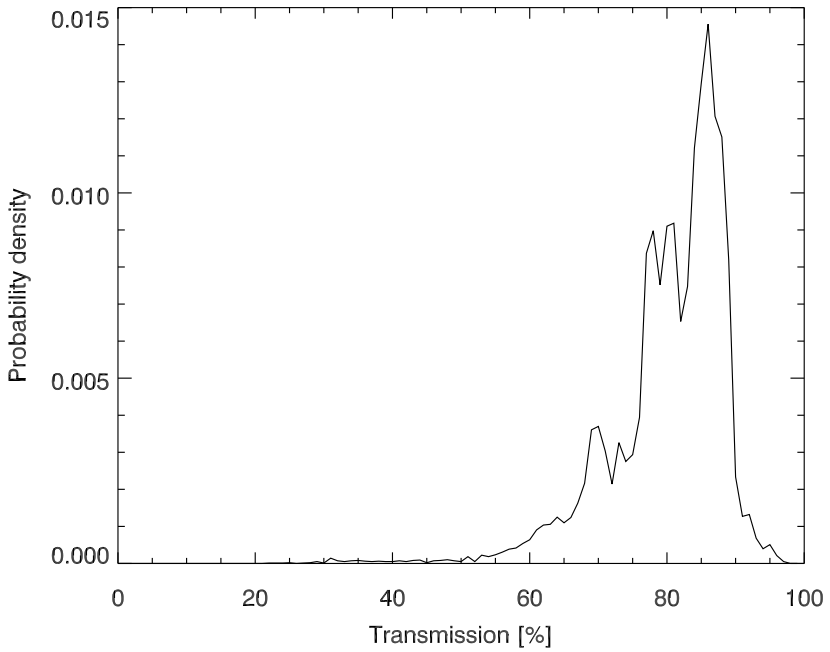

Figure 4.2: Measured transmission over ALOMAR for 2009. The observed brightness temperature is averaged for 5 minutes recalculated into tropospheric transmission according to Eq. 4.7 and rebinned into 1% bins.

and due to the narrow band backend it cannot resolve the lower part of the atmosphere. By assuming the intensity at the top of the troposphere to be $\mathcal{I}_0$, the measured intensity $\mathcal{I}$ can be described as:

$$\mathcal{I} = \mathcal{I}_0 \frac{\exp(-\tau m_a)}{\cos\theta} = \frac{\mathcal{I}_0}{\cos\theta} \mathcal{T}_0^{\frac{1}{cos\theta}} \tag{4.10}$$

where τ is the optical depth, m_a the airmass factor, θ the zenith angle and $\mathcal{T}_0$ the transmission at zero zenith angle. The transmission at the zenith angle, θ, is defined as $\mathcal{T}_\theta$ and Equation 4.10 can be written as:

$$\mathcal{I} = \frac{\mathcal{I}_0}{\cos\theta} \cdot \mathcal{T}_\theta. \tag{4.11}$$

Figure 4.1 shows the impact of different zenith angles on the ratio between the observed and unattenuated intensity. The dashed line marks the elevation angle used at ALOMAR. A dotted line is drawn at ratio 1, it highlights the level at which there is no intensity gain. The optimal elevation angle can be found by differentiating Equation 4.11:

$$\frac{\partial}{\partial\theta}\left(\frac{\mathcal{T}_0^{\frac{1}{\cos\theta}}}{\cos\theta}\right) = \frac{\mathcal{T}_0^{\frac{1}{\cos\theta}} \sin\theta}{\cos^2\theta} \cdot \left(1 + \frac{\ln\mathcal{T}_0}{\cos\theta}\right) \tag{4.12a}$$

$$\longleftrightarrow \quad \theta_0 = 0, \quad \theta_1 = \arccos(-\ln\mathcal{T}_0). \tag{4.12b}$$

It should be noted that the second solution (θ_1 in Eq. 4.12b) only exists for atmospheric transmissions $>\frac{1}{e}$. In other words, for transmissions worse than ≈ 0.37 and $\theta \neq 0$ will always result in a degradation of the signal. Although the mathematical solution indicate an optimal angle for every transmission $>\frac{1}{e}$ it is not implemented for practical reasons. The measured water vapor line is optically thin and the transmission is rarely $<\frac{1}{e}$. Figure 4.2 shows the measured transmission for 2009 over ALOMAR. The brightness temperature used in the calculation is a 5 minute average of the observed instantaneous brightness temperature and the resulting transmission is rebinned into 1% bins. A zenith angle of 72° has been found to be an advantageous trade-off between the opposing effects (Jarchow 1998).

Determination of the elevation angle We have used two different methods of to determine the elevation angle used in the inversion calculations. One is a visual method where the angle of the mirror is estimated relative to the optical table of the instrument itself. This assumes the instrument to be correctly installed in the horizontal plane.

The second method is an absolute calibration of the preset elevation angle relative to the sun. Due to the instrument being immobile there is a limited time-span when the sun is in a favorable position to be used as a source. For southward pointing instruments (located at the northern hemisphere) the sun will pass through the beam for a few days at two separate times of the year. The determination of the elevation angle by use of the sun can be done in two ways, passively or actively. The passive mode requires reasonable clear skies over a long time in order to clearly see when the sun pass through the beam. If the transmission is too low the SNR of the passage of the sun through the beam is too low and the determination of the elevation less exact. By knowing the exact azimuth of the instrument and the time of passage of the sun through the beam the elevation angle can be compared to that of the sun at the time of passage. In the active mode the elevation angle is increased and decreased according to a well defined time-plan. This is possible thanks to a special input on the chopper controller which takes a voltage and translates into an increase (or decrease) in the elevation angle[4]. The exact relation between input voltage and the correlated deviation from the original angle is known thus the elevation angle and observed brightness temperature can be plotted versus time and used to determine the original elevation angle, see Figure 4.3. During this calibration the measurements cannot be used to deduce water vapor profiles. The integration time per scan position is shortened to 3 s in order to achieve a faster and smoother scan.

4.1.4.2 Elevation angle correction

In the forward model the antenna beam is estimated as a pencil beam. In reality antenna pattern has a finite beam-width with a HWHM of 3.5°. A correction for the true and estimated beam size is carried out in the retrieval. It can be shown that while the actual elevation angle is 18° is the efficient elevation angle 17.5° (Jarchow 1998), which needs to be corrected for.

[4]This feature was originally included to the chopper controller to account for a changing roll angle when used in the SOFIA aircraft.

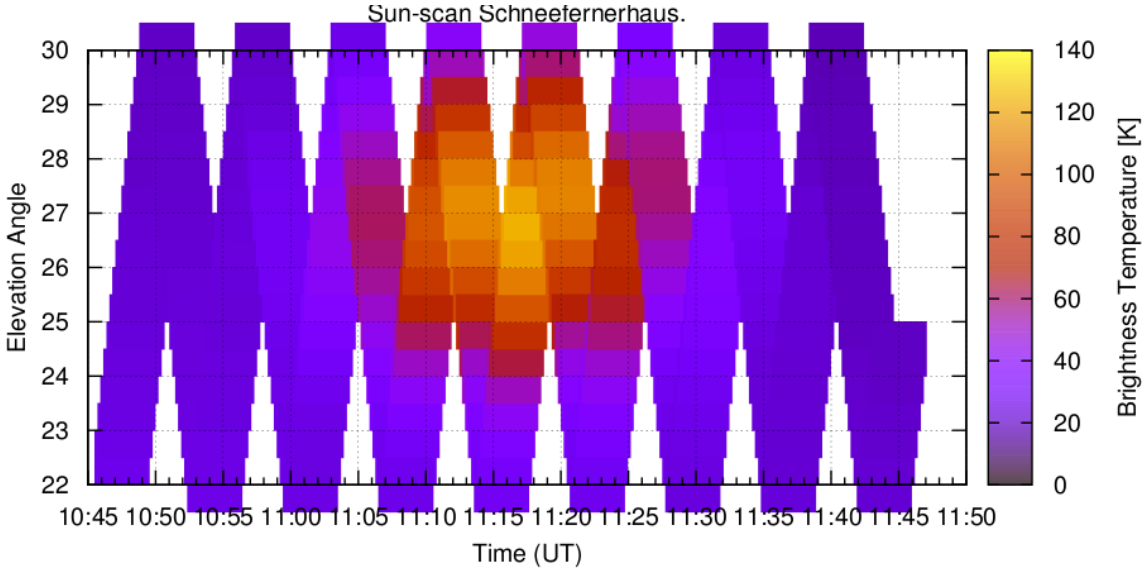

Figure 4.3: The result from a sun scan carried out at Schneefernerhaus on Zugspitze on the 6th of February 2009. The brightest point is assumed to be the location of the sun in the sky. The elevation angle on the y-axis is then the elevation angle of the sun. By knowing the azimuth of the instrument (177°) the true position of the sun in the sky at a certain time can be calculated and compared to the observation. The elevation of the sun is thereafter compared to the calculated of the instrument in order to determine the instrument elevation angle.

4.1.5 The baseline ripple

4.1.5.1 Different baseline components

When measuring a given, emitted, spectral line the retrieved spectra usually contains components other than the molecular line under study. All components of the measured spectral line which are not directly related to the actual measurement are generally denoted as *baseline ripples*. They are caused by imperfections in the instrumental setup and design. It can be a simple offset in the retrieved power or non-linearities in the receiver setup. Commonly there are also periodic modulations of the ideally flat background. Such periodic modulations in the baseline are created by standing waves caused by reflections, somewhere in the instrument. If the cause of the reflection is known the frequency, f, can be calculated by

$$f = \frac{c}{\lambda}, \tag{4.13}$$

where λ is the wavelength and c is the speed of light. In the case of a standing wave the wavelength is the distance between the two reflective media. The reflections can be classified according to their origin, either optical or electronic.

- **Optical baseline components**
  The optical, or quasi-optical, baseline components are created by reflections in the frontend. It can be stray radiation received by the side-lobes of the antenna, or reflections in the windows and/or calibration loads. As discussed in Appendix A.3

most of these reflections can be reduced by moving the optical table. It can be achieved by fine-tuning the movement of the optical table to a multiple of the wavelength of the frequency at which reflections should be suppressed (see Appendix B).

- **Electronic baseline components**
  In general, transmission line reflections can occur at any point where there is a change in impedance, usually at interfaces between components and/or transmission lines. The reflections can be reduced by keeping impedance changes as low as possible, *e.g* by carefully selecting and matching the components, as well as by introducing attenuators and amplifiers at critical places in the signal chain.

Even though it is possible to mathematically reduce the impact of a baseline the first priority should be to design the instrument with a minimized baseline in mind as any modification of the retrieved line might introduce residuals that can affect the atmospheric profile.

The loads are assumed to have a flat spectrum in the measured frequency range and any deviation from a flat line can therefore be assumed to be an instrument artifact. Every single channel is calibrated separately and no correlation between them is introduced at this stage. Thus a simple periodic line influence introduced after the antenna will be eliminated by the calibration process[5]. This is not the case for baseline components which are introduced before the antenna as they will differ between the cold load spectra and the hot load spectra and the calibration will not correctly eliminate the original baseline component. For multiple reflections the situation is more complex and the discussion in Seele (1999) is recommended.

4.1.5.2 Baseline correction

An unprocessed baseline feature will affect the retrieved profile differently depending on the shape, phase and frequency. Baseline features in the wings of the spectra have comparatively low impact on the profile. A result of the fact that the channels in the line-wings contain less information (per channel) about the state of the atmosphere than in the middle of the line[6]. A slope or an offset of the observed line are relatively harmless and can easily be corrected.

The baseline correction applied here fit a line-offset, a slope and a number of periodical baseline modulations (usually $n = 4$) according to:

$$\boldsymbol{y}(\Delta\nu) = \boldsymbol{K}_{\Delta\nu} \cdot \boldsymbol{x} + c + d\Delta\nu + \sum_{i=1}^{n_b} \left[a_i \sin(2\pi\Delta\nu\tau_i) + b_i \cos(2\pi\Delta\nu\tau_i)\right], \tag{4.14}$$

where c is the offset, d is a slope (a proportionality constant) and finally a_i, b_i and τ_i are the fit parameters for periodic modulations of the baseline.

[5] Analogous to flatfield calibration of imaging arrays

[6] For instance, the Doppler broadening of water vapor at 22.235 GHz is ≈30 kHz which corresponds to three channels, thus all information received about the uppermost layer is contained in these three channels. In the line-wings on the other hand one layer can correspond to hundreds of channels.

Offset correction The a priori profile will introduce a constant, frequency independent, offset to the retrieved profile. This offset is removed by the free parameter c and is usually on the order of a few mK.

Slope correction Regardless of baseline ripples the 22.235 GHz is not measured n a flat background. Instead it is superposed on the atmospheric background which is manifested as a background slope. Thus a second free parameter in the baseline correction is introduced, d. Periodic wave-like modulations with a period much longer than the bandwidth of the spectrometer will also be fitted by this parameter (unless they are a pure cosine wave in which case the crest or trough is in the middle of the spectrum).

Wavelike component correction As discussed in Section 4.1.5.1 optical or electronic reflections in the system can give rise to standing waves in the retrieved spectra. They need to be removed for a correct retrieval of the line. These periodic modulations are fitted with the parameters a_i, b_i and τ_i. The amplitude of the modulation can be calculated from a_i and b_i whereas τ_i gives the phase of the modulation. The frequency of the modulation is not a free parameter in the fit and needs to be defined. There are two different approaches when trying to fit the different baseline components. One is to try to find the exact period of the periodic components, and the other to find a good general fit. If the exact period of the baseline is known the first approach is preferable. However to find the exact period of all baseline components is very hard. The other approach, in which a more generally applicable baseline reduction is sought, is somewhat simpler and the result less sensitive to changes in the baseline. The latter approach has been chosen for the default retrieval and use the harmonics of the spectrometer bandwidth as predefined baseline components (80, 40, 20 and 10 MHz). Qualitatively the reasoning behind this approach is as follows. Any reflection in the system will have sub-reflections with harmonics of the original period, with rapidly decreasing amplitude. If it is assumed that any baseline-feature not corrected by a slope or offset is periodic[7] in nature within the bandwidth of the spectrometer it should be able to fit any baseline with a harmonic approach.

4.2 Inversion of the spectrum by the optimal estimation method

4.2.1 The inversion algorithm

The last step in the data-pipeline is to invert the retrieved line in order to deduce a vertical profile. The problem of inversion can be split into two different problems of which the first is the actual inversion. From the forward model we can calculate a line-shape from any given state of the atmosphere. Thus the inversion process is a matter of applying this model to the retrieved line. This is usually an ill-posed problem in the sense that the measured parameters are not enough to constrain the solution – there is an infinite number of solutions. The second part of the problem therefore becomes a statistical problem, namely to find the best estimate of the state of the atmosphere given the retrieved spectra.

[7] Hence non-linear baseline influences cannot be corrected by this approach.

In order to find the best fit it is not enough to ask which is the best mathematical fit of the line. The solution also has to be physically sound. A simple least squares fit can provide a very good fit of the line, but the corresponding vertical water vapor profile is not possible from a physical point of view. A detailed discussion can be found in Jarchow (1998). Due to noise in the measured signal and the infinite number of solutions that exist for any given measurement additional constraints are needed. The method used here to combine the measured emission line and the physical constrains was first described by Rodgers (1976) and has become known as the *optimal estimation method* (OEM). A commonly used constrain is *a priori* water vapor distribution profile of the atmosphere, see Section 4.2.1.3. The a priori profile is not the true profile and an error must therefore be assigned to the profile. This error is described by the covariance matrix. Such an error estimate is important as it is used by the algorithm to find the optimal fit between the measured profile and the a priori profile.

4.2.1.1 Use of background atmosphere

As was discussed in Section 2.1.1.2 the ambient temperature and pressure is important to correctly invert the line-shape to a distribution profile. Currently, there is however no source that can provide continuous in situ measurements of the background atmosphere. Satellite-data exist, but are limited in geographical coverage and temporally inconsistent. Models and assimilated datasets are used instead. Depending on the location of the measuring instrument the available datasets differs. Normally the background atmosphere is constructed from two, or three, different sources. The default setting is to use real weather-data available from the NCEP automailer[8] up to approximately 55 km (0.4 mb)(McPherson et al. 1979), which is the upper level of this data. At higher altitudes it is nudged to the climatological CIRA86 model (Rees et al. 1990). These two datasets are available at any given point of the earth, and can therefore be used for all observation locations. The CIRA86 model overestimate the polar summer mesospheric temperatures and in order to correct for this overestimation the climatology presented by Lübken (1999) is used for ALOMAR. This is unfortunately also a climatology, although based on actual measurement above ALOMAR during 10 years. It should be noted that by using only climatologies at high altitudes the background atmosphere does correctly reflect the dynamics in the upper region. The dynamics of the lower part on the other hand is reasonable well resolved by the NCEP data, see for example the two sudden stratospheric warmings in Figure 2.5.

A complete description of how the background atmosphere is constructed can be found in Seele (1999).

4.2.1.2 Spectroscopic parameters

In addition to the background atmosphere the spectral line parameters also need to be known in order to correctly invert the line-shape (*cf.* Equation 2.11). These parameters are empirically determined and several different versions of "spectroscopic catalogs" exist. By default the JPL catalog is used (Pickett et al. 1998) in combination with broadening (air- and self-broadening) parameters from Liebe (1989) and Liebe et al. (1993). Seele

[8] Located at Goddard Space Flight Center, `science@hyperion.gsfc.nasa.gov`.

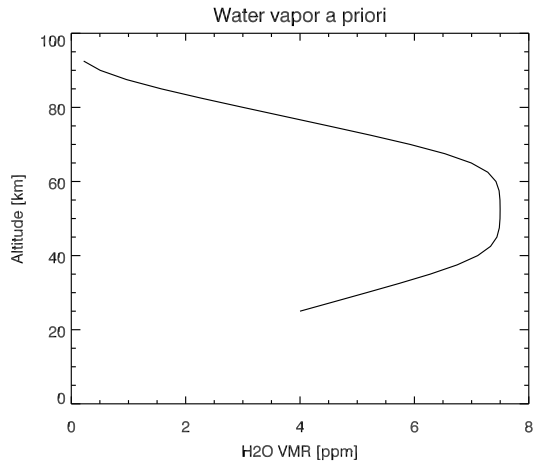

Figure 4.4: The standard a priori profile used for the retrievals. It is constructed by a piecewise linear profile which has been smoothed by a 5 km HWHM Gaussian.

(1999) discuss the influence of the hyperfine structure to the retrieval at higher altitudes, and it is shown that they need to be taken into account. A retrieval with WASPAM with a 24 h integration time will have an error of almost 0.5 ppmv at 80 km. The significance of the error increase with the integration time[9].

4.2.1.3 A priori water vapor profile

The a priori profile plays the role of a virtual measurement and is weighted against the measured profile by the optimal estimation method. Assuming that the a priori profile is a reasonable estimate of the actual water vapor distribution the retrieved profile will never be worse than this. The standard a priori profile used can be seen in Figure 4.4 and is originally described in Seele (1999). In order for the retrieval to correctly weight the measurement and the a priori profile a covariance matrix needs to be supplied. It represents the uncertainty of the profile and a diagonal matrix is used with the diagonal elements being 2 ppmv. Thus the layers in the a priori profile are assumed to be uncorrelated in the retrieval. Rodgers (1976) discuss the possibility of introducing a correlation between the layers in the a priori, but it has been shown to introduce strong, physically impossible, oscillations in the profile and is therefore not used.

4.2.2 The optimal estimation method

A short introduction to the optimal estimation method will be given here. A more extensive mathematical description of the method can be found in Appendix C. The optimal estimation method is a way to find the optimal combination of two or more measurements. Commonly a real measurement is used in parallel with a virtual, or a priori, measurement (see Section 4.2.1.3 for a discussion on the a priori used here). These two measurements are weighted according to their error profiles (represented by their covariance matrices) and the resulting profile is the optimal combination of the two.

[9] According to the retrieval algorithm they are therefore also proportional to the sensitivity of the instrument. The more sensitive the instrument, the more important it is to include these corrections.

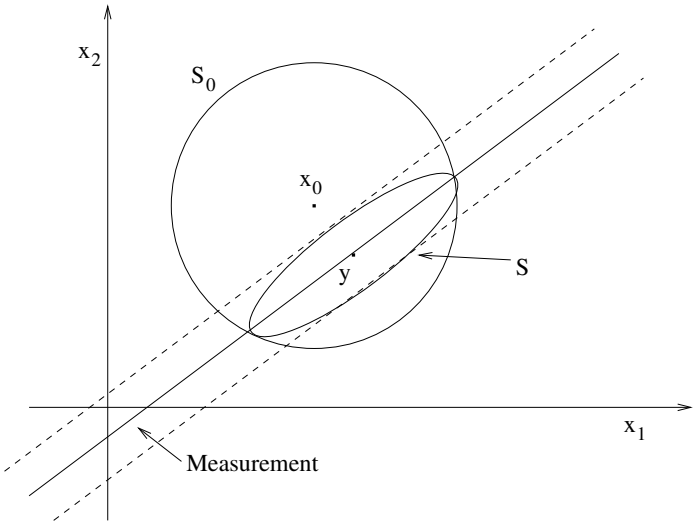

Figure 4.5: A geometrical interpretation of the optimal estimation method. For simplicity the atmospheric model used here only consists of two layers, which can be translated to a 2 dimensional solution space. The solution is then the overlapping region between the a priori and the measurement.

4.2.3 A geometrical interpretation of the optimal estimation method.

In order to visualize the optimal estimation method Rodgers (1976) offer a geometrical interpretation of the method. There are two spaces involved in the retrieval; measurement space, with M dimensions, and profile space with N dimensions. The aim of the measurement is to "map" profile space to measurement space, and consequently the retrieval inverts the process. The number of layers used in the model atmosphere can then be thought of as the number of dimensions N. For simplicity assume that the atmosphere only consist of two layers. This gives a picture similar to Figure 4.5. By measuring the atmosphere the solid line is retrieved with corresponding experimental noise contained within the dashed lines. The a priori profile with corresponding covariance is visualized by the area covered by the circle. With only two layers the true solution is a point, and in this analogy the solid line is the infinite number of atmospheres that would produce the same measured line. The solution according to the OEM is thus contained within the intersection area between the a priori and the measured line. The small ellipse is the error ellipse[10], with the optimal estimate (y) at its center. Note that the intersection is an ellipse and not a truncated rectangle, the surfaces are not clear boundaries but rather contours of probability density functions.

4.2.3.1 Some notes on error bars in the optimal estimation method.

The optimal estimation approach is a well-established method to get reasonable results from atmospheric spectra. The fact that it is widely used is a good measure on the effectiveness of the method. However there are a few counter-intuitive results that one should be aware of when interpreting the results. Errors in measurements, usually depicted one dimensional bars, are a common way to visualize the accuracy of a measurement. Unfortunately this simple method can't be directly applied in the OEM case for different reasons. Following the discussion in Section 4.2.3 it can be understood that there are no single error bars at any specific altitude. Instead, the errors have to be visualized as parameters in a multivariate error space. Recollecting Figure 4.5 and the virtual measure-

[10] Analogous to the error bars in a one-dimensional measurement

ment, the a priori, the error space (or covariance) is the circular region S_0, spanned by the elements in the covariance matrix. By combining the measurement to the a priori the error is decreased to the error ellipse. However representing the error in this way is only possible for a profile with two or maximum three layers, which is rarely the case. Retrieval errors can be presented in another way as eigenvectors, or *error patterns* that span the multivariate error space. For a complete discussion see the original paper, Rodgers (1990), or the interpretation by Jarchow (1998).

4.2.3.2 The Backus-Gilbert approach to the optimal estimation method

Backus and Gilbert (1970) suggested an algorithm to solve inversion problems in geophysics and imaging of the earth. The approach of Backus and Gilbert can be applied in atmospheric inversion with some slight changes. A description of the approach and its applicability to atmospheric problems was discussed by Rodgers (1976) as an alternative to the OEM. Instead of leaving it to the algorithm to find the numerically optimal weighting the different sources of information, a priori and measured data, the covariance matrix is predefined and kept fix. In other words the measured variance at each channel is replaced by the variance given by the covariance matrix, here denoted as $\boldsymbol{S}_y$. The result is that the vertical resolution is fixed, and the measurement noise error will reflect the quality of the profile. A more complete comparison of the two methods for microwave applications is discussed in Jarchow and Hartogh (1995).

4.2.4 The relationship between integration time and vertical resolution

In order to better understand the difference between the original OEM and Backus-Gilbert approach the influence of integration time on the vertical resolution and measurement noise error was investigated. In addition the results underlines some issues that needs to be taken into account when working with ground-based spectroscopy, such as the physical limits in terms of vertical resolution.

Initially six atmospheric profiles were modeled, based on two different instrument sensitivities, represented by the total system temperature (T_S). $T_S = 20$ was used as an estimate of the new instrument (cWASPAM) and $T_S = 150$ for the old (WASPAM). For each instrument sensitivity the profile was modeled with three different atmospheric conditions, represented by changing the atmospheric transmission. $\mathcal{T}$=90%, 50% or 15% was used, corresponding to very good, fair and bad conditions. The modeled water vapor profile was set to be the same as the a priori profile described in Section 4.2.1.3 and the default background atmosphere as well as the normal elevation angle (18°) was used. Actual atmospheric data from NCEP was taken from August the 30th, 2008 above Andøya. The simulations were conducted with full spectral resolution of the CTS (10 kHz) in order to mimic normal operating conditions.

Figure 4.6[11] shows the vertical resolution plotted against the integration time. The vertical resolution is defined as the FWHM of the averaging kernel matrix at the layer peaking at an altitude of 55 km. This plot corresponds to the OEM approach as the

[11]The plot is similar but not identical to a $1/\Delta t$ curve which becomes clear when extremely long integration times are investigated.

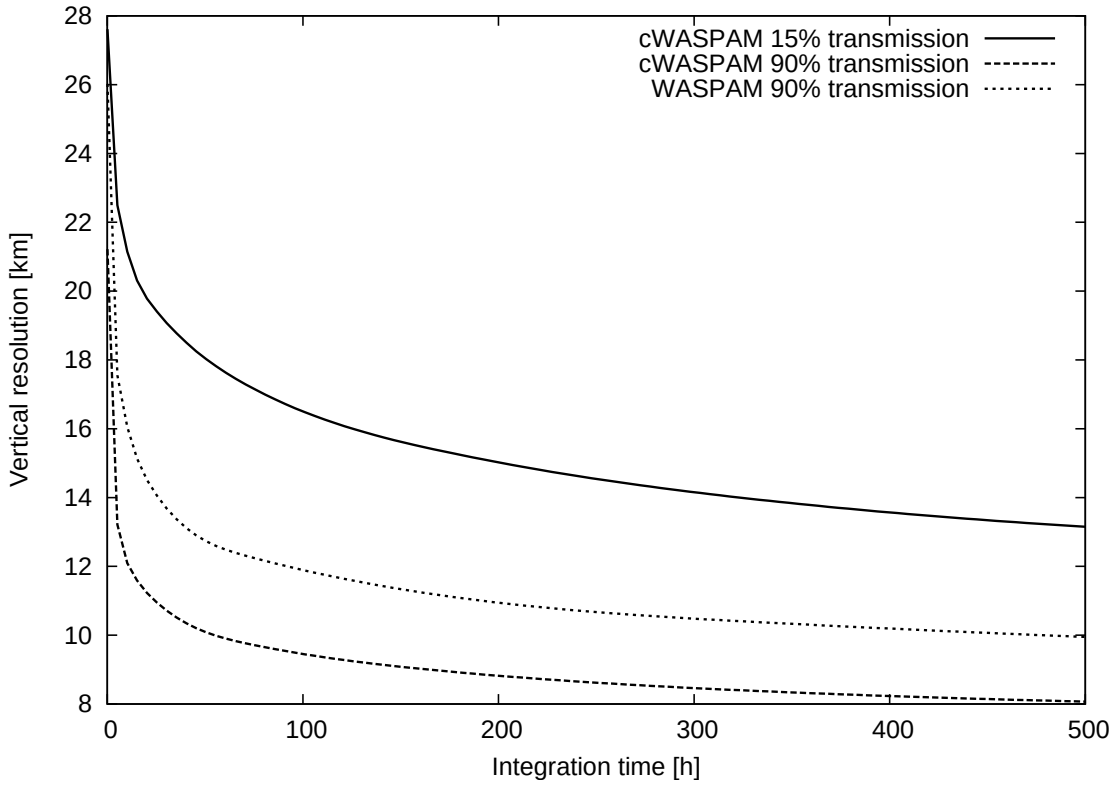

Figure 4.6: The relationship between integration time and height resolution for the OEM. The vertical resolution is given as the FWHM at 55 km.

measurement noise error is constant at 0.17 ppmv for *all* cases (not shown) whereas the vertical resolution increase with increasing integration time. Only the very good and bad conditions for the new instrument and the very good conditions for the old instrument are shown in the plot. However the behavior is similar for the simulations not shown. It should be noted that the very good conditions for the old instrument and the fair conditions for the new instrument overlap almost perfectly (not shown). The better conditions for the old instrument is compensated by the better T_n in the new instrument. Note that the measurement noise error does not change between the two cases.

For the Backus-Gilbert approach on the other hand, see Figure 4.7, the integration time is plotted against the measurement noise error. A similar behavior can be seen here as for the OEM approach, but for a different parameter. The difference between the observational conditions are smaller and the sensitivity of the instrument has less importance as the covariance matrix is pre-defined. Two different covariance matrices of the measured signal was used, $\boldsymbol{S}_y$ = 20 mK and $\boldsymbol{S}_y$ = 100 mK, although only $\boldsymbol{S}_y$ = 20 mK is shown. In the Backus-Gilbert approach the measurement noise decrease with the integration time. On the other hand the vertical resolution is constant. In the case of S_y = 20 the vertical resolution is 17.5 km and by increasing S_y to 100 the vertical resolution is increased to 20.3 km.

An important difference between the Backus-Gilbert approach and OEM is the plausibility of the retrieved profile. If the covariance matrix defined for the Backus-Gilbert case is too narrow, *i.e.* the variance is much smaller than the variance in the measurement

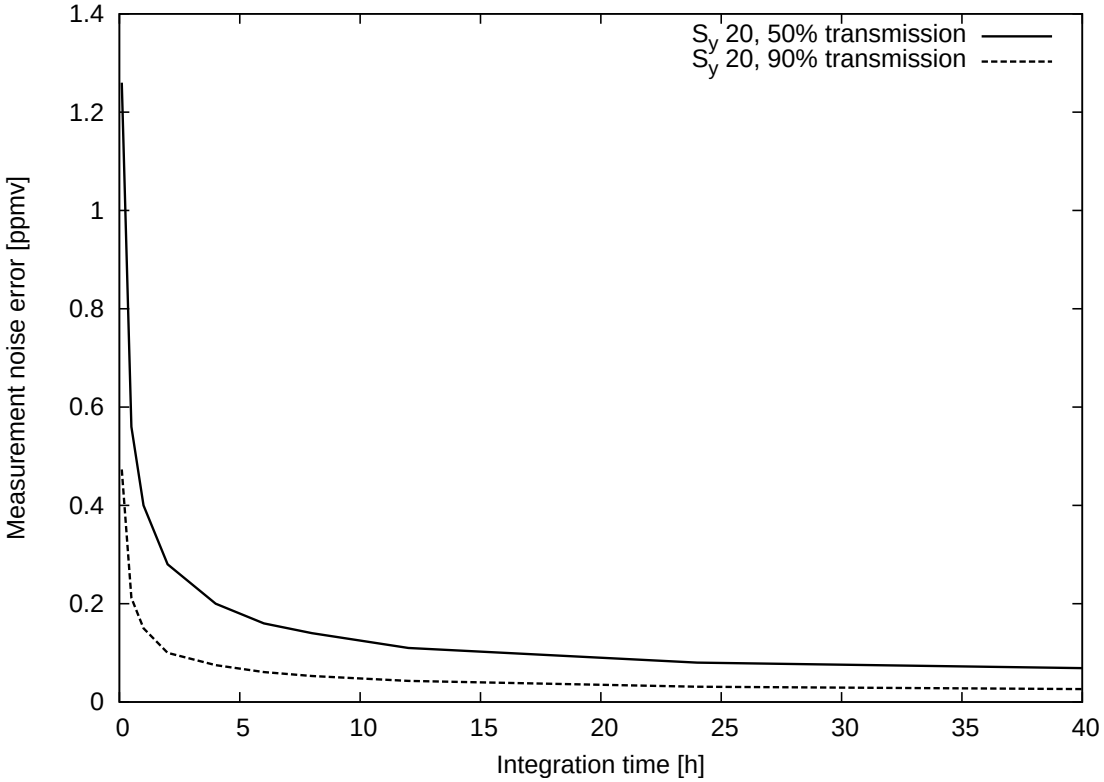

Figure 4.7: Similar as Figure 4.6 but for the Backus-Gilbert approach. The vertical resolution is constant (17.3 km) and instead the measurement noise is improved as the integration time increase. The given measurement noise is measured taken from the 55 km layer.

the resulting profile will contain oscillations. Qualitatively this is can be understood as the algorithm trying to use noise as a true part of the signal and fit a profile to it. If, on the other hand, very bad observing conditions occur with the OEM the profile will tend to the a priori. In fact, the profile retrieved will under the worst conditions (no input signal at all) be exactly the a priori profile. As long as this is taken under consideration OEM will always produce a useful profile.

4.2.5 Influence of the background information

Aside from the pure spectroscopy parameters, which are needed for the forward model to relate a line-shape to a distribution profile, the inversion is also dependent on additional, external, background information such as the a priori profile and the background atmosphere. The following section will investigate the influence of this information on the retrieved profile.

4.2.5.1 Influence of the a priori profile

It has been stated that when the retrieval is conducted with the OEM the a priori profile will “save” a bad measurement in the sense that the profile will tend to the a priori profile. Additionally, a profile retrieved with the OEM will contain more information from the a

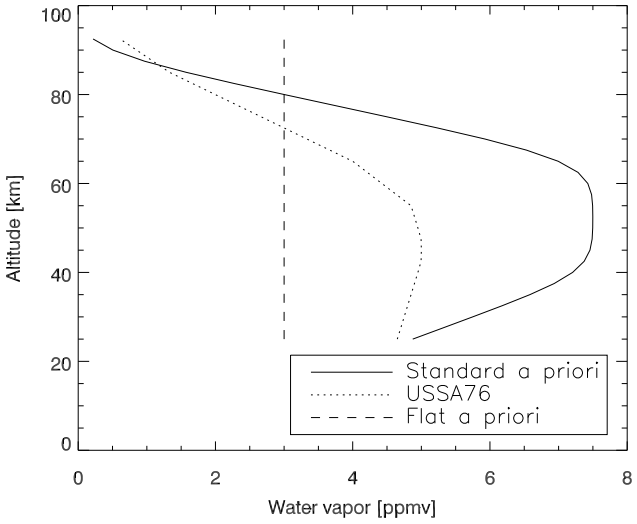

Figure 4.8: The different a priori profiles used in the sensitivity investigation. The solid line corresponds to the default a priori profile used, the dashed is taken from the U.S. Standard Atmosphere 1976 for mid-latitude winter conditions and the dotted corresponds to a static water vapor profile of 3 ppmv.

priori in altitude regions where the instrument sensitivity is low. The question then arise how much does the a priori profile influence the measurements during normal operation conditions.

To investigate this three different profiles were used to retrieve real data from July 2009. The three different profiles can be seen in Figure 4.8, where the solid line is the default a priori profile used in the retrievals, the dashed line is taken from the U.S. Standard Atmosphere 1976 (USSA76) and corresponds to winter conditions at a mid-latitude location. This profile is also used in the comparison campaign at Zugspitze discussed in Section 5.1.1. Finally a deliberately incorrect a priori profile was used, the dotted line, which is a static water vapor profile of 3 ppmv. In order to facilitate the analysis and comparison of the difference in the retrieved profiles the distribution for the month in question with standard settings is shown in Figure 4.9. The difference in the profiles can be seen in Figure 4.10. Figure 4.9 include a slightly larger portion of the retrieved atmosphere to clarify the implications of the lower instrument sensitivity at decreasing altitudes where the averaging kernels are close to zero.

In the case of the difference between the standard a priori and USSA76 a priori the difference is less than 0.25 ppmv in most of the middle atmosphere. The flat a priori profile introduce somewhat larger errors as the algorithm is having trouble to smooth the true profile to the flat profile. A striking feature in Figure 4.10 is the stable, and large, difference at low altitudes. This is expected as the averaging kernels at these altitudes are zero and OEM will take all information from the a priori profile. A similar process is present at high altitude although less pronounced. As illustrated in Figure 4.8 the USSA76 a priori has less water than the standard a priori. This results in less water in the regions where most of the information is taken from the a priori, a fact that can be seen in Figure 4.10. Higher up, where the profile run free the algorithm try to compensate for the forced lower amount of water vapor at low altitudes. Thus the retrieved water vapor is higher than the standard profile. This is a general feature – if the water vapor provided by the a priori profile is lower than the actual atmospheric water vapor at low altitude it will be reflected by an overestimate of the retrieval at higher altitudes. Thus, not only will the absolute values

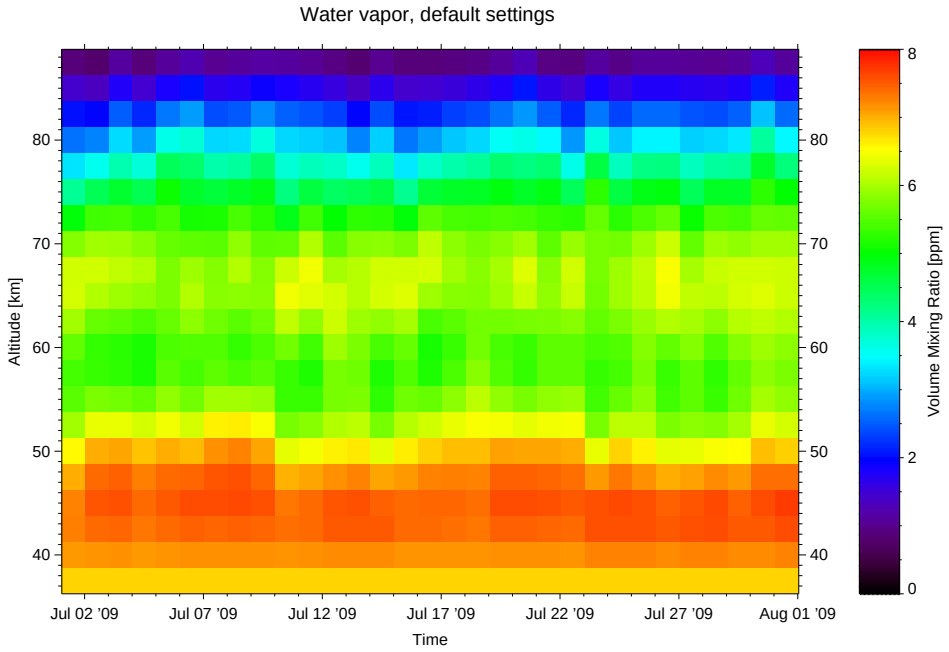

Figure 4.9: The water vapor distribution for July 2009 using standard settings. This implies a falling sphere modified CIRA86 and NCEP background atmosphere. The default a priori profile as shown by the solid line in Figure 4.8 is used. In order to minimize the impact of noise a 24 hour integration time has been used.

of the profile be erroneous, but also the vertical distribution as the algorithm account for the underestimation at one location by adding water to another (or vice versa).

Some weak dynamical differences can be seen in the difference plot. They reflect the behavior of water vapor at low altitudes and affect the profile at higher altitude by the same reason as described above. The same is true for the difference plot between the static a priori profile (3 ppmv) and the standard profile. The a priori profile is obviously wrong, but the same behavior as between USSA76 and the standard a priori can be seen. It seems that the shape and absolute values of the a priori in the sensitive region is of less importance whereas the amount of water vapor in the region where the instrument is not sensitive are of much greater importance. However the differences are very small and in general it can be said that the retrieved profile is not very sensitive to the a priori profile.

4.2.5.2 Influence of the background atmosphere

Similar to the a priori profile the temperature in the background atmosphere is an external information source needed for the retrieval. As described in Section 4.2.1.1 the background atmosphere is a combination of true atmospheric data and models. Different models provide slightly different background temperatures and this section will investigate how that affects the retrieved water vapor profile. As in the previous section data from July 2009 has been used for the comparison. Thus monthly behavior according to default conditions can be seen in Figure 4.9.

In the following background atmospheres the lower part is taken from NCEP data, whereas the upper part differs. It is either taken from the CIRA86 model, a modified

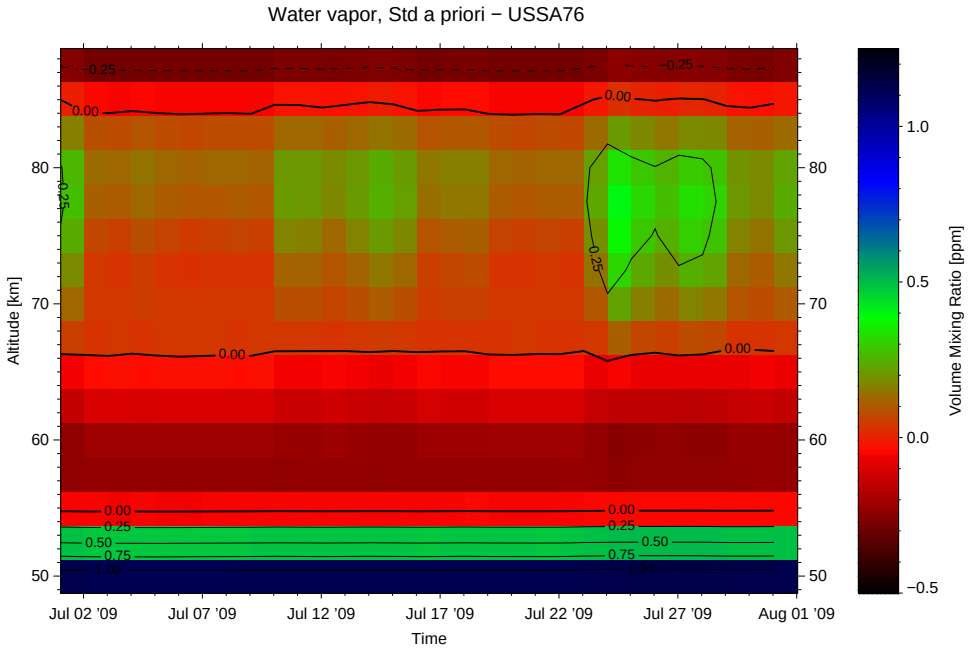

(a)

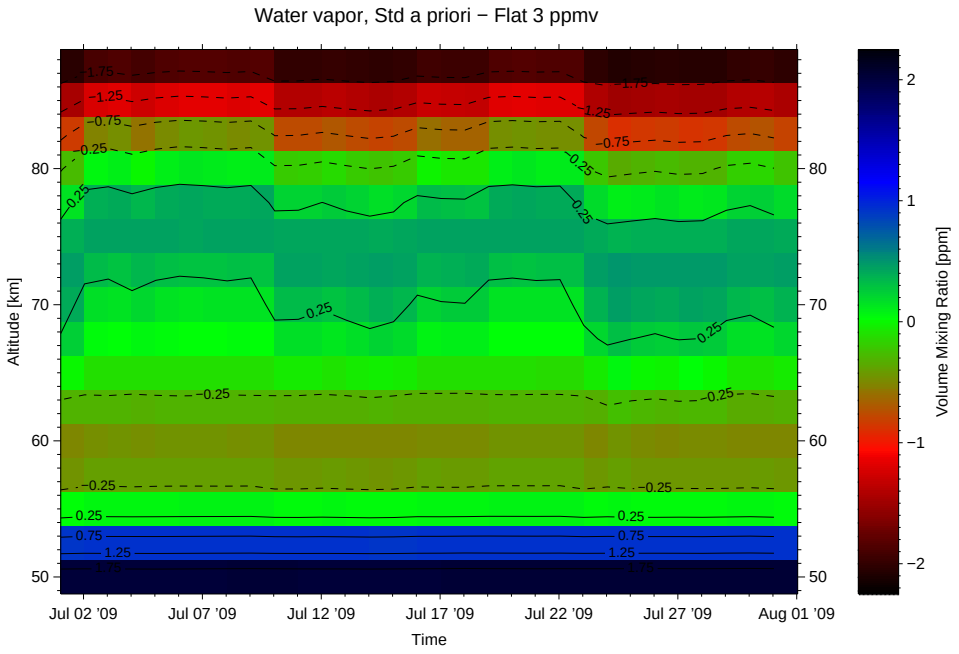

(b)

Figure 4.10: Different water vapor profiles according to difference on the a priori profiles. Fig. 4.10(a) shows the difference between the standard a priori case and the USSA76 case and Fig. 4.10(b) shows the difference to a flat a priori case.

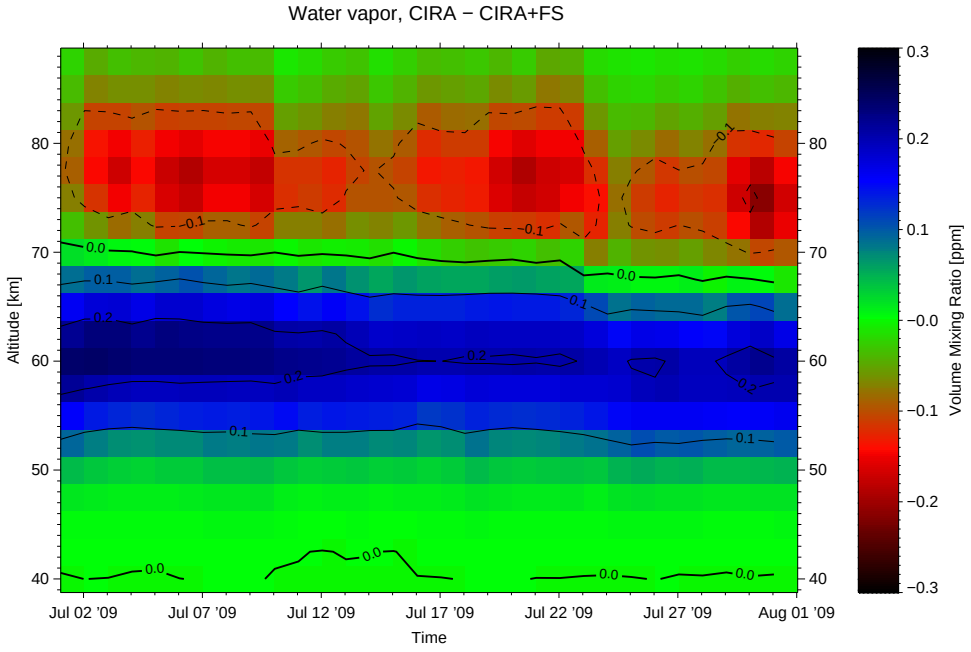

(a)

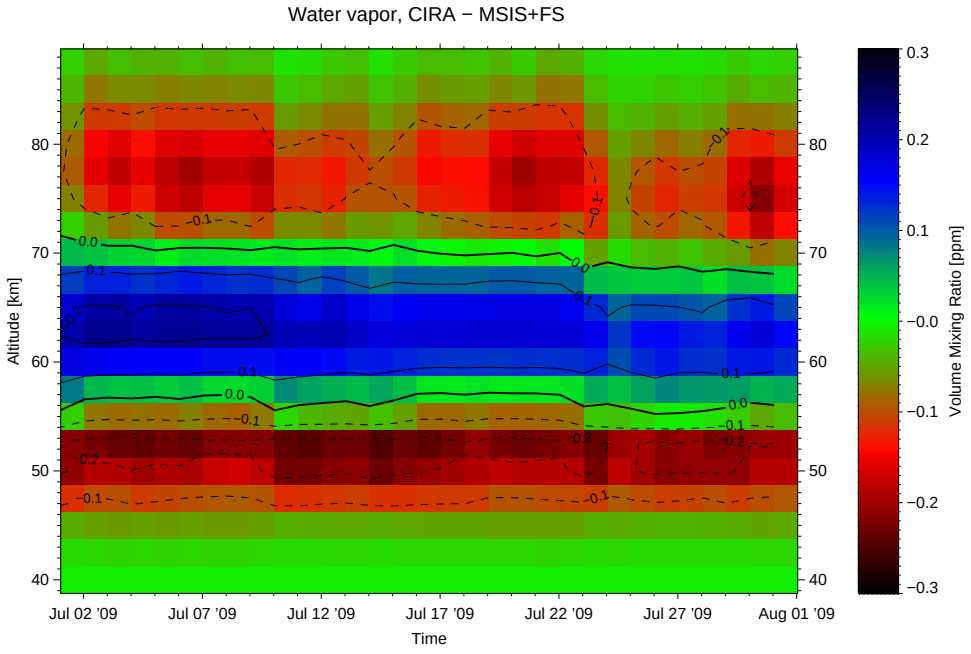

(b)

Figure 4.11: The difference in retrieved water vapor volume mixing ratio depending on the background temperature used. The profile retrieved with a pure CIRA86 background nudged to NCEP data is taken as the default retrieval against which the others are compared. Fig. 4.11(a) shows the difference to the CIRA86-model with added falling sphere temperatures from Lübken (1999) and Fig. 4.11(b) shows the difference to MSIS temperatures.

CIRA86 model by falling spheres data (Lübken 1999) (hereafter noted as CIRA-FS) or the MSIS90 model (Hedin 1991) modified by the same falling sphere data (denoted MSIS-FS). The pure CIRA86 background is a bit colder around the stratopause than CIRA-FS. However, at higher altitude CIRA-FS has a much steeper negative gradient and is almost 10 K colder at 80 km. In the MSIS-FS data a strong inversion layer around the stratopause is present, but in general the MSIS-FS data is controlled by the falling sphere climatology. Both models (CIRA86 and MSIS90) have a monthly time-step thus the only short term variability comes from the NCEP data. When adding the falling sphere data to the monthly models a warmer stratopause in the beginning of the month is visible. The falling sphere climatology is a daily model and therefore add some temporal variability to the background.

The difference in the retrieved water vapor between the backgrounds can be seen in Figure 4.11. The profile retrieved with only the CIRA86 model is taken as the default retrieval against which the others are compared.

There is no appreciable difference between CIRA86 and CIRA-FS in the upper stratosphere. Higher up in the atmosphere the pure CIRA86 model provides slightly higher water vapor amounts than CIRA-FS. This is the case up to approximately 70 km where the CIRA86 background show less water than the CIRA-FS background. This is consistent with the changes in temperature. Below 70 km the CIRA-FS background have higher temperatures than CIRA86 and above lower temperatures. In the case of the MSIS-FS background the temperature differences and especially the inversion layer around 50 km is clearly visible in the retrieved water vapor amounts.

The retrieved small-scale dynamics seem to be weakly affected by the background atmosphere. For example in the CIRA86 to CIRA-FS comparison there are three events in the upper mesosphere differing between the backgrounds. They are actually an artifact of the retrieval process and stem from the difference in the lower layers.

4.2.5.3 Concluding remarks

Both the impact of the a priori profile and the background atmosphere have been investigated in order to find out how strongly they affect the retrieved profile.

The impact of the a priori profiles is mainly concentrated to the layers where the instrument is not sensitive. It is shown that even large discrepancies between the used a priori profile and the true profile only slightly affect the sensitive region. However, largely incorrect a priori profiles will introduce small oscillations as the algorithm compensate for the under- or overestimate of water vapor. This can be understood in terms of total water vapor. The retrieved line amplitude constrains the total amount of available water vapor according to the measurement. When there is an overestimation of water vapor in one region the algorithm will compensate this by reducing the amount in the adjacent region.

Similar to the impact of the a priori profiles the impact of the background atmosphere is weak. For the cases tried here the difference rarely exceed 0.2 ppmv in the middle atmosphere ($\approx$5%). Due to the lack of dynamical features in the monthly climatologies the differences can be seen as offset differences caused by incorrect background temperatures (and pressures). The falling sphere climatology has a higher temporal resolution and will therefore introduce a somewhat higher variability in the measurements. In the default background, there are relatively large changes in the water vapor on the 10th and 23rd of

July. These events are also visible in the difference plot, where they turn up as differences in the upper part of the atmosphere. Thus even though there is only a offset difference in the background it will cause dynamical changes in the retrieved water vapor. This is to be expected as the retrieved water vapor is not linearly related. In general it can be said that for the same line a warmer atmosphere will increase the amount of water vapor in the retrieved profile.

4.3 Error analysis

The shape of the retrieved water vapor profile is affected by many different sources; internal and instrumental as well as external information of the state of the background atmosphere. How some of them influence the result has been discussed in earlier sections, for example the a priori profile and background atmosphere in Section 4.2.5.2. This section will present an estimate of how strongly the uncertainties correlated to these parameters affect the retrieved profile. Although the instrument presented here itself is new and differ in some ways significantly from the earlier WASPAM instrument the error analysis is very similar. Jarchow (1998) and Seele (1999) include an extensive discussion on how the errors are calculated and how the retreived profiles of WASPAM are affected by uncertainties in different parameters. The results there are denoted as the WASPAM errors. It is important to remember that the new instrument is more sensitive in the sense that it has a much higher signal to noise ratio — but it is based on the same concepts and use essentially the same retrieval process as WASPAM and the errors are therefore to a large extent similar. A difference can however be seen in the measurement noise which represents the Gaussian noise of the instrument, which is less for cWASPAM than WASPAM. The discussion by Jarchow (1998) is slightly more extensive as it also includes errors due to uncertainties in the antenna model and window transmission[12].

The total error as a function of altitude can be seen in Figure 4.12. The errors presented are explored by changing each parameter and calculating the difference of the retrieved distribution to the original profile for a 24 hour integration time. In general there are no significant differences between the errors at different integration times except for few cases. At high altitudes (>75 km) the longer the integration time the larger the error will be for an incorrect pressure broadening parameter and elevation angle. Errors related to the background atmosphere affect the whole profile and also increase with the integration time.

4.3.1 Errors caused by the forward model

The task of the forward model is to provide a modeled spectral line according to the physical relations described in Section 2.1.1. Some of the parameters used are not exact, such as the pressure broadening parameter, but empirically measured. Others such as the background atmosphere is a combination of modeled and actual measurements. These uncertainties propagate through the retrieval and create further uncertainties, or errors, in

[12]He also include errors due to the filter function which are of no interest for the new instrument as it has no filterbank backend.

the retrieved profile. The forward model used for the new instrument is unchanged and the errors correlated to it are therefore the same as the WASPAM errors.

Tropospheric correction Uncertainties in the determination of the tropospheric transmission can introduce incorrect scaling of the measured middle atmospheric spectra (Equation 4.8). To determine the tropospheric transmission the measured brightness temperature needs to be known together with an estimate of the tropospheric temperature. By assuming an error of the measured T_b of 1 K and 5 K for the estimated tropospheric temperature the resulting error is on the order of 1%. Note that the method of determining the tropospheric transmission has not changed between this retrieval and the one used for WASPAM, thus the error correlated to the tropospheric correction is identical for both systems.

Background atmosphere The influence of the background atmosphere is discussed from a qualitative point of view in Section 4.2.5.2 but the question on how the retrieved profile differ from a true profile persist. To uniquely answer the question a true pressure and temperature profile is needed for comparison. Seele (1999) tries to solve the issue by closely studying the retrieved profile at two different times, one by exploring the influence of the given uncertainty in the temperatures provided by the falling sphere climatology (FS) in Section 4.2.5.2, and the other by using a LIDAR temperature profile as the true temperature profile during a SSW. Only the FS case is shown in Figure 4.12. For the first case the estimated standard deviation in the FS climatology is used to calculate the variability in the retrieved profile caused by uncertainties in the background temperature. The CIRA86 climatology is considerably warmer (up to 10 K) than the FS climatology in the summer mesosphere[13] which results in a higher water vapor volume mixing ratio in the mesosphere. The difference is present up to the upper limit of the instrument, but at altitudes above 75 km the error introduced by an incorrect background decrease as the sensitivity of the instrument decrease.

For the second case LIDAR temperature measurements are used as the true background atmosphere. Compared to the CIRA86 climatology there is a large temperature difference (≈80 K at 40 km) at lower altitudes (30 – 50 km) due to the ongoing SSW. These large temperature differences only inflict a relatively small VMR differences (≈10%) due to the altitude sensitivity of the instrument. Again the temperatures provided by CIRA86 are warmer than the actual temperature which result in a wetter atmosphere.

The error attributed to the background temperature in Figure 4.12 are calculated by changing background temperature in the forward model ±5 K.

Spectroscopic parameters All empirical parameters used in the line-shape functions are bundled together as spectroscopic parameters. Most of them are empirically derived and suffer therefore from uncertainties. The parameters which has the largest influence on the retrieval are the pressure broadening constant and the line-intensity. To explore the impact on the profile the pressure broadening constant is varied by ±1014 Hz/Pa (≈3.5%)

[13] There is unfortunately no year round climatology derived from falling sphere measurements.

and the line-intensity by 6.81e-21 m^2Hz ($\approx$.5%)[14]. The resulting error is at some levels is higher than the measurement noise for a 24 hour integration time.

4.3.2 Errors caused by the inversion

Errors that are associated with the inversion method, the two right hand side terms of Equation C.16c, are the measurement error and the null space error. Both WASPAM and cWASPAM use OEM for the retrieval thus there is no difference in the errors introduced by the retrieval. However a short discussion on each of the separate errors are given below.

Null space error The null space error can be thought of as the error represented by the limited vertical resolution of the retrieval. It is the subspace spanned by all possible solutions allowed by the uncertainty of the a priori which cannot be uniquely determined by the measurement. Small variations between the layers are not resolved by the current retrieval method which will introduce an error as a consequence of the smoothing effect by the averaging kernels. This is the null space error, which is sometimes also called the smoothing error. Being a technical artifact of the estimation method it does not express anything about the measurement *per se* and is therefore not included in the total error. It was introduced in Rodgers (1990) which include a general discussion on its applicability. Jarchow (1998) explore the null space error in a graphical representation and how it relates to ground-based microwave spectroscopy.

Measurement noise error According to OEM the stochastic noise, ϵ_y, in each measured spectra will be represented as the measurement noise error (see Section 4.2.2). In Figure 4.12 it can be seen that the error associated with the measurement noise is approximately 5% up to 70 km and above that it increase rapidly. It is important to remember that the measurement noise error does not decrease linearly with a longer integration time. Hence a sensitive instrument will only be slightly less affected by stochastic noise than a less sensitive instrument, see the discussion in Section 4.2.3.1. The optimal estimation method tries to find the optimal weighting between a noisy measurement and the a priori profile, the higher sensitivity will be translated into a higher vertical resolution (the averaging kernels change shape). As long as the estimated error of the a priori profile is unchanged the optimal weighting will be the same, only the averaging kernels change with varying observational conditions or instrument sensitivity. Thus the errors introduced by the measurement noise are only slightly smaller than for WASPAM although cWASPAM is much more sensitive.

4.3.3 Instrumental errors

The instrumental errors are caused by uncertainties in how the instrument is numerically represented within the retrieval. It also contains the uncertainty of how well the elevation angle of the antenna, transmission losses in the windows and antenna parameters are

[14]The uncertainty of the parameters are the same as used in an intercomparison campaign, ARIS, which is expected to be published first half of 2011.

known. The two latter parameters are investigated in detail in Jarchow (1998) and are so small, (<1%), that they can be ignored here.

Determination of elevation angle The difference in the actual elevation angle, and the one used while calculating the observed airmass (cf. Equation 4.9) needs to be included in the error analysis. The method of determining the elevation angle has changed with the new instrument because of a new instrumental design. However the angle cannot be determined with a better precision than before (±0.5°). Thus, the error introduced by the uncertainty in how the elevation angle is determined is identical to the WASPAM error. The error profile shown in Figure 4.12 is the result of varying the elevation angle θ with ±0.5°.

Frequency shift The finite channel width of the CTS might introduce an error in the inversion process due to the sampling of the line. If the channel width is denoted ν_{ch} the line center can essentially vary with $\pm\frac{\nu_{ch}}{2}$ and still be measured within the center line. As the backends are averaged before inversion the propagation of an uncertainty in the line center needs to be investigated. The total uncertainty is then

$$\Delta\nu_c = \frac{\nu_{ch}}{2} + \frac{\nu_{ch}}{2}. \tag{4.15}$$

Note that the averaging between the backends only average the intensity at each channel, they are assumed to be correctly aligned from the line center point of view. The channel resolution of cWASPAM is twice as good as WASPAM but with the averaging of two backends the introduced error due to the finite channel width is the same. Due to pressure broadening this error is almost solely an issue at altitudes above 70 km. Although if the hyperfine structure of the water vapor spectrum is not taken into account the error is visible already at 50 km and above 70 km the error is larger than 10% (see Seele (1999) for a more detailed discussion about the hyperfine structure).

4.3.4 Concluding remarks on the error analysis

The sum of all errors for the default retrieval with the OEM can be seen in Figure 4.12. It turns out that even though a multitude of different parameters are used in the retrieval the single most important component of the error profile is the measurement noise. It may seem a bit counterintuitive that the measurement noise is the same as for the WASPAM instrument when the new instrument is so much more sensitive. The reason is again the retrieval process, and the difference in the sensitivity between the instruments is seen in their respective averaging kernels. It is interesting to note that decreasing the uncertainty in many of the parameters used in the retrieval will only marginally improve the measurement. Nor will a much more sensitive instrument be burdened with a proportionally smaller measurement noise, although the smoothing error will decrease between the atmospheric layers and the vertical resolution increase.

It should however be noted that the measurement noise and the how well small-scale variations is resolved by the instrument is to a certain extent dependent on the retrieval method. As is seen in Figure 4.7 the measurement noise can be further decreased if the

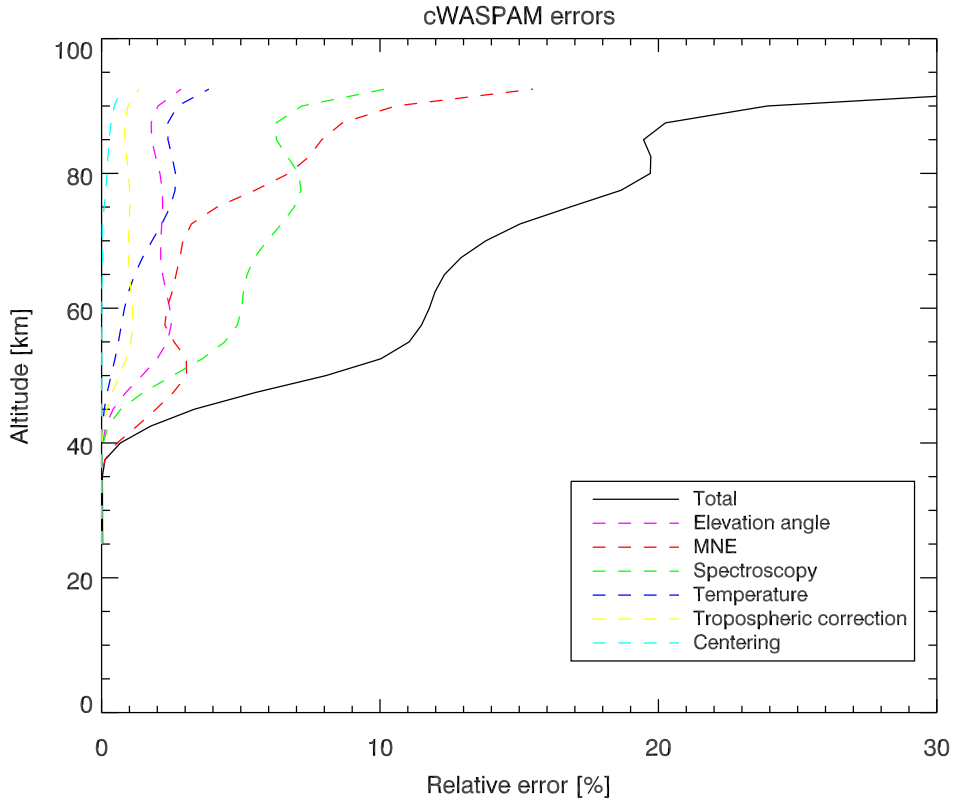

Figure 4.12: Total error in the measurements, where each component is derived by modeling an error according to the respective description in Section 4.3. The integration time used is 24 hours. The largest error components are the measurement noise and the spectroscopic uncertainties.

vertical resolution is kept constant. Thus depending on the application it might make sense to use for example the Backus-Gilbert method instead of the OEM.

5 Observations of mesospheric water vapor

5.1 Validation of measurements

In order to validate the retrieved water vapor profiles it is of interest to know how the retrieved measurements compare to other instruments. Not only comparisons with similar instruments are of interest but also comparisons with instruments measuring water vapor in general, such as satellites measuring water vapor at different frequencies. Unfortunately the former instrument (Hartogh and Jarchow 1995a) (the WASPAM frontend) at ALOMAR broke down and did not produce any reliable profiles at the arrival of the herein described instrument. However, the instrument located at Zugspitze has been involved in an intercomparison campaign. The campaign is expected to result in a paper describing the first co-location intercomparison of three different microwave instruments measuring the 22.235 GHz rotational line of water vapor. All the instruments are observing the sky in the same direction and at the same elevation angle which further enhance the validity of the intercomparison.

5.1.1 Comparison with ground-based instruments

Water vapor radiometers are observing the middle atmosphere at several places over the world and the "global" dataset is continuously growing. An advantage of ground-based instruments compared to satellites is the fact that they more or less continuously observe the atmosphere. However, a temporally complete dataset from only one location cannot constrain the global transport patterns of water vapor. Thus, measurements from many instruments need to be compared and correlated. In order for this to be possible it is of importance to know how the different receiver setups and backends behave in comparison to each other. Global intercomparison campaigns have been conducted with instruments at different locations in order to resolve this issue. Such comparisons, on the other hand, suffer from the fact that they measure at different locations and are dependent on external input as a baseline comparison. In the case of a large intercomparison campaign recently conducted by Haefele et al. (2009) the EOS-MLS[1] instrument onboard NASAs EOS satellite AURA was used (Waters et al. 2006). In order to avoid the dependency on an external source for the comparison an intercomparison campaign started in the beginning of 2009

[1]The Microwave Limb Sounder (MLS) is one of four instruments onboard NASA Earth Observing System (EOS) Aura satellite.

where all participating instruments were located at the same place, measuring the same atmospheric region.

During the ARIS[2] campaign (January 15, 2009 to April 22, 2009) three different ground-based microwave radiometers were observing the water vapor above Zugspitze. One of the instruments was the one described herein, the others were operated by the Institute for Applied Physics (IAP) at the University of Bern and the Institute for Meteorology and Climate Research - Atmospheric Traces Gases and Remote Sensing (IMK-ASF) at Karlsruhe Institute of Technology (KIT). IAP Bern participated with MIAWARA-C[3] (Straub 2008) and IMK-ASF with MIRA 5[4] (Hochschild et al. 2008). The instruments differ in many ways, notably in the receiver setup and backend type, for a comparison see Table 5.1.

It is of interest how these three instruments compare to instruments at other locations and in order to generalize the campaign it was decided to include a comparison with water vapor profiles from EOS-MLS. The comparison between cWASPAM and EOS-MLS can be found in Section 5.1.2. Some work related to the comparison of the data, as well as discussion of the results, still needs to be carried out thus no results from the campaign can be presented here. However the campaign is expected to end in a publication during the first half of 2011.

Table 5.1: Instruments participating in the ARIS campaign.

Instrument	cWASPAM3	MIRA-5	MIAWARA-C
Operated by	MPS	IMK-ASF	IAP-Bern
Receiver type	Cooled total power	Cooled total power	Correlator
Backend type	CTS	AOS/FFTS	FFTS
Total bandwidth [MHz]	40	1300	500
Channel bandwidth [kHz]	10	62	30
Receiver noise [K]	≈30	≈170	N/A

5.1.2 Comparison with MLS

During the Zugspitze campaign a number of co-located profiles from EOS-MLS have been recorded and an intercomparison between the cWASPAM and EOS-MLS profiles has been carried out. It is important to note the differences in the retrieval before drawing any conclusions from the comparisons. Therefore a short description of EOS-MLS will follow and thereafter the actual comparisons.

5.1.2.1 EOS-MLS

EOS-MLS use limb-scanning technique to retrieve profiles of water vapor from the stronger, optically thicker, 183 GHz line. The altitude resolution attained is ≈4 km below the stratopause and increase to about 10 km at high altitude. Horizontal resolution is ≈7 km

[2] Alpine Radiometer Intercomparison at the Schneefernerhaus
[3] Middle Atmosphere Water vapor Radiometer
[4] Microwave Radiometer

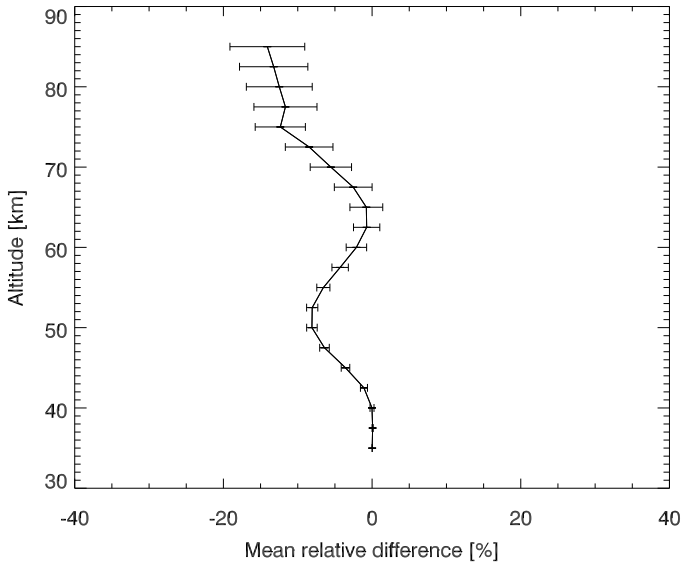

(a)

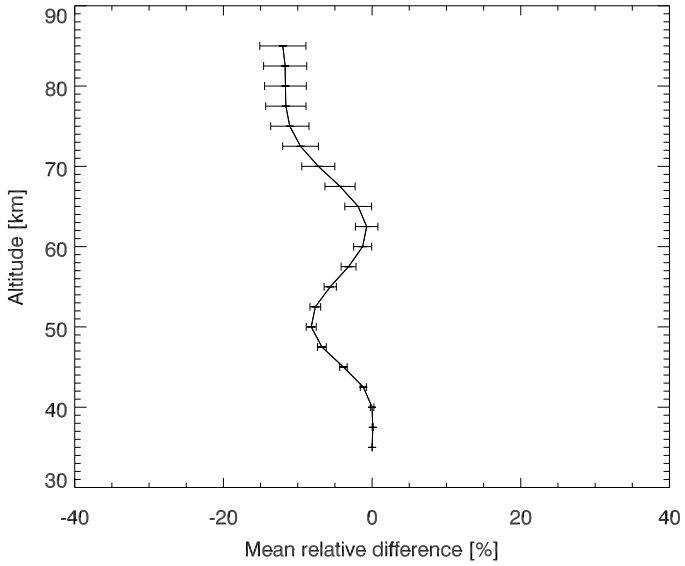

(b)

Figure 5.1: Relative difference between the profiles measured by cWASPAM3 and EOS-MLS profiles above Zugspitze. Both figures are retrieved according to v1 parameters, but Figure 5.1(a) is retrieved with a 12 hour integration time and and Figure 5.1(b) 4 hours ($v1_{short}$).

across-track and approximately 400 km along the line of sight. Profiles retrieved by EOS-MLS differs from ACE-FTS[5] by ±5% and 2 – 10% compared to HALOE[6]. A detailed validation of the profiles can be found in Lambert et al. (2007). The time needed by EOS-MLS to retrieve a profile can be assumed to be instantaneous compared to the long integration time needed by cWASPAM. Due to orbital restrictions EOS-MLS do not provide a profile at the exact same location (the variance in longitude being much larger than in latitude) on every orbit, so to get a decent number of co-located retrievals I picked out EOS-MLS profiles with ±1° latitude and ±5° longitude. cWASPAM3 points to the south with an elevation angle of 15° thus the atmosphere measured is approximately a region between 180 – 320 km south of Zugspitze. The collocation parameters were therefore centered at 45° N, ≈250 km to the south.

5.1.2.2 Comparison of profiles

To correctly compare profiles from EOS-MLS and cWASPAM the difference in vertical resolution and altitude sensitivity needs to be taken into account. This is best done by convolving the profiles from EOS-MLS to the averaging kernels from cWASPAM for each overpass. It also has the effect that at the altitudes where cWASPAM is not sensitive and get most information from the a priori so will the profiles from EOS-MLS. The new profiles are calculated according to

$$\hat{\boldsymbol{x}} = (1 - \boldsymbol{A})\boldsymbol{x}_0 + \boldsymbol{A}\boldsymbol{x}. \tag{5.1}$$

The equation is the same as Equation C.16a although the error, $\boldsymbol{D\epsilon}$, of the EOS-MLS profile is unknown here and contained in the $\boldsymbol{x}$ term. The a priori, $\boldsymbol{x_0}$, used for EOS-MLS is the same as the one used in the cWASPAM retrievals.

Table 5.2: A short description of the different datatypes.

Parameter/Data version	v1	v1_{short}	v2
Pressure broadening parameters	Liebe89	Liebe89	Liebe89
Spectroscopic catalog	JPL91	JPL91	JPL91
Atmospheric background	NCEP-CIRA86	NCEP-CIRA86	EOS-MLS
A priori profile	Standard	Standard	USSA76
Integration time [h]	12	4	12

Different data versions One of the points of the Zugspitze campaign was to compare how well current, state-of-the art, water vapor radiometers compare to measurements taken by satellite. In order to minimize the bias introduced from non-instrumental sources the retrievals where made with a background atmosphere constructed from EOS-MLS data[7]. Two different data versions from cWASPAM were compared to the EOS-MLS

[5] Atmospheric Chemistry Experiment - Fourier Transform Spectrometer onboard SCISAT-1

[6] Halogen Occultation Experiment onboard UARS

[7] EOS-MLS provides among other things temperature, and geopotential height at predefined pressure levels.

profiles; the default retrievals and retrievals which used an EOS-MLS constructed background. In addition a third version, using the default background but only 4 hours integration time, was included in the comparison in order to investigate the sensitivity of the instrument. The differences can be found in Table 5.2. `Liebe89` refers to the empirical constants taken from Liebe (1989) and `JPL91` to the JPL-catalog described in Pickett et al. (1998). In all cases are the data-timestamps centered around the timestamp of the EOS-MLS profile. Two of the versions use an integration time of 12 hours whereas the last is only integrated for 4 hours. Results from the comparison can be seen in Figures 5.1, 5.2 and 5.3.

5.1.2.3 Results

In Figures 5.1 and 5.2 the mean relative difference between cWASPAM measurements and EOS-MLS can be seen. The difference was calculated relative to the EOS-MLS measurements according to,

$$\boldsymbol{d} = \frac{\boldsymbol{x}_{cWASPAM} - \boldsymbol{x}_{EOS-MLS}}{\boldsymbol{x}_{EOS-MLS}}. \tag{5.2}$$

The error region in the plot is the standard deviation of $\boldsymbol{d}$ for the set at each layer. As can be expected when the EOS-MLS profiles are convolved with the averaging kernels from cWASPAM there is be no difference at low altitude. The kernels are zero at these altitudes and all information is taken from the a priori. At the uppermost altitudes cWASPAM is less sensitive, but the averaging kernels are >0, which implies that some information is taken from the measurement, and not only from the a priori. Thus, the convolved EOS-MLS profile will still contain information from EOS-MLS. Although the averaging kernels from cWASPAM are used on EOS-MLS the measurement from cWASPAM will be burdened with a larger smoothing error as the vertical resolution of EOS-MLS is more than a factor of two better than the ones from cWASPAM at these altitudes. The larger spread at these altitudes is therefore to be expected.

EOS-MLS overestimate the amount of water vapor compared to cWASPAM in two distinct layers. One relatively low, between 45 and 55 km, and the other extends from 65 km and upward. In the case of the v2 data, where the atmospheric parameters (temperature and pressure) are taken from EOS-MLS, the difference is less at the higher altitudes. It is interesting to see that the v1 data underestimate the amount of water vapor compared to EOS-MLS over the whole profile, although in the middle of the retrieved profile the measurement is almost identical. For the v2 data on the other hand there is a "kickback" effect in the middle of the profile where cWASPAM overestimate the amount of water vapor. This kickback, or overshoot, is most probably caused by the a priori profile. In the lower regions the retrieved profile will follow the a priori as there is not enough data. When the measured data start to become reliable (approximately above 45 km) the algorithm will compensate for the too low values as discussed in Section 4.2.5.3. Thus, there will also be larger errors in the upper part of the profile caused by the algorithm decreasing higher altitude water vapor as a consequence of the overshoot. A similar oscillation effect of the profile can be seen in Figure 5.4. While Figures 5.1 and 5.2 show the mean difference between EOS-MLS profiles and cWASPAM profiles, Figure 5.3 show the difference at each single co-located measurement at four distinct layers; 50, 60, 70 and

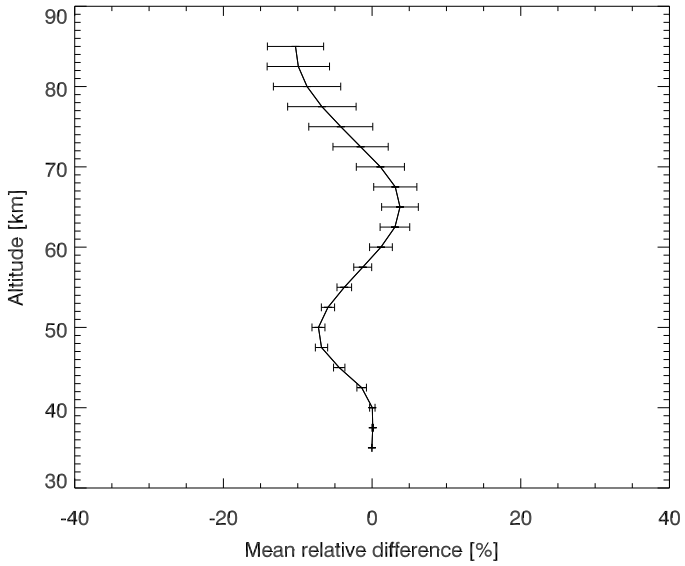

Figure 5.2: Same as Figure 5.1, but for data version 2.

80 km. On February 20 there is a large discrepancy between cWASPAM and EOS-MLS. This discrepancy is also visible in the v2 data (not shown). However none of the logged house-keeping data indicate any changes that could affect the instrumental reliability. Nor do the baseline removal fit indicate a change in the removed baseline. The sky brightness temperature of the day was less than 100 K so the observing conditions were normal. As the discrepancy is visible in both data versions a problem caused by the atmospheric background can be excluded. A possible explanation could be that a short term decrease in the water vapor occurred at the time of the EOS-MLS overpass. A sharp, short term, dip in the volume mixing ratio would be smoothed out by a 12 hour integration time, but visible in retrievals with a short integration time. This theory is confirmed by the much lower difference between the data integrated for only 4 hours and EOS-MLS, where the error is only approximately 50%. The general difference seems to be slightly smaller between the EOS-MLS profile and cWASPAM at the upper part of the atmosphere. This could imply that the water vapor amounts at these altitudes are relatively variable. The increase in signal strength gained by the longer integration time is does not improve the results as the water vapor distribution varies at a shorter time-scale. For the mid to lower part of the retrieval, where the signal is already good for the 4 hour integration time no appreciable improvement can be seen in for 12 hour integration time compared to the 4 hour integration.

5.1.2.4 Concluding remarks

In order to validate retrieved profiles an intercomparison campaign was initialized at Zugspitze. The intercomparison was mainly intended to compare and correlate three ground-based water vapor radiometers and this work is still underway. However one of the points of the intercomparison was to compare the retrieved profiles to co-located profiles taken by EOS-MLS. In the intercomparison between the cWASPAM instrument

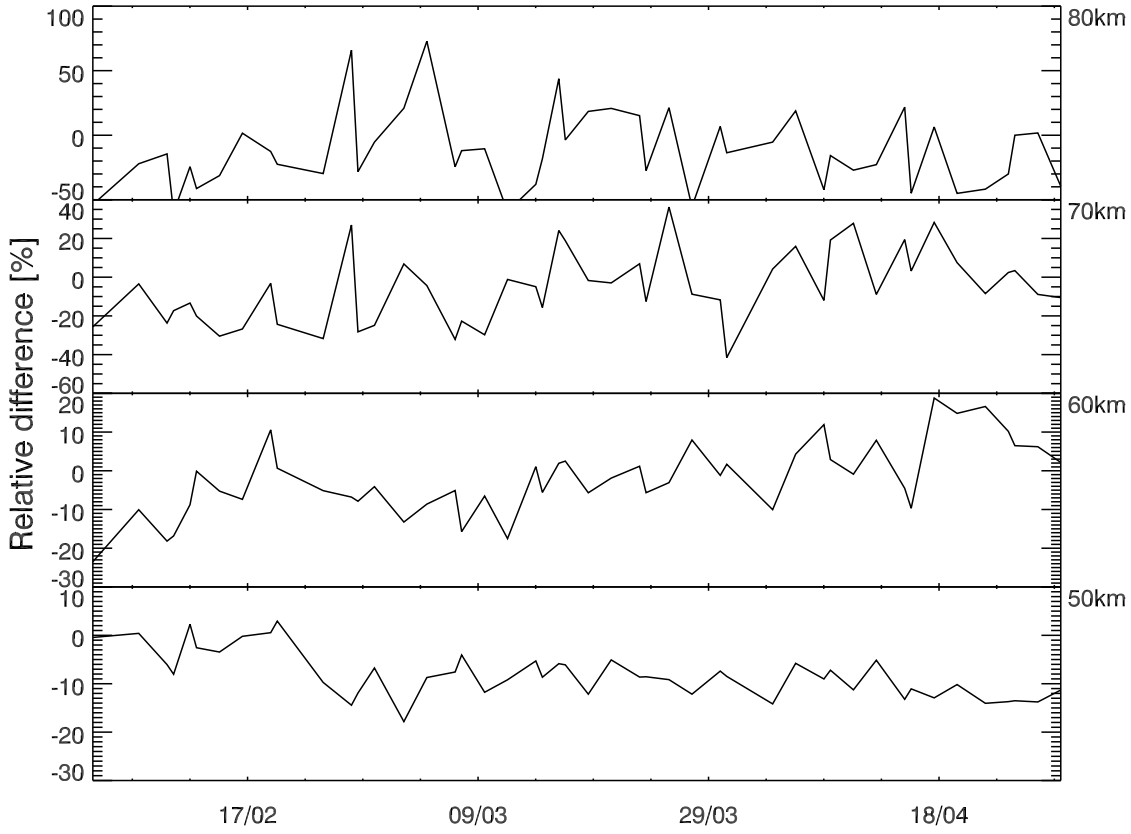

Figure 5.3: The difference between EOS-MLS profiles and profiles measured by cWASPAM3 (v1 data with 12 hour integration time) at 4 separate layers.

and EOS-MLS it can be seen that the latter in general overestimates the water vapor compared to the former. The background atmosphere is also shown to have some impact of the retrieved profile at higher altitudes. Although not explicitly apparent it seems that the climatological water vapor profile provided by the U.S. Standard Atmosphere from 1976 is a bit low in the stratosphere which cause a positive overshoot in the relative difference to the EOS-MLS profile (Fig.5.2). A similar overshoot is not visible in the standard a priori profile. That is however not an indication that the default a priori is correct. It could instead overestimate the water vapor, which would result in a larger negative difference at higher altitudes. Such a negative difference is present in both data versions and it is hard to deduce its origin.

Another interesting outcome of this comparison is the fact that the geophysical variability at higher altitudes seem to be relatively high. When using a longer integration time the smoothing error became larger than the increase in sensitivity at high altitude and the result was a retrieved profile with larger relative difference compared to EOS-MLS profiles. The effect shows up as three distinct events during the intercomparison time and can be explained by a short term depletion or an airmass with significantly lower water vapor

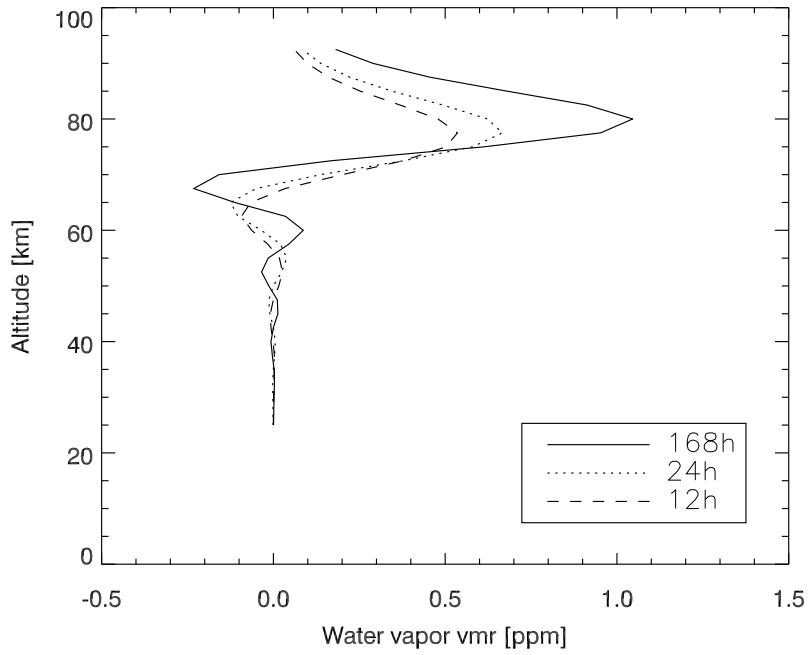

Figure 5.4: The figure shows the impact on the retrieved profile of a 2.5 km thick layer with 6 ppmv water vapor located at 82.5±1.25 km. The averaging kernels used for the calculation are based on a system temperature of 20 K, a tropospheric transmission of 90%. The solid line represents a 168 h (one week) integration, the dotted line a 24 h integration and the dashed a 12 h integration.

passing over Zugspitze at the same time as the EOS-MLS overpass.

5.2 Observations of the NLC-region with cWASPAM

NLCs are one of many puzzling polar mesosphere specific phenomena and the question arise if the improved instrument can observe them. The clouds themselves cannot be observed directly as they consist of ice crystals and the instrument is only sensitive to water vapor. This section will investigate if it is possible to detect them indirectly. Model runs in von Zahn and Berger (2003) suggest evidence of a dehydrated mesopause due to the creation of "summer upper mesospheric ice clouds" (SUMIC) and a lower region with enhanced water vapor as those clouds descend and sublimate. Whereas the dehydration is fast (the initial time-scale is <6 h and bottoms out after $\frac{3}{4}$ days) the time-scale for deposition is on the order of days. The water vapor is deposited in the lower regions of the SUMIC (82 – 84 km for 65° – 70°N) and can reach enhanced mixing ratios of up to 8 ppmv (tidal maximum after 2.8 days). At these altitudes the instrument sensitivity is very low and the integration time needed to reliably observe an water vapor deposition by NLC is on the order of days, similar to the process itself. The averaging kernels can be used to visualize the (vertical) sensitivity of the instrument. For example, as can be seen in Figure C.1, a 24 h integration will project all water vapor above 77.5 km to the 77.5 km

layer. In the case of the tidal observations (see Figure 6.1) which are retrieved with an approximately 7 times longer integration time the uppermost limit is 80 km. The x-axis value of each layer in the averaging kernel represent the influence of the measured profile to the retrieved profile. For example, a 2.5 km layer with 1 ppmv of water vapor at 80 km would be smoothed over a larger region with a peak of ≈0.2 ppmv at 80 km in the case of an observation with the averaging kernels in Figure 6.1. It is important to note that the vertical resolution of the output profile is limited by the thickness of the layers in the atmospheric model (2.5 km). Rodgers (1976) comment on the fact that disregarding from computational limits the layer thickness of the background cannot be infinitely small. With model layer thickness much smaller than the vertical resolution of the instrument the retrieved profile will start oscillate as a consequence of the algorithm trying to account for noise in the spectra which cannot be accounted for by the observation.

5.2.1 Result and discussion

Due to the layer approach in the forward model a thin layer (<2.5 km) with a high VMR will be smoothed out to cover the whole model-layer thickness. For example, a 500 m thick layer with 10 ppmv would result in a 2.5 km thick layer with 2 ppmv. The case tried here contains a much more water rich layer – 8 ppmv over 2 km, which results in a 6 ppmv layer, 2.5 km thick. To simulate how an injection of this amount of water vapor affect the measurements a vector with the added water vapor is convolved with the averaging kernels for three different integration times. Figure 5.4 shows the results on the background level of water vapor. The system temperature used to calculate the averaging kernels is 20 K and the transmission is 90%. Further parameters for the simulation the default elevation angle (18deg) and the background atmosphere from 30th of August 2008. In the figure it can be seen how such a water rich layer would affect the retrieved profile if injected at 82.5 km[8]. The solid line is the addition to the normal profile if the integration time was set to 168 h (one week), whereas the dotted line shows the result of one day of integration and the dashed line represents an integration time of 12 h. In the latter case approximately 0.5 ppmv of extra water vapor would be seen at 80 km after such an injection event. If, on the other hand, the layer of increased water vapor instead is located at 85 km the added water after 12 h would only be 0.35 ppmv at 80 km (not shown) which would be harder to detect. However, according to von Zahn and Berger (2003) the most probably injection altitude would be around 82 – 83 km. This indicates that it could be possible to detect large depositions of water vapor by sublimating NLCs. However due to the long time-scales involved it would be preferable to correlate such a detection to a well-defined event in order to fully understand the limitations of the instrument before it is used as a tracer of NLCs.

Furthermore, some qualitative constrains can be presented on the available water vapor at high altitude. During the summer months the retrieved profiles are consistently higher than the a priori above 75 km. In general the retrieved profile is underestimated (the low sensitivity of the instrument will force the profile towards the a priori, see discussion in Section 4.2.5.1). Thus the actual amount of water vapor is probably relatively high, above 3 ppmv at 80 km. It should also be noted that it is not possible to deduce

[8]The altitude of the layer is the middle of the layers, thus it is spread around 82.5±1.25 km.

if this is a water vapor layer at 80 km, or a layer with much more water vapor at higher altitudes.

5.2.2 Concluding remarks

Direct detection of NLCs is not possible due to the fact that the water content in NLCs is ice crystals, not vapor. However, simulations shows that it could be possible to detect depositions of water vapor as modeled by von Zahn and Berger (2003). Although it would be preferable to initially correlate such detections with other observations in order understand how they are related to the normal geophysical variation of water vapor at these altitudes. It should be noted that only the total amount of water vapor above 80 km can be deduced, no information about the vertical distribution will be available.

Simulations of an instrument with 10 K system temperature were also carried out which resulted in the same conclusion. With a lower system temperature the upper limit will be reached faster and it is therefore possible to constrain the variability on a shorter time-scale. However, the system will not be able to resolve any vertical distribution at higher altitudes. Above 80 km ground-based microwave spectroscopy not well-suited for measurements of the vertical distribution of water vapor. The very weak water line is one reason and the fact that the Doppler to pressure broadening transition starts already at approximately 77 km additionally limits the sensitivity of cWASPAM. The events cannot be properly resolved vertically and only a qualitative description of the atmosphere at this altitude can be given.

5.3 Time series of distribution of water vapor

5.3.1 Observation locations

The developed instrument is very delicate and is not intended to be used in different campaigns where it needs to be moved around. Once installed at a location it is not expected to be moved. In addition to being large and heavy it also demands a lot of power and relatively stable room temperatures. A stable Internet connection is needed in order to control the instrument and download the data. Thus the scientific and logistical infrastructure at the observation location is of some importance. Furthermore as shown in Figure 4.6 a location with high tropospheric transmission is favorable, for example a high altitude location with relatively dry atmosphere.

Arctic LIDAR Observatory for Middle Atmosphere Research (ALOMAR) ALOMAR is located north of the polar circle, 69.16°N, 16.00°E just outside the village Andenes by the north Atlantic. The observatory sits on top of the mountain Ramnan at an altitude of 380 m a.s.l. It has been in operation as a research facility since 1994 and houses several different active and passive instruments for atmospheric research. Being located within the polar vortex makes it interesting from a middle atmospheric point of view.

Umwelt Forschungstation Schneefernerhaus (UFS) On the highest mountain in Germany, Zugspitze (47.25°N, 10.59°E), did the State of Bavaria establish an environmental

1998. Located just below the peak of the mountain at an altitude of 2650 m.a.s.l., it is operated by a consortium consisting of several German Universities and Federal Agencies with the aim to provide a location and needed infrastructure for environmental research. Since September 2009 Max-Planck-Gesellschaft is a part of the consortium.

5.3.2 ALOMAR, 1995 – 2009

Since 1995 the vertical water vapor distribution above ALOMAR have been observed with WASPAM instruments from MPS. The full dataset contains data from different frontas well as backends. An overview of their differences and similarities can be seen in Table 5.3. The designation of the backends should be read as:

W-HR	High (spectral) resolution WASPAM
W-MB	Medium bandwidth WASPAM
W-VHR	Very high (spectral) resolution WASPAM

Unfortunately there was a gap in the observations between data version 3.3 and 3.4 when the old instrument/backend broke down before the new one was installed and no direct comparison between the instruments could be done. However the individual instruments have been involved in different comparison campaigns and indicate reliably retrieved profiles.

The first instrument was installed at ALOMAR late 1995 and the frontend of this instrument was successfully running until 2006. A complete description of the instrument and associated updates can be found in Jarchow (1998) and Seele (1999). The new instrument, described herein, was installed in May 2008. All spectrometer backends mentioned in the full dataset are CTS. Apart from a 180 MHz CTS they all had a bandwidth of 40 MHz, but with different spectral resolution. In order to facilitate the comparison the bandwidth of the wide-band CTS was cut to 40 MHz, that is only the middle 40 MHz were used in the retrieval. It also has the advantage that, according to the harmonic baseline removal discussion in Section 4.1.5.2, the same baseline parameters could be used for all backends. Thus artifacts introduced by the baseline should be minimized between the backends. As can be seen in Table 5.3 the two last backends are almost identical and there are only a few slight differences in the internal setup. The system temperature of the old instrument increased with time and in order to minimize the impact of this degradation in sensitivity the integration time used is, in all cases, 168 hours (1 week). This integration time is long enough to ensure a good enough SNR to reach the virtual maximum sensitivity of the instrument (see discussion in Section 4.2.4).

The background atmosphere is constructed according to the same rules for all years, which in essence means that only the lower atmosphere is changing between each year, the upper part is identical.

5.3.2.1 Long term evolution of water vapor above ALOMAR

The long term evolution of water vapor in the middle atmosphere has received a lot of focus during the last few years. For a complete assessment of the changing climate it is important to know, and understand, the natural variability of water vapor. Thus, good and reliable observations of how the available amounts of water vapor in the middle atmosphere vary is necessary. Numerous instruments, both ground-based and space-borne,

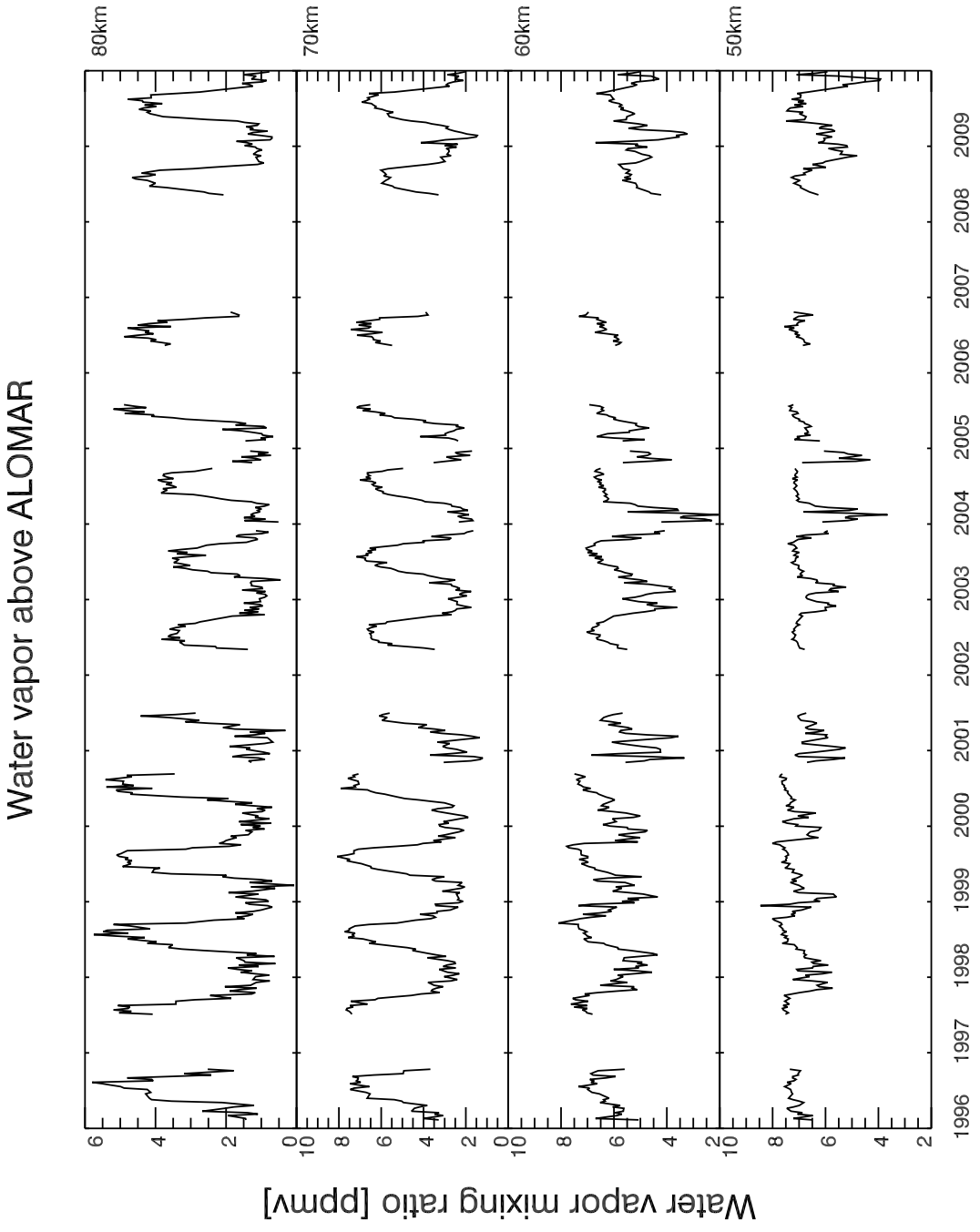

Figure 5.5: The full dataset from ALOMAR, starting early 1996 until the end of 2009. Each datapoint is retrieved with an integration time of 168 hours (1 week) to assure that the old instrument correctly retrieve the upper part as well. Datagaps shorter than 4 weeks have been interpolated whereas longer gaps are left out.

Table 5.3: The different sub-datasets used for the complete dataset of ALOMAR data. The spectral resolution given is the effective spectral resolution.

Data version	v3.1	v3.2	v3.3	v3.4
Frontend	WASPAM	WASPAM	WASPAM	cWASPAM
Backend	W-HR	W-MB	W-VHR	W-VHR
Bandwidth [MHz]	40	180	40	40
No. of channels	2048	4096	4096	4096
Spectral resolution [kHz]	20	44	10	10
In operation	1995 - 2002	2002 - 2005	2004 - 2006	2008 - ...

focus on water vapor and continuously add information to the ever growing dataset. It is therefore troubling that no conclusive results of the long term evolution of water vapor exist. Laštovička (2009) cite the long term behavior of water vapor as one of three problematic areas when it comes to the understanding of the middle atmosphere. Garcia et al. (2007) also investigate this problem and give some ideas of the reasons. They model the behavior of water vapor since 1950 with WACCM[9] and the obtained results do not agree with neither HALOE data nor the Hygrometer dataset from Boulder. However, ozone and temperature trends which are also measured and modeled agree well. Their explanations for the discrepancies is based on the long dataset used by WACCM compared to the much shorter observations. The hygrometer dataset goes back to 1980 whereas the HALOE dataset only dates back to the mid-nineties. Low frequency cyclic variations could be interpreted as trends by shorter datasets.

Hartogh et al. (2010) give a detailed discussion of how the amount of water vapor has changed above ALOMAR between 1996 and 2006. The main scope of the paper discuss water vapor measurements in correlation to variations in the solar Lyman-α radiation. In addition a large part is spent on the comparison to results obtained from the LIMA model (Berger 2008). Hence, a thorough trend analysis will not be undertaken here. Instead a short recollection of earlier results will follow and how the data from cWASPAM fit into those conclusions. The dataset in Hartogh et al. (2010) is essentially the same as presented here, with cWASPAM data excluded. However, one important difference exists between the datasets. The one presented in Hartogh et al. (2010) is obtained by a 24 hour integration time, and thereafter smoothed with a seven day running mean. The data presented here, see for example Figure 5.5, is obtained with 168 hour integration time. By using a longer integration time the sensitivity of the older instrument is much better at high altitudes, which leads to higher amounts of water vapor in the retrieved profile. The noisier signal underestimate the amount of water vapor at high altitude due to the conservative a priori profile. Furthermore the baseline reduction scheme used with the older instrument was to try to find the exact frequency of each component. This approach was replaced by the harmonic approach described in Section 4.1.5.2 since using the same baseline reduction scheme on all instrument greatly reduce any bias introduced by changing the estimated baseline components.

As Figure 5.5 show, and as being discussed in Hartogh et al. (2010), the amount of water vapor above ALOMAR during the last 14 years has not been stable and a clear

[9]Whole Atmosphere Community Climate Model

trend[10] is difficult to deduce. However, there seem to be a slight decrease in water vapor when the full dataset is used. Furthermore, Hartogh et al. (2010) note differences in the long term behavior between summer and winter season. A, global, major decrease in the water vapor was detected between 2001 – 2002, which was also detected by other groups observing water vapor at lower latitudes, see for example Rosenlof and Reid (2008). An explanation to this sudden decrease in water vapor was given by Randel et al. (2006) and relates to a change in the Brewer-Dobson circulation. In the years after this depletion the amount of water vapor has slowly increased again and during 2005 – 2006 it almost reached the same levels at high altitudes as before the depletion. Although this slight rebounce almost restore the amount of water vapor to the initial level there is a small negative trend. It is strongest at 60 km altitude with an approximate decrease of 0.05 ppmv/year. A negative trend is puzzling as the general amounts of methane has increased during the last decades, with a short plateau for a few years (Dlugokencky et al. 2003, Rigby et al. 2008). Although the current increase of methane doesn't seem to have reached the polar latitudes yet (Dlugokencky et al. 2009). No explanation to this behavior has so far been put forward.

The trend towards less water vapor is also visible in LIMA calculations. LIMA, in the setup used for Hartogh et al. (2010), starts every model run with identical amounts of water vapor at the lower boundary and only modulates water vapor at these altitudes by means of photo-dissociation by Lyman-α and transport. The Lyman-α values are taken from Woods et al. (2000). The dataset covers almost a full solar cycle and the influence of the Lyman-α is found to be dependent of season. During summer there is a constant replenishment of water vapor from below thus high solar activity and increased Lyman-α and the consequent enhanced photo-dissociation is of less importance. On the other hand during winter there is a clear anti-correlation of water vapor to Lyman-α which can be seen in both datasets. However, as the dataset cover a full solar cycle and the corresponding cyclic influx of Lyman-α the negative trend in water vapor cannot be accounted to the Lyman-α, it has to be induced by transport.

A short note on sudden stratospheric warmings in the dataset Another interesting feature is the behavior of the sudden stratospheric warmings. Seele and Hartogh (2000) investigate the behavior of water vapor in the ALOMAR region of an observed stratospheric warming. This particular warming was a minor warming from the point of view of how it affected the polar vortex. However, it had a large effect on the stratospheric temperature, see for example von Zahn et al. (1998). It can be seen as a sudden increase in water vapor in February 1998. The warming increases stratospheric temperatures by approximately 20 K as resolved by the background used for the retrieval. The warming during spring 2009 on the other hand is a major warming with a complete and irreversible break of the polar vortex. When comparing the two events a few properties that differs between them can be noted. From a temperature point of view a difference in the background atmosphere as resolved by the NCEP data can be seen. The 1998 warming is characterized by a strong warming in the stratopause region (20 K increase at $\approx$50 km) with only a minor effect on lower altitudes whereas the 2009 warming is more pillar-like

[10]Trend is here used to denote a linear regression of the averaged amount of water vapor, not a climatological trend.

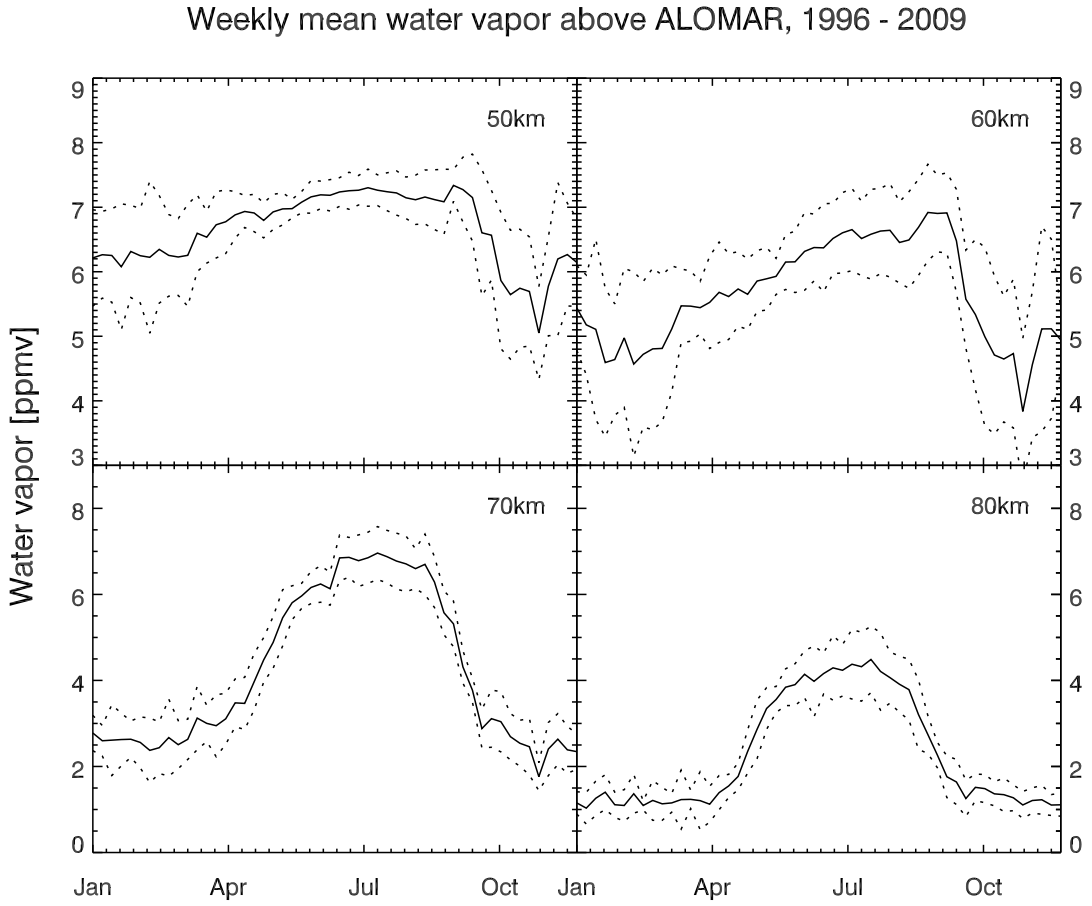

Figure 5.6: Weekly mean water vapor values above ALOMAR between 1996 and 2009. The dataset is rebinned into weekly bins and the mean of each bin is plotted as a function of time. The solid line represent the mean whereas the dotted line represent the standard deviation in each bin.

in the sense that the warming increase temperatures all the way down to 30 km, but do only slightly warm the stratopause region (see Figure 2.5). Opposite to what is to be expected from this behavior the 2009 warming cause a strong increase in water vapor at the 60 and 70 km layer while the warming 1998 mainly seem to affect the 50 and 60 km layer. Thus the result cannot be caused by the changes in temperature and have to be explained by transport patterns. The major warming during spring 2009 breaks the polar vortex and moist air from the mid-latitudes enters the polar region to a greater extent than the 1998 event. This theory is strengthened by EOS-MLS which measures a significant decrease in mid-latitude water vapor during this time. It is believed the decrease is caused by water vapor-rich mid-latitude air being transported northward to the dryer polar airmass (Manney et al. 2009).

5.3.2.2 Weekly mean water vapor above ALOMAR

In order to better appreciate the mean yearly behavior of water vapor above ALOMAR the data presented in Figure 5.5 was rebinned to a weekly basis. This is however not based on the calendar weeks. Instead, the timestamp of each datapoint is translated into the day of the year which is divided by seven and the integer term is used as the number of the week. The mean of each bin was thereafter plotted and is shown in Figure 5.6 as the solid line, the dotted line represent the standard deviation of the corresponding bin. A few interesting features can now be seen. The variability of water vapor in the two lower altitude layers plotted here has a maximum during winter whereas the opposite is true for the higher altitudes. This is to be expected as the winter in the northern hemisphere is very unstable and characterized by a high degree of variability, see for example the discussion in Shepherd (2000). The variability is overall lower at the upper altitudes, but show a larger spread during summer. This is most probably caused by the negative trend and especially by the 2002 depletion incident. The time of increase and decrease of water vapor in the upper regions seems to be well defined as the spread here is very small. At 70 km the time of maximum gradient of the increase to summer[11] varies over the last 13 years by no more than 6 weeks, and the maximum decreasing gradient seem to be even more stable varying by approximately only a month. It can however not yet be concluded if there has been a slight shift in the onset time or if it is a random variation. A similar stable behavior can be seen for the 80 km layer. The very strong annual variation is much less evident in the 50 and 60 km layers from the point of view of quantity of available water vapor. Instead it can easier be defined as the stable period during the year. A skewed annual variability do however seem to be present in the 60 km layer where very slow increasing gradient last from approximately early April to early September where the water vapor amount abruptly start to decrease. Furthermore, a local minimum not visible in the mesosphere is present in the stratopause region around November. As mentioned above the starting time for the increase of water vapor is in early April for the 60 km layer and a few weeks later in the upper layers. The gradient is slightly steeper and the onset is more pronounced for the 80 km layer than the 70 km layer. While the annual behavior is almost symmetric at 80 km there is a slight asymmetry at 70 km with a much faster decrease than increase. This behavior is most pronounced at 60 km and at the lowest layer such a decrease is less evident, if present at all. The decrease at 80 km starts already in the end of July but not until approximately 2 weeks later can a falloff be seen in the 70 km layer. At 60 km the decrease in water vapor is not visible until September, however then with a very strong gradient.

A feature which was discussed in Hartogh et al. (2010) and not visible in Figure 5.6 is a secondary maximum during summer at 65 – 70 km. It can be deduced from Figure 5.5, but is much more clearly visible in Figure 5.8. The secondary maximum, or double peak, in the water vapor distribution is a feature visible in the profile as a second peak of water vapor above the main peak which is located around approximately 55 km. The secondary maximum can be traced back to a secondary, weaker, autocatalytic source of water vapor Sonnemann et al. (2005). There are also some indications of a correlation between the secondary maximum and the QBO (Sonnemann et al. 2009).

The full dataset making up Figure 5.6 can be found in a table format in Appendix D.

[11] If defined as the stable plateau of the annual variability.

This table contains all layers where the instrument is sensitive to the atmosphere and can be seen as a climatology of the weekly mean water vapor for the last 14 years above ALOMAR.

5.3.3 Water vapor above ALOMAR measured with cWASPAM

In order to better appreciate the yearly differences between ALOMAR and Zugspitze data is presented on a yearly basis. Thus the data retrieved so far with cWASPAM can be found in two separate figures; 5.7 for 2008 and 5.8 for data retrieved 2009. Although there is no data from Zugspitze dating back to 2008 and the data from ALOMAR only covers slightly more than half a year it is included here for comparative reasons. The annual variability of water vapor at ALOMAR, for 2008 as well as 2009, follow the general behavior of water vapor at polar latitudes, see for example the discussion in Lossow et al. (2009) and Seele and Hartogh (1999). It is characterized by a pronounced annual cycle with a strong maximum during summer and low values during winter. During winter the amount of water vapor is almost a factor of 3 lower as compared to summer at high altitudes (>70 km).

5.3.3.1 Water vapor above ALOMAR during 2008

The new instrument was initially installed at ALOMAR in the beginning of May 2008 and has been measuring ever since with the exception of shorter stops caused by hardware malfunction. As seen in Figure 5.7 the first year did not present any pronounced deviations from the normal behavior of water vapor as discussed in Section 5.3.2.2. The double peak is only barely visible during the 2008 summer, but the local minimum in November is well resolved by both the actual minimum and the correlated increase in the pillar shape in December.

5.3.3.2 Water vapor above ALOMAR during 2009

A few notes on the 2009 dataset should be mentioned and taken into account before analyzing the data from 2009 and comparing it to other datasets. On September the 13th an FM-transmitter was installed at ALOMAR, about 50 meters from the instrument. Initially it transmitted with a power of 250 W which severely disturbed the temperature measurements used for calibration in the retrieval. Unfortunately the installation was not revealed to us until almost one month later. Unrelated, but during this time the wobbler also broke down which introduced a strong baseline in the measured signal. When the cause for the disturbance of the temperature measurement was finally understood the output power of the transmitter was reduced to a level where it no longer affected the measurements. The transmitter is currently transmitting at minimal power (20 W) and is expected to be moved to a better (more shielded) location as soon as the weather permits. The disturbance caused by this low output power can be filtered out from the measurements and is not expected to introduce any further noise. In the case for the wobbler no such easy solution could be found and the instrument has been running without the baseline reducing wobbling since October 2009. This introduce a stronger residual baseline in the wings of the retrieved spectra. To reduce the impact of the wings an additional error is assumed at

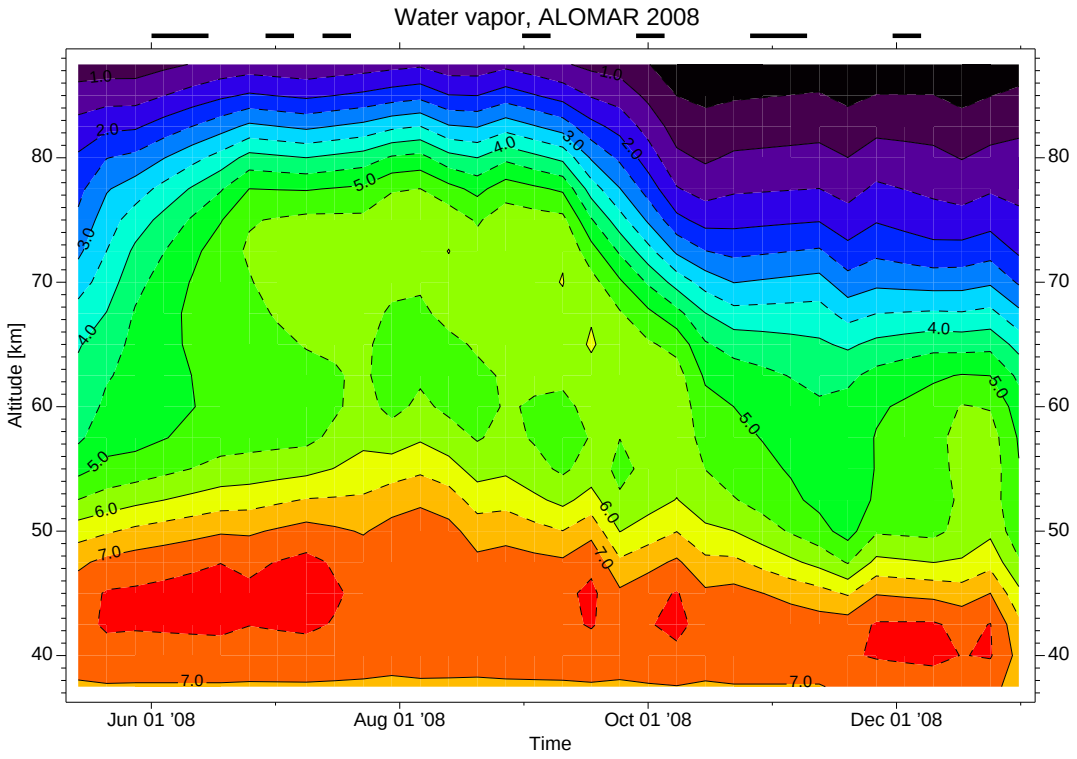

Figure 5.7: The variation of water vapor above ALOMAR for the observation time of the new instrument during 2008. The integration time for each point is 168 hours and shorter datagaps are linearly interpolated. The black bars above the plot denote times when the instrument was not running and the data interpolated.

the wings, hence the retrieval algorithm will force the profile to follow the a priori more closely to a higher altitude. Above 60 km there is no change at all to the retrieved profile but any variability below this level will most probably be underestimated as the a priori profile will be given a higher weight by the OEM.

2009 was an interesting year from the point of view of water vapor dynamics. As opposed to 2008 the double peak is clearly visible during late summer 2009, emerging in the second half of July and lasting until first half of September. It first appears around 70 km and slowly expands to lower altitudes and increases in magnitude in the maximum altitude. In addition to the two larger stratospheric warmings, visible in the beginning and in the end of the year the local minimum in November was unusually strong, with regions depleted in water vapor reaching down as far as 40 km.

5.3.4 Water vapor above Zugspitze during 2009

In connection to the initiation of the intercomparison campaign at Zugspitze one of the instruments was installed at Schneefernerhaus on Zugspitze. At the end of the campaign it was possible to keep the instrument at this location. Thus the instrument denoted cWASPAM3 has been observing the middle atmosphere from this location ever since. Water vapor measurements at a high altitude is favorable as there is less tropospheric

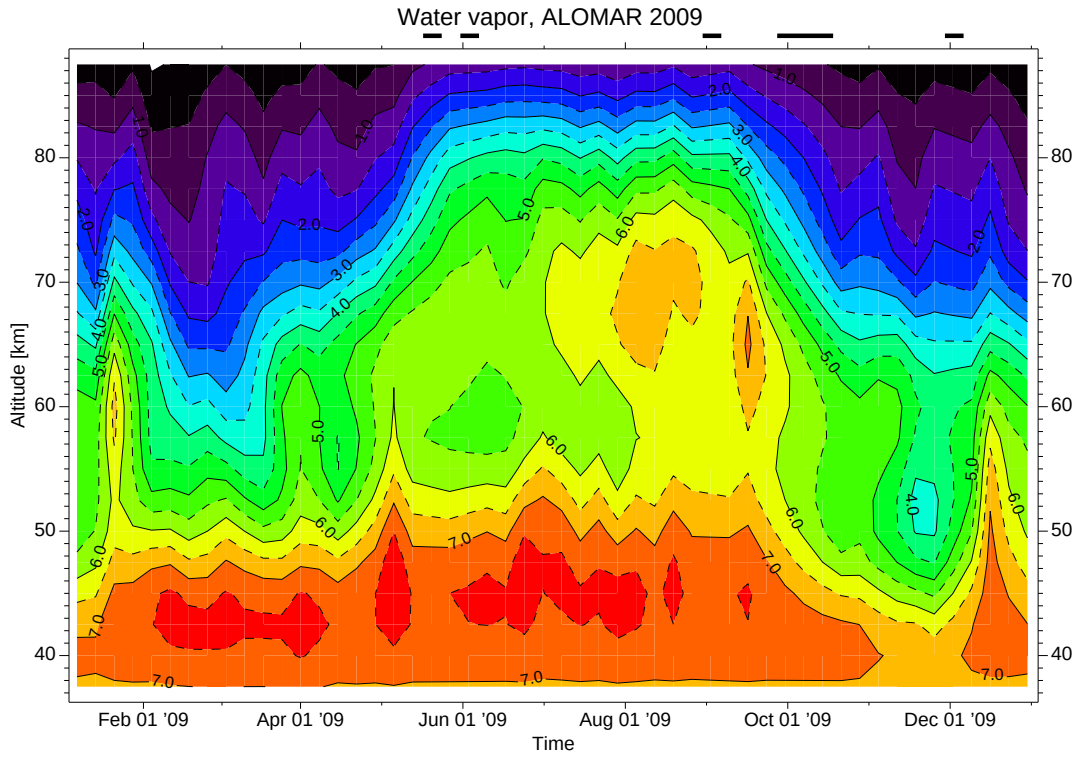

Figure 5.8: As Figure 5.7 but for 2009.

water vapor that attenuates the spectral line. The instrument at Schneefernerhaus is located at an altitude of 2650 m a.s.l. and has in general better observation conditions than ALOMAR, *i.e.* higher tropospheric transmission.

Unfortunately the axis connecting the chopper motor to the mirror broke in an unfortunate way in end of November 2009 and was not repaired until mid-January 2010. Thus there is no data from this time.

A plot of the yearly variation during 2009 (January and December are excluded) can be seen in Figure 5.9. If compared to Figure 5.8 (and Figure 5.7) a few initial remarks can be made. First it is important to note that Zugspitze is a mid-latitude location (47°N) whereas ALOMAR is a polar location (69°N) which has important implications on middle atmospheric transport and in consequence also the water vapor variability during the year. The amplitude of the annual oscillation is larger at high altitudes in the polar region (ALOMAR), than at mid-latitudes. The summer maximum is approximately as strong over both sites, but more important is the very low amount of water vapor in the polar middle atmosphere during winter compared to mid-latitude locations.

The decrease in stratospheric water vapor during summer might indicate a semi-annual variability above Zugspitze. There also seem to be a phase difference between the stratospheric and mesospheric variability. Lossow et al. (2008) discuss such a phenomena in measurements made by Odin. Although the dataset presented there is constrained by orbital parameters and do not extend further from the equator than 35°S and 35°N. However, the stratospheric water vapor maximum observed in February and November 2009 above Zugspitze need not uniquely be attributed to the SAO. During 2009 there

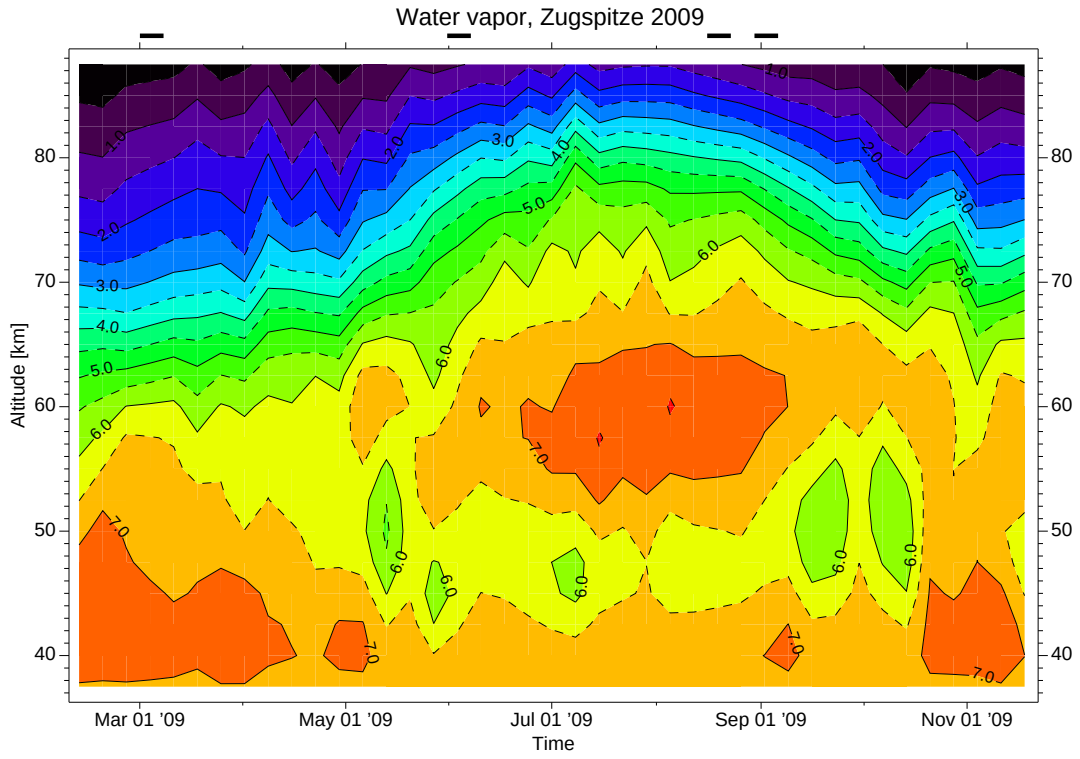

Figure 5.9: As Figure 5.7 but for Zugspitze 2009.

was a strong SSW in late January and another one during mid-November, which could affect the normal transport behavior and amplify the observed increases in stratospheric water vapor. As discussed in Section 5.3.2.1 it is known that ground-based microwave spectrometers regularly observe the impact of SSWs on the middle atmospheric in the water vapor VMR. Thus it cannot be excluded that the SSWs significantly amplified the observed increase in water vapor. Additionally, the lack of data during December and January add uncertainty and make it hard to deduce the yearly variation as it is unknown how the distribution develops during the winter. A longer data set is needed in order to conclusively answer the question.

5.3.5 ALOMAR and Kühlungsborn, January 2010

A fourth instrument has been installed in Kühlungsborn at the Leibniz-Institut für Atmosphärenphysik (IAP). It is therefore located in an interesting transition region between the mid-latitude behavior above Zugspitze and the polar latitude behavior of water vapor at ALOMAR. However, so far the dataset from this instrument is limited and below only a short discussion on similarities between ALOMAR and Kühlungsborn in January 2010 is presented.

The integration time used is 8 hours in order to properly resolve any time differences between the sites but also long enough to allow MISI[12] to retrieve data to a good enough

[12]Microwave Spectrometer at IAP (the designation of the instrument at IAP Kühlingsborn)

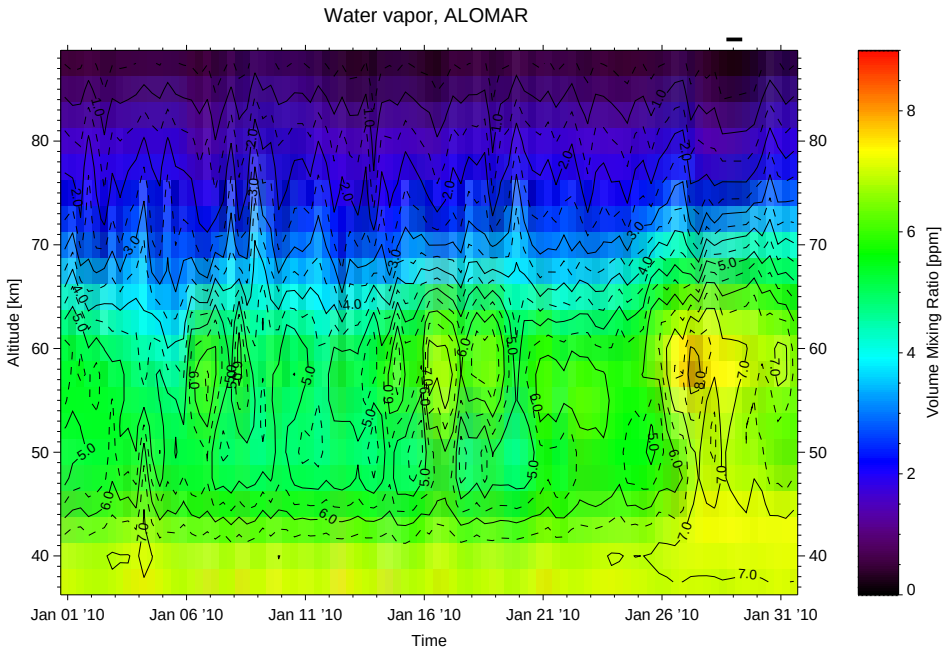

(a)

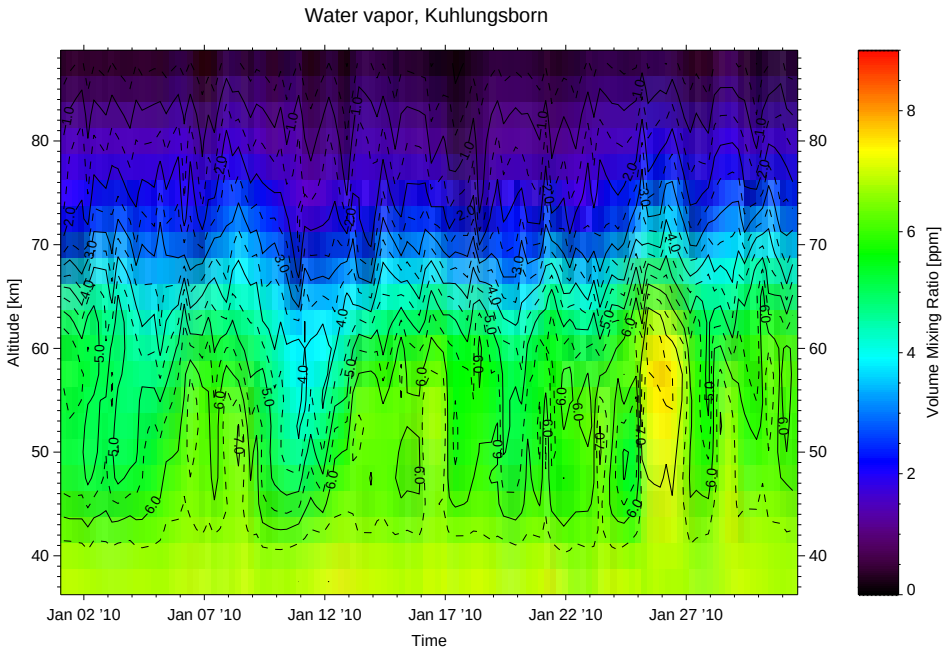

(b)

Figure 5.10: Water vapor above ALOMAR, 5.10(a), and Kühlungsborn, 5.10(b). It is retrieved with an integration time of 8 hours during January 2010. Note the coincident similarities (*e.g.* the event on the 16th) as well as the temporally offset events such the major warming in the end of the month.

quality. During January one of the backends for MISI did not work properly and the sensitivity was therefore decreased during this time. Furthermore MISI has been troubled by stray emission from a MW radar located in the vicinity of the instrument (*cf.* the influence of the FM transmitter cWASPAM1 discussed in Section 5.3.3.2). A comparison between the sites can be found in Figure 5.10. A confirmed warming event is visible in the end of the month and it can be seen that there is a time-lag between the two sites. The event is discussed in more detail in Section 5.4. There is another interesting event between the 16th and the 17th which seems to be coincident in time as opposed to the larger warming. This event has also been observed by the microwave group in Bern over Finland (C. Straub, *personal communication*) and a more detailed collaborative investigation of this event would be of interest.

5.4 Observation of a stratospheric warming from three different locations.

During the last few years there has been an increase in the numbers of SSWs (G. Hansen, *personal communication*). During the time of operation with the new instrument at least three sudden stratospheric warmings have been observed. Two during 2009, January and December, as seen in Figures 2.5 and 5.8, and one in January 2010. The stratospheric warming 1998, observed by the old instrument, was investigated in detail by (Seele and Hartogh 2000). That paper and Seele (1999) discuss the possibility to correctly retrieve the water vapor amounts during SSW due to the large temperatures fluctuations. By comparing a retrieval with the default background atmosphere to a retrieval that use temperatures retrieved with a LIDAR during the event they come to the conclusion that there is a risk of overestimation of the water vapor by up to 10% in the stratosphere by the difference in the used and true atmospheric temperature. This is consequence of the fact that the temperature changes are not fully resolved in the normal atmospheric background. Furthermore, as the water vapor in the stratosphere is overestimated, a "kick-back" effect of underestimation in the mesosphere occurs, see Section 4.2.5.3. However it should be noted that Seele (1999) does the comparison to a static CIRA86 background whereas the current retrieval use NCEP up to approximately 55 km. As can be seen in Figure 2.5 there is a clear increase in the temperature used for the background[13] and the error should therefore be smaller.

5.4.1 The stratospheric warming during January 2010

The stratospheric warming in January 2010 was observed from three different locations and will be discussed in the following section. A high time-resolution contour plot from each location can be seen in Figures 5.11, 5.12 and 5.13. In order to better resolve the dynamics the integration time is set to 4 hours for cWASPAM1 and cWASPAM3, and 8 hours for MISI which suffered from a dysfunctional backend at the time. By doubling the integration time the vertical resolution will be more comparable to the other instruments

[13]It should be noted that the LIDAR measurements show a difference of up to 80 K between CIRA86 and the true temperatures during the event, which is almost 40 K more than the difference between NCEP and CIRA for this event.

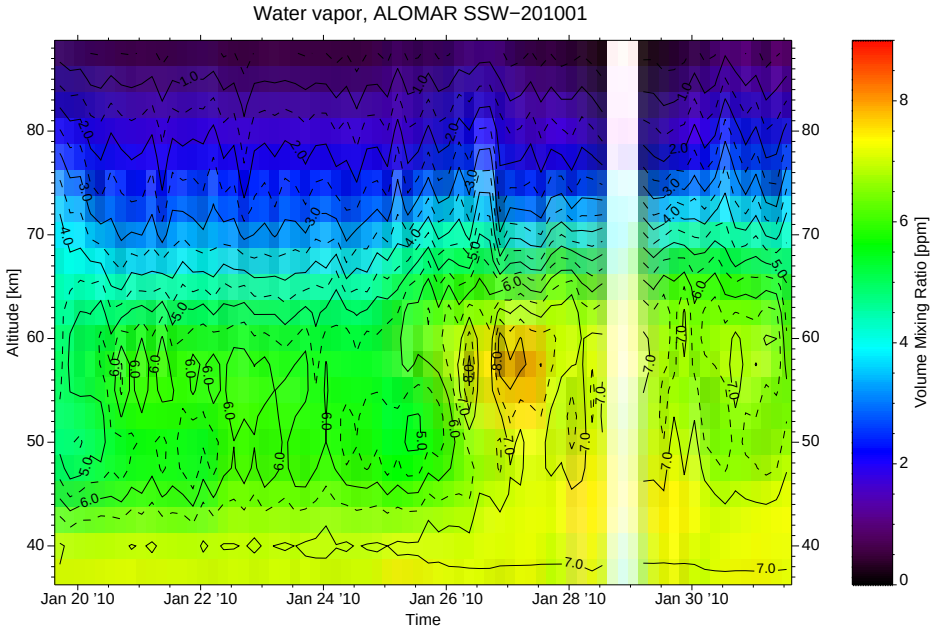

Figure 5.11: The stratospheric warming from January 2010 as measured above ALOMAR. In order to better retrieve the dynamics of the event the integration time used here is 4 hours.

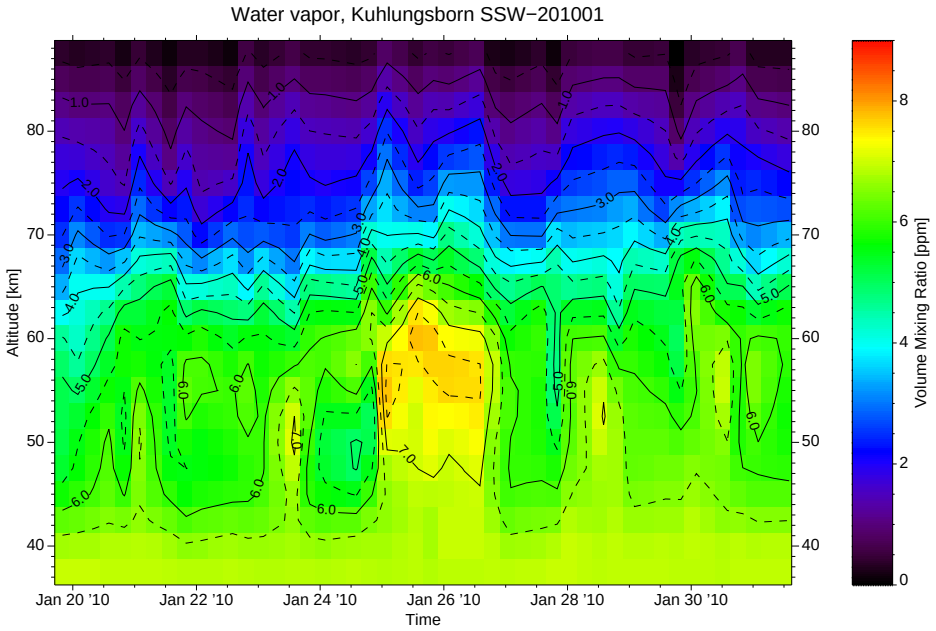

Figure 5.12: Same as Figure 5.11 but over Kühlungsborn with a integration time of 8 hours.

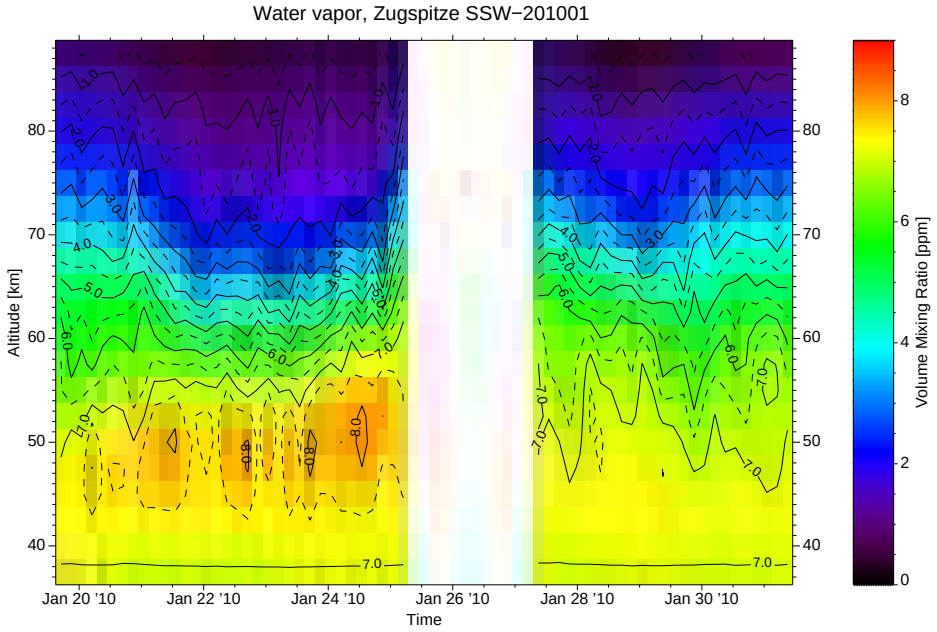

Figure 5.13: Same as Figure 5.11 but for Zugspitze. It can be seen that the normal water vapor level is higher than for the polar latitudes hence the warming is not as evident. A general increase of the mesospheric levels can however be seen after the 28th, which slowly decrease again in the end of the month.

(see the discussion in Section 4.1.2.1 on the influence of two backends). Following the discussion in Section 5.1.2 on short term variations in the higher atmosphere such a short integration time as 4 hours is possible to use without any risk of loosing sensitivity in the regions affected by the warming. The figures span the last third of January which better allows us to resolve the dynamics. The group in Bern claim to detect the warming as early as the 22nd of January with their instruments. cWASPAM3 do however not resolve any strong increase in water vapor during this time. It should be noted that cWASPAM3 has an elevation angle of 15 degrees and look to the south which imply that in reality it observes the atmosphere above the southern parts of the Alps whereas the instrument operated by the Bern group observe the atmosphere above Mulhouse, France (T. Flury *personal communication*). Furthermore, if instead of doing the 4 hour integration shown in Figure 5.13 a 24 hours integration is conducted a stronger increase in stratospheric water vapor can be seen on the 22nd. With the longer integration time a decrease in mesospheric water vapor can also be seen. A similar behavior in terms of a decrease in mesospheric temperature at the same time as a stratospheric warming is discussed in Siskind et al. (2005). Regardless if the behavior measured by cWASPAM3 is interpreted as indicative of a SSW or not the following can be deduced from the observed behavior. Above Zugspitze there is a slight increase in the water vapor at lower altitudes which maximizes already around the 23rd. This wetter airmass seems to slowly propagate into higher layers over the course of time, but is almost gone on the 25th. It does not propagate as a continuous water vapor rich layer. If instead the general contour lines are followed, it can be seen that they start to propagate upwards on the 23rd. Furthermore the water rich airmass between 45 – 55 km

stabilize during this time and is less variable. Unfortunately there was a power failure at noon at Schneefernerhaus on the 25th and the instrument was not restarted until afternoon the 27th. It is therefore hard to reliably correlate this increase and transport of water vapor to the warming seen above Kühlungsborn and ALOMAR.

MISI on the other hand detects a strong and clearly visible increase of water vapor over a large altitude range on the 25th of January. Approximately one day later the warming is visible above ALOMAR, on the 26th. But already on the afternoon of the 25th a slight increase in water vapor at approximately 60 km can be seen. This wetter airmass seem to expand and propagate downwards as well as increase in moisture over the course of time. Two distinct maxima can be seen in the observed water vapor, one less pronounced on the morning of the 26th and a second stronger in the afternoon on the 27th. A water vapor depletions following event seem to be coincident in time on the 28th on all locations.

There are ongoing discussions with the microwave group at the University of Bern concerning a collaborative investigation of the above described event. This would imply water vapor data from a multitude of water vapor radiometers spread around Northern Europe. In addition to their radiometer in Bern they were also at the time involved in a campaign in Northern Finland which would extend the dataset and give important information on the longitudinal distribution of the event.

6 Tides in the middle atmospheric water vapor

The dynamics of the polar middle atmosphere is important for the global circulation and in order to correctly model it a comprehensive knowledge of the involved processes is needed. Tides are known to affect gravity waves which are an important driver for the dynamics in the middle atmosphere (Fritts and Vincent 1987, Wang and Fritts 1991). It is therefore of interest to understand all aspects of the tidal behavior in the MLT[1] region. Detections of tidal behavior in the different wind fields in the polar regions are common and a monthly mean climatology have been published (Portnyagin et al. 2004). The instrument described herein has an upper sensitivity limit at approximately 80 km, radars on the other hand sounds the mesopause region and above. Observations by microwave radiometers can therefore be a good complement to the radar observations as they are sensitive to a lower region in the middle atmosphere. In contrast to the well-known tidal behavior in the winds, almost no information of the behavior of tracers such as water vapor exist. Largely due to the observational difficulties connected with ground-based microwave spectroscopy. Measurements from satellites have the possibility to temporally resolve water vapor better than ground-based microwave instruments, but they suffer from orbital constrains and are rarely able to achieve the needed local time coverage for conclusive tidal detection. The high sensitivity of the new instrument makes it possible to retrieve tidal variations in the mesospheric water vapor for the first time.

6.1 Observation of tides

6.1.1 Method

The importance of the a priori profile has been discussed in Section 4.2.1.3 and 4.2.5.1. Thus with the knowledge of the annually varying water vapor one would perhaps expect that a changing a priori profile should be used for sensitive measurements. However, the nature of OEM is that the influence of the a priori profile depends on the noise of each measurement – a noisier measurement result in more information taken from the a priori profile than from the measurement and vice-versa. A dynamic, or varying, a priori profile could introduce seasonal artifacts in the dataset. This observation focus on the variability of the water vapor and less on the absolute quantities thus it was decided to use a constant a priori profile.

[1] Mesosphere and Lower Thermosphere

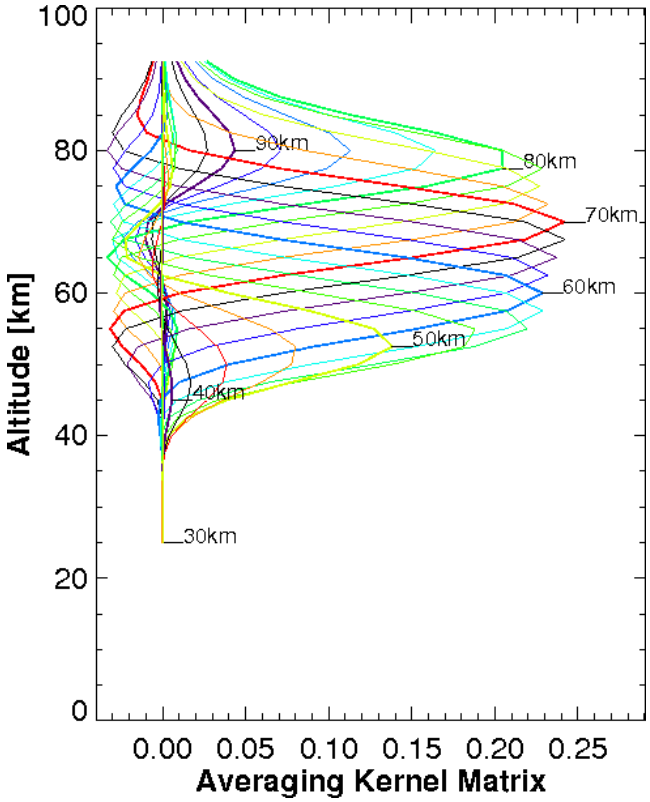

Figure 6.1: Typical averaging kernels from the tidal detection mode. The total integration time amounts to ~180 hours. Even with this long integration time the upper limit of the vertically resolvable water vapor is ≈80 km.

According to Nyquist's sampling theorem only five datapoints/day are needed to avoid aliasing and to properly detect a semidiurnal tide. But with a noisy signal, which is expected to change in phase over time, as many datapoints as possible are preferred. However, in order to reliably observe the water vapor variability at high altitude the integration time needs to be as long as possible. A compromise between these two opposing demands was found in the new moving time-frame integration scheme. It is based on a normal six hour integration, but after six hours of integration on day 1 the scheme will move to day 2 and integrate the same time-frame and add to day 1. Eventually the whole month is integrated and the time-frame is moved two hours and the month is reprocessed. After each integration run the time-window is moved two hours compared to the local time – if the first datapoint was between 00.00 and 06.00, the next one will be 02.00 and 08.00. This results in 12 datapoints during a 24 hour period. This adds up to a total of ~180 hours of integration time for each spectra. Each measurement is given a timestamp according to $T_{start} + t_{int}/2$.

An estimate of the quality of the data can be seen from the averaging kernels shown in Figure 6.1. Averaging kernels are not expected to change significantly between subsequent measurements as long as the measurement itself has a reasonable signal to noise ratio. The kernels can therefore be assumed to be representative for the whole dataset. As can be seen in Figure 6.1 the upper limit of the measurement is still approximately 80 km. The kernel maximum for the higher layers are all located in this altitude which have the effect that any dynamical behavior above 80 km will be projected to this layer in the retrieval.

The tides are assumed to behave as a periodic modulation of the background water

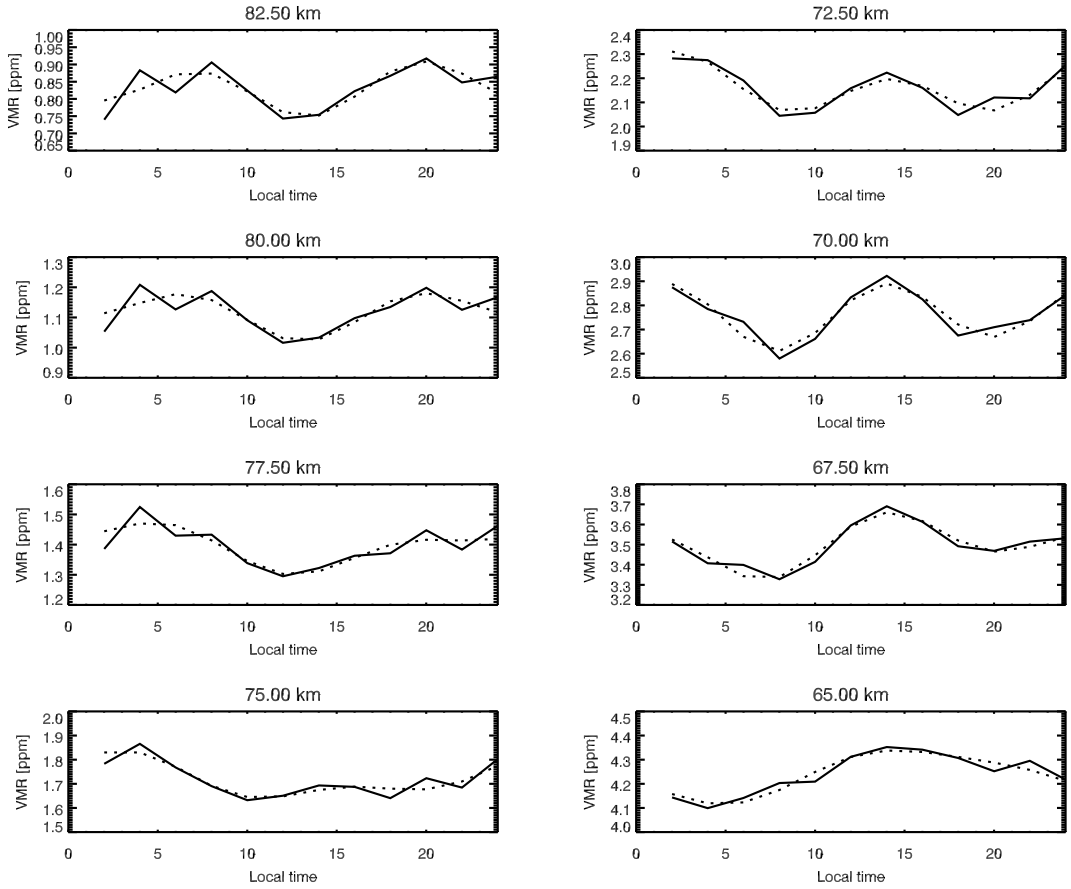

Figure 6.2: The volume mixing ratio as a function of local time for the eight topmost layers, with an altitude difference between each layer of 2.5 km. The solid line is the measured water vapor amount at the local time and the dotted line is the fit according to Eq. 6.1.

vapor. Hence a simple wave-function is used to fit the tides,

$$B + \sum A_i \cdot \cos(\omega_i + \lambda_i) \tag{6.1}$$

where B denotes the background water vapor mixing ratio, A_i the amplitude, ω_i the frequency and λ_i the phase offset. Initially three components of the tide were included in the fit. However, the third, terdiurnal, component was found to be negligible and therefore removed. Thus only the diurnal and semidiurnal modes are addressed in the calculations ($i = 1, 2$). In general, the amplitude of the tides is expected to increase with altitude and therefore the focus was on the tidal behavior in the upper layers (> 55 km) of the retrieval.

6.1.2 Observations of tides in the water vapor

A few cautionary remarks needs to be highlighted before interpreting the results. The detected amplitudes are probably underestimated by two different reasons. One being the integration time of six hours, which acts as a smoothing of the daily variability and hereby reducing the amplitude. The second reason being the construction of a monthly

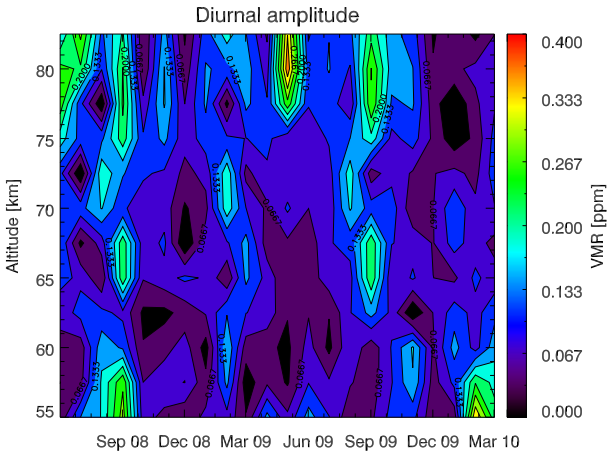

Figure 6.3: A contour plot showing the yearly variability of the amplitude of the diurnal component of the fitted tide. The overall behavior of the diurnal component is relatively stable except for a strong increase in the amplitude at the equinoxes, with the fall equinox being the strongest.

mean, which might introduce additional amplitude suppression if the phase of the tide changes drastically over the averaging interval and causes destructive interference. The Atmospheric Tides Middle Atmosphere Program (see the special issue of *Journal of Atmospheric and Terrestrial Physics*, July/August, 1989) showed that when doing tidal observations it is preferable to average over 10 days or more to isolate the global-scale tidal oscillations of interest from gravity wave interference.

Detection of tidal behavior as measured by ground-based microwave spectroscopy in the alpine region was claimed by Haefele et al. (2008). They compare measurements done by their instrument in Bern to model results. Their approach is to calculate a deviation from a daily mean, and similar to this investigation they use one month of data to produce one daily profile. Initially they present the observations at two pressure (altitude) levels; 3.14 hPa (~40 km) and 0.1 hPa (~70 km) and a deviation from the mean on the order of 1% is found for the lower level and even less at higher levels. Additionally a comparison with GSWM[2] data is done at 65 km altitude, for the diurnal and semidiurnal component separately. It should be noted that these results are for a mid-latitude region which is not expected to show the same behavior as a polar region.

6.1.3 Tidal behavior above ALOMAR

In Figure 6.2 the volume mixing ratio is plotted as a function of local time. The data show is taken from December 2008. Each subplot represents an atmospheric layer, with 2.5 km difference between each vertical layer. No correlation between the layers is introduced in the retrieval although the altitude resolution of the instrument (see Fig. 6.1) is larger than the layer thickness in the forward model. Thus each layer will be affected by layers above and below. The solid line is the measured variability of the water vapor as a function of the local time, and the dotted line is the fit according to Equation 6.1.

The chosen month for Figure 6.2 is completely arbitrary and shows a general behavior of the retrieved volume mixing ratio and how it changes with altitude. It should be noted that the phase and amplitude maximum is not stable and changes over the year, as is suggested by Figure 6.3 and even more so by Figure 6.4. Some months show a stronger

[2]Global Scale Wave Model

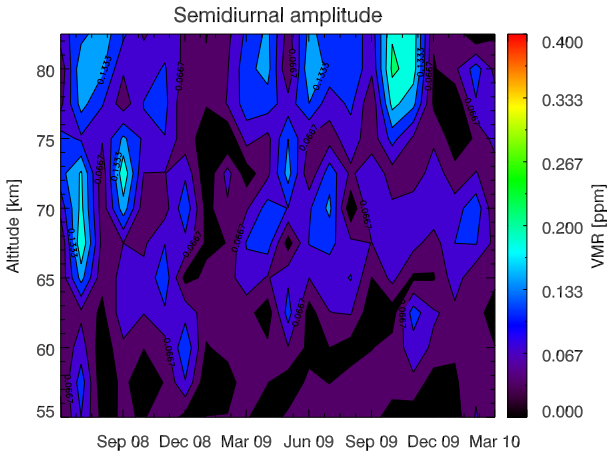

Figure 6.4: As Figure 6.3, but for the semidiurnal part. As opposed to the stable behavior with a few well defined increases in the amplitude of the diurnal component the semidiurnal seem to be more chaotic and no regular behavior can be seen.

diurnal behavior whereas others show a strong semidiurnal behavior, but there are also similarities. The absolute amplitude of the observed tides is generally stable over the year. Thus due to the strong seasonal variability (almost a factor of three at 70 km between summer and winter (Seele and Hartogh 1999)) of the water vapor at these altitudes the relative amplitude of the measured tide is anti-correlated to the background amount of water vapor.

6.1.3.1 Diurnal behavior

As expected from conservation of energy the amplitude of the waves increase as they reach higher altitude and the density of the ambient atmosphere decrease. Forbes (1982a) suggest that the amplitude of the diurnal tide is relatively stable in the middle atmosphere. This behavior can clearly be seen in Figure 6.3, where the amplitude is relatively weak and stable throughout the year, except at the equinoxes where a stronger wave seems to penetrate the stratosphere and affect the lower mesosphere. The maximum amplitude at the equinoxes follow earlier observations (Vincent et al. 1988) and model (Canadian Middle Atmosphere Model) observations (McLandress 1997). However they both deal with wind measurement and do not provide any direct predictions or measurements of water vapor. Nor do any of the used models extend poleward of middle latitudes. The observed amplitude maximum for the wind is located at a slightly higher altitude, ~80 km, compared to the observed maximum in the water vapor, 65 – 70 km. Indications of maximum at higher altitudes (>80 km) can also be seen in Figure 6.3, but this is at the limit of the water vapor measurements and could be a measurement artifact. In addition to the maximum they also mention an amplitude minimum at the solstice. It might well be the case that such a minimum is also present in the water vapor tide. Unusually low values of the diurnal amplitude are visible for June 2009 in Figure 6.3, but this is not conclusive as no such minimum can be seen at any other solstice in the dataset. Furthermore, such a minimum implies a weak signal, which might be too weak for direct detection. However, it could be deduced by statistical means from a longer dataset.

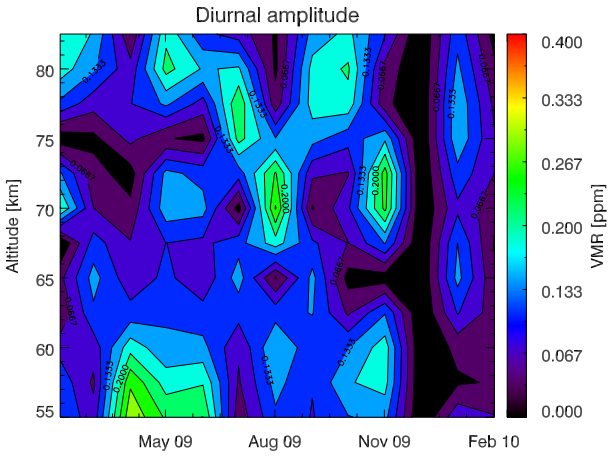

Figure 6.5: The amplitude of the diurnal component above Zugspitze. The instrument was not running during December 2009 thus these values are all set to zero.

6.1.3.2 Semidiurnal behavior

As opposed to the stable and regular behavior of the diurnal tide the amplitude of the semidiurnal tide (Fig. 6.4) shows a more complex behavior in the measured region. The most prominent feature in the dataset is the almost complete lack of semidiurnal component during January 2009. It could be connected to the very strong sudden stratospheric warming which occurred in during this time. It is known that the polar vortex was irreversible broken and this could have had an effect on the propagation of the tides. There do not seem to be an appreciable seasonal variability in the amplitude of the tides, nor any incidents of stronger tidal behavior. Compared to the diurnal component the semidiurnal amplitude seems to be more evenly distributed during the year, with a slight general increase in amplitude during summer.

6.1.3.3 The phase of the observed tides

The phases of the tides are not shown here but according to the climatology of winds and tides in the arctic region presented in Portnyagin et al. (2004) the phases of both the diurnal and semidiurnal tides show a strong dependence on longitude. They should not change significantly over the years. With less than two years worth of tidal observations it is hard to draw any conclusions comparing this claim to the water vapor distribution, and this is therefore left as an open question to be answered when more data has been retrieved.

6.1.4 Observations above Zugspitze

In order to compare the tidal behavior at a mid-latitude site to that of a polar site data collected at Zugspitze have been processed according to the above mentioned scheme. A daily modulation of the observed amount of water vapor, similar to that at ALOMAR, can be fitted to the retrieved data. However, the dataset from Zugspitze is much shorter[3] which severely limits the possibility to deduce a seasonal behavior. The instrumental stop

[3] In the second quarter of 2010 it only spans a year.

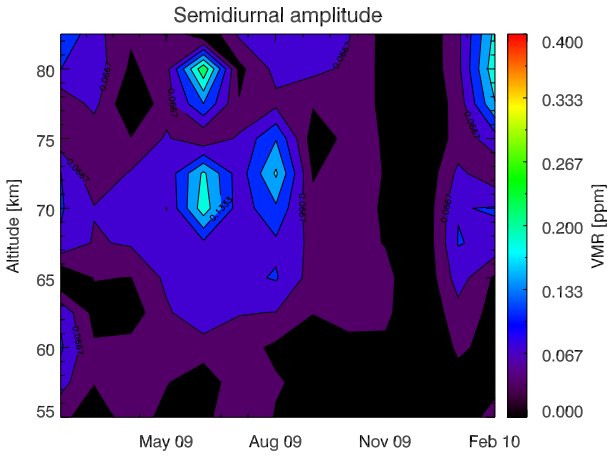

Figure 6.6: As Figure 6.5, but for the semidiurnal component.

during December 2009 is marked as a zero amplitude on all heights and components in the contour plots.

Contour plots similar to the ones presented for ALOMAR can be seen in Figures 6.5 and 6.6. In general the diurnal component seems to have a larger amplitude during the summer season than the winter season. This is also suggested by wind patterns derived from GSWM. However the peak amplitude of the tide at mid-latitudes is lower than the that of the polar latitudes. On the other hand the average amplitude of the tide is higher. In the case of the semidiurnal component the amplitude is in general the weakest of all the detected components for both polar and mid-latitudes. Although, similar to the diurnal component it shows a slightly stronger amplitude during the summer season. The weak amplitude of the semidiurnal component is also observed by Haefele et al. (2008). At 65 km they measure it to have a deviation from the mean of less than 0.5%, which is slightly less than the measurements from cWASPAM. It should be noted that the dataset used in Haefele et al. (2008) is more than three times larger than the current dataset of cWASPAM3.

6.2 Comparison to a planetary and tidal wave model

Portnyagin et al. (2004) show that the dynamical features attributed to tidal behavior in observed data are relatively persistent from year to year. Hence it makes sense to compile this data into climatologies and compare the results to planetary wave models. Currently the dataset is not large enough to be compiled into a climatology of the tidal behavior of water vapor in the polar regions. It is however of interest to know how well the first observations follow model predictions. The observations are likely to be burdened with geophysical small-scale variability which are not covered by the models.

Assuming that water vapor distribution is zonally homogeneous the behavior of the zonal wind is expected to have less influence on the tides than the meridional and vertical wind fields. However, Mayr et al. (2001), concluded that especially the semidiurnal tide is affected by the zonal mean circulation. They also acknowledge a coupling between the diurnal and semidiurnal tide, and the complexity of correctly modeling the latter.

6.2.1 Global Scale Wave Model (GSWM)

The Global Scale Wave Model is a planetary scale wave model developed by Dr. M. Hagan at the High Altitude Observatory (HAO) (Hagan and Forbes 2002, 2003). It is a 2-dimensional model that numerically solves migrating or non-migrating tides. Global steady-state temperature and wind perturbations are used and it extends from ground up to ~125 km. Time (month of the year), height and geographic location are independent variables in the calculations, whereas temperature and wind are dependent. The diurnal and semidiurnal amplitudes and phases are included as dynamical components together with a zonal mean. It is used here to compare the observed monthly variability in water vapor with modeled tidal variability in individual wind and temperature fields. The model has been updated several times, and the next update, GSWM09, is supposed to be publicly available sometime during the first half of 2010 (M. Hagan, *personal communication*).

6.2.2 Comparison to polar latitudes

Modeled wind and temperature fields according to GSWM00 can be seen in Figures 6.7 and 6.8, the former for the diurnal and the latter for the semidiurnal component. GSWM00 models the global behavior of the above mentioned parameters at a longitudinally independent, 3 degree latitudinal grid. The vertical resolution is approximately 4 km/layer. The plots shown are for 66°N, which roughly corresponds to the middle atmosphere observed from ALOMAR.

6.2.2.1 Diurnal tide

To a first approximation there is no single field that expresses the same behavior as observed in the water vapor above ALOMAR. There are however similarities. Curiously the maximum at the equinoxes discussed in Section 6.1.3 seems to be present in the zonal wind, as well as in the vertical wind at high altitude, although weaker. It is however not present in the meridional wind. Both the meridional and vertical wind have a local amplitude maximum at lower altitudes during summer, a time when the water vapor diurnal amplitude is low.

6.2.2.2 Semidiurnal tide

The most striking result in the modeled semidiurnal tides, depicted in Figure 6.8, is the overall weak amplitude compared to the corresponding diurnal tide. The vertical and meridional component seem to be almost identical, however their phases (not shown here) differ greatly. A common feature is a stronger amplitude during the winter months, and a weak local maximum at low altitude during summer. Thus, the weak amplitude and irregular behavior observed in the semidiurnal component of the water vapor (Fig. 6.4) distribution could be caused by the lack of a strong regular influence of the background fields and weaker, irregular incidents may be strong enough to break through the “noise floor” of the general atmospheric behavior.

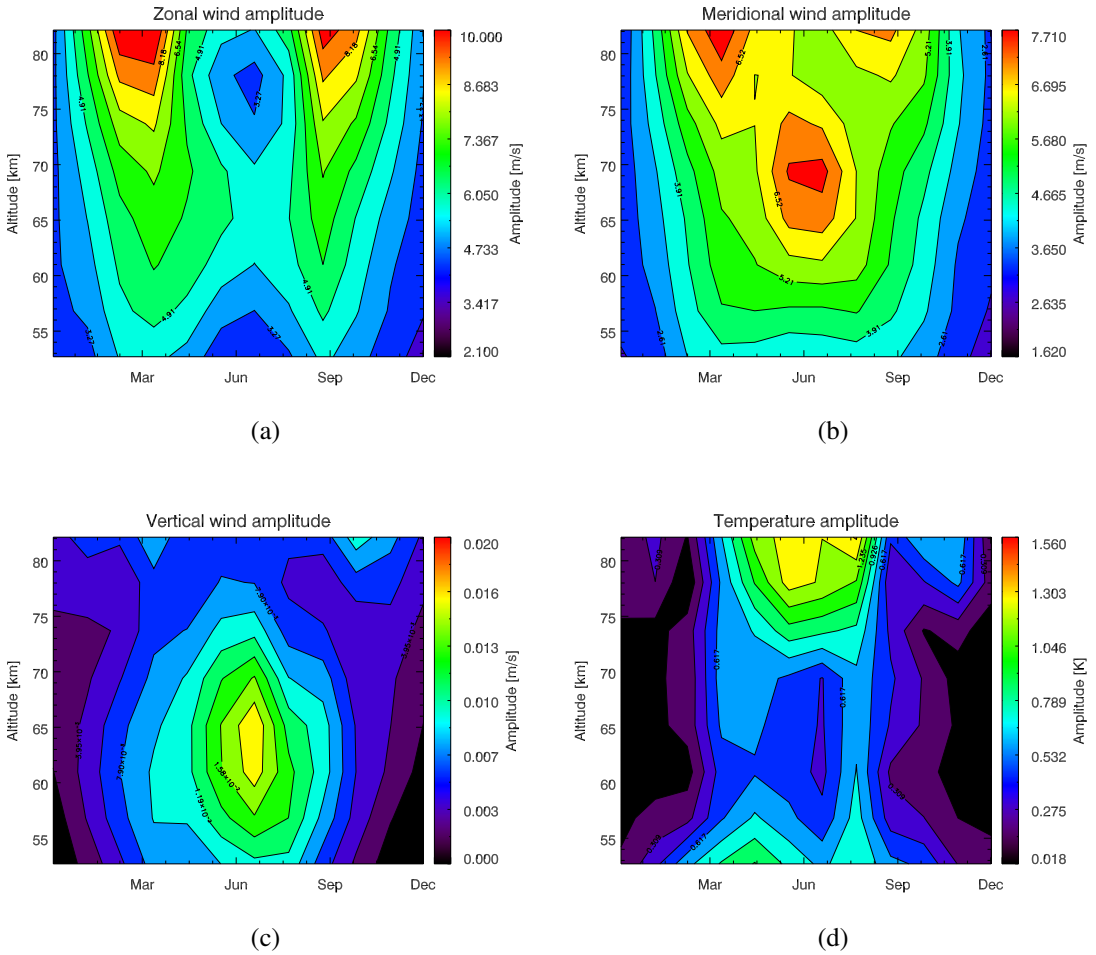

Figure 6.7: The yearly tidal variability for the diurnal component in different wind and temperature fields above ALOMAR according to GSWM00. Fig. 6.7(a) depict the amplitude of the zonal wind with eastward as positive amplitude, Fig. 6.7(b) the meridional wind with north being positive amplitude, Fig. 6.7(c) the vertical wind where upward is the positive direction, and in Fig. 6.7(d) the tidal variability of the temperature field can be seen.

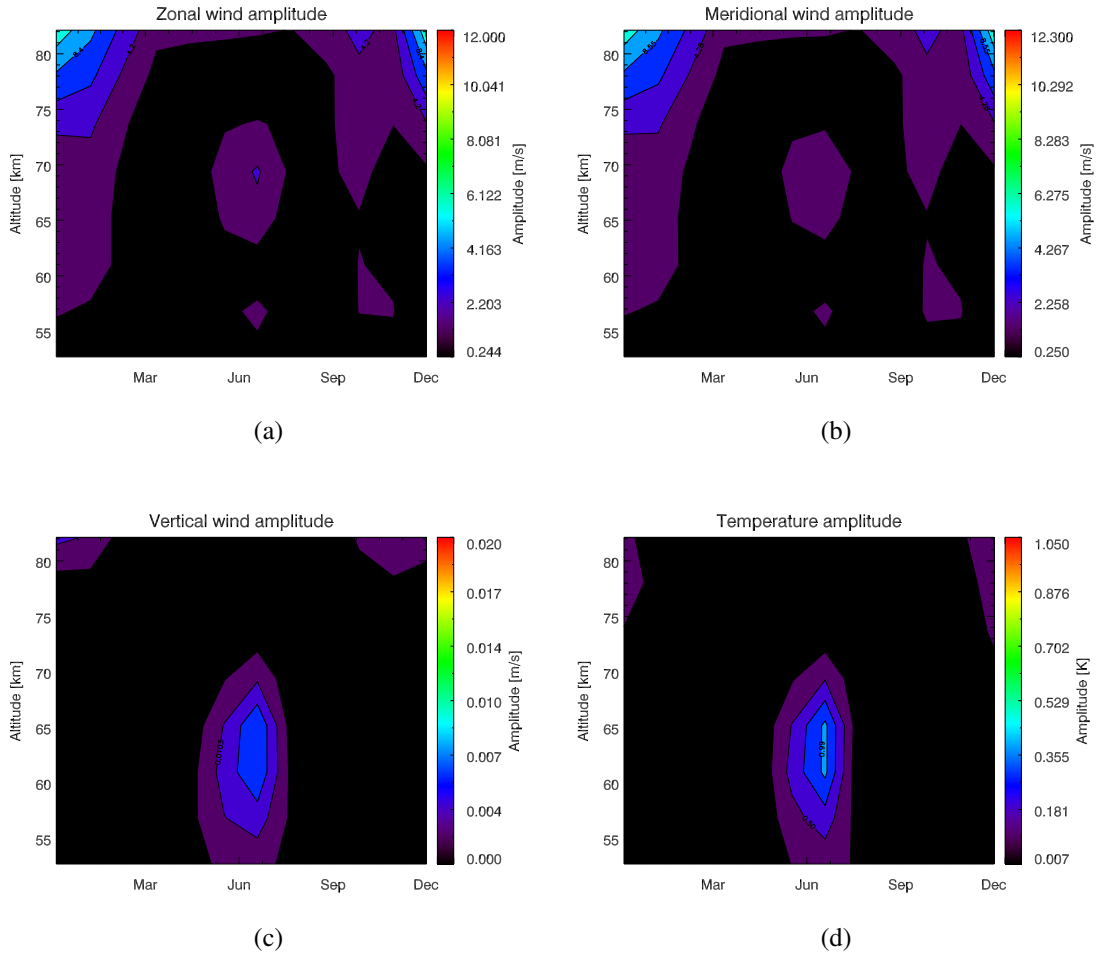

Figure 6.8: As for Figure 6.7 but for semidiurnal components.

6.2.3 Comparison to mid-latitudes

The general behavior of the GSWM for midlatitudes (45°N) shows two distinct patterns, one for the diurnal tide and one for the semidiurnal tide. The same pattern repeats itself for all dynamical fields with only slight differences in altitude and phase. In the case of the diurnal component the maximum amplitude occurs during summer. The phase is relatively stable over the year and is characterized by a slow positive phase shift towards higher altitudes. For the semidiurnal component on the other hand the amplitude maximum occurs over a distinct period around the winter solstice. During the rest of the year the amplitude is in general low and do not show any prominent features.

6.3 Discussion

The averaging kernels presented in Figure 6.1 show that the atmosphere up to 80 km can be resolved fairly well. This can be called the upper limit of the measurement as all information from above this level will be superposed to the 80 km layer. This could, to a certain extent, explain the sometimes irregular behavior at this altitude.

It is important to note that the measured quantity is water vapor, an atmospheric tracer. Water has a long lifetime at these altitudes and the measured variability can therefore be assumed to be a direct result of atmospheric transport. There is no tidal behavior expected to affect the water vapor production (or destruction) itself and the variability shown here should be an effect of tidal behavior in the transport mechanisms in the polar (and mid-latitude) regions. The detected behavior does not follow any single dynamical field according to GSWM, which is to be expected. If a homogenous zonal distribution of water vapor is assumed then the tidal behavior seen is most probably a combination of the meridional and vertical wind. The retrieval is slightly sensitive to changes in the temperature of the background atmosphere. Thus tidal behavior in the atmospheric temperature could introduce artifacts in the measured tide. Recent LIDAR results from ALOMAR (Lübken and Höffner 2010) indicate thermal tides (approximately ±4 K) in the region. However, the LIDAR measurements are constrained to a higher altitude region (85–96 km) than the microwave measurements. The measurements are taken between June and August 2008, and indicate a relatively stable phase similar to the phase seen by this instrument (not shown). Although it cannot be excluded that the cWASPAM measurements are affected by a thermal tide the amplitude of the thermal tide needs to be of the order of ∼10 K to affect the retrievals. On the other hand it should also be noted that results from GSWM09 ((Zhang et al. 2010a) and (Zhang et al. 2010b)) shows a much weaker thermal tide in this region (±1 K). Such a weak oscillation is not expected to affect the measurements to any noticeable degree. More measurements of the thermal tide would be needed to better be able to analyze the correlation between the thermal tide and the detected water vapor tide.

The seemingly random behavior of the semidiurnal amplitude cannot be explained by any current model results and it can therefore not be excluded that the detected signal is a superposition of different wave signatures. It is unlikely that it is randomly occurring gravity waves due to the long integration time, it could however be affected non-migrating tides.

7 Concluding remarks

7.1 The reliability of microwave spectroscopy

Although not directly touched upon in the previous chapters the question of the reliability of the data arises, which is a complicated question to answer. As previously has been discussed there is a multitude of free parameters used in the retrieval. Some of them are empirically determined, some are assumed and others are climatological means.

The nature of the measurement makes it ambiguous, the retrieved spectra alone cannot describe the full state of the atmosphere. Thus, to a certain extent it relies on assumptions to retrieve a vertical distribution profile. The issue of how it is possible to improve water vapor measurements can be divided into two parts; namely a) instrument improvements and b) retrieval improvements. As shown in Figure 4.6 and discussed in the related section this instrument is getting close to the noise limit of microwave spectroscopy of water vapor at 22.235 GHz. Further decreases in T_s will only slightly improve the measurements. In Section 5.2 the possibilities of constraining the amount of water vapor above 80 km are modeled. Even if the system temperature is lowered to 10 K the resulting improvements in the retrieved profile are minimal. Furthermore, as can be seen in Figure 4.6 there is a "knee" similar to a $1/x$-function when the vertical resolution is plotted as a function of integration time. After this knee every increase in vertical resolution (or time resolution) demands an exponentially better instrument. Put in another way, the efforts needed to improve the system temperature are much greater than the increase in data quality.

When it comes to the other part of the problem – the assumptions, some improvements can be done. However they imply collaboration between different fields. A high resolution background atmosphere in terms of temporal resolution especially for the temperature and pressure fields would decrease the uncertainty of the retrieved water vapor profile by a few percent. The a priori profile is a commonly discussed part of the retrieval and as discussed in Section 4.2.5.1 it has a small but non-negligible effect on the retrieved profile. However the use of a static or a dynamic a priori profile is a matter which is still under discussion and the optimal solution is to a large extent dependent on what the water profiles are used for.

7.1.1 Absolute values versus measured variability

Following the above discussion it becomes clear that there might be a difference between the measured and the true amount of water vapor in the atmosphere. This offset is unknown and it might be different at different altitudes, see for example the difference in

measured water vapor between our instrument and EOS-MLS[1] in Figures 5.1 and 5.2. However, if the instrument is stable[2] and the data always are processed in an identical way then the difference between the true and measured atmospheric water vapor content can be assumed to be constant and variability and long term trends can be successfully derived from the data.

7.1.2 Validation of data

By validating the data knowledge of how the instrument compares to other similar instruments and models can be gained. Aside from the obvious importance of knowing how well the profiles retrieved with instrument proves to be in relation to others there is another advantage offered by data validation. Ground-based instruments normally have a nearly continuous local time coverage over the region where it measures, space-based instruments on the other hand usually have very good spatial coverage but are limited when it comes to the temporal coverage at a given location. In order to be able to use data from different instruments in larger campaigns it is vital to know how the individually retrieved profiles compare to others as well as if any instrumental biases are present and how they affect the measurements. Such an intercomparison campaign was carried out in the beginning of 2009 and the results are currently analyzed and will be presented in a publication sometime during the second half of 2010. The comparison between the herein presented instrument and EOS-MLS is however finished. Systematic minor differences exist but the overall behavior indicates a good agreement.

7.2 Water vapor observations

Water vapor measurements have been carried out above ALOMAR since 1996. A paper discussing the variability and trends over the last solar cycle in comparison with LIMA has been published (Hartogh et al. 2010). Thus the analysis of the long term dataset in Section 5.3.2 was instead focused on a yearly water vapor climatology. At low altitudes (50 – 60 km) the inter-annual differences are largest during winter, which is to be expected as the stratosphere is more dynamic during this time. In the upper layers on the other hand the variability is larger during summer. However, this could be influenced less by the year to year variability than a result a depletion which occurred between 2001 – 2003. In general, the annual cycle is stable with the onset of water vapor increase in the upper atmosphere occurring at almost the same time every year. This is also true for the onset of the reversal of the process, when the amounts of water vapor start to decrease.

The behavior of the water vapor distribution over both ALOMAR and Zugspitze for 2009 is presented and compared, with ALOMAR representing a polar latitude location and the associated pure annual variability. Zugspitze on the other hand is a mid-latitude location and the characterization of the annual behavior is more ambiguous. It seems to be in a transition zone between the annual and semi-annual oscillation. There are indications of a weak semi-annual oscillation in the stratosphere and an annual oscillation in the

[1] Note that it is a difference in the measured profile. It is not known whether the cWASPAM, EOS-MLS profiles or both are incorrect.

[2] By stable is meant no instrumental drifts over a longer timespan.

mesosphere. Unfortunately there was a hardware problem and the dataset do not yet fully cover all seasons. Furthermore two stratospheric warmings occurred, one during spring and one early winter which could increase a false positive of the semi-annual oscillation signal.

Yet another sudden stratospheric warming occurred in January 2010. It was observed by all instruments and is discussed in detail in Section 5.4 with high time-resolution distribution maps from ALOMAR, IAP Kühlungsborn and Zugspitze. It is concluded that the more southern the location, the earlier the increase in water vapor can be seen. The change of the transport patterns caused by the warmings decrease or reverse the easterlies and associated wintertime downwelling and instead more humid air from the tropics are transported into the higher latitudes resulting in a strong increase in measured water vapor.

7.3 Tides

One of the main objectives of the new instrument was to detect daily variability, or tides, in the middle atmospheric water vapor distribution. A daily variability in the water vapor have indeed been detected at ALOMAR as well as Zugspitze, which is believed to be caused by tides. The tidal behavior differs between the locations as expected from models. However, whereas the data from ALOMAR spans almost two years the data available from Zugspitze so far only span slightly more than a year which makes it hard to deduce any seasonal behavior.

The most prominent feature in the ALOMAR tidal behavior is the maximum amplitude of the diurnal component around the equinoxes, and especially the fall equinox. The general diurnal component is somewhat stronger above Zugspitze than ALOMAR but the opposite is true for the semidiurnal component. A recent publication by Lübken and Höffner (2010) discuss detections of a thermal tide above ALOMAR. The thermal tide detected is located at higher altitudes than our measurements. A thermal tide could introduce a retrieval artifact in the form of a false detection of a water vapor tide. Although the amplitude of these detections are in general larger than the predictions from GSWM09 any such artifact caused by temperature variabilities is unlikely. Simulations show that in order to introduce water vapor variabilities with the detected amplitudes a thermal tide in our sensitive region need to have an amplitude of approximately 10 K peak to peak, which is larger than the detected variability.

7.4 Outlook

The validation campaign at Zugspitze, ARIS, is slowly coming to an end with the actual comparisons being undertaken in the second quarter of 2010. It is expected to increase our knowledge in how different microwave spectrometers setup, backend and retrieval affects the deduced atmospheric profile. It will also result in a atmospheric mapping of the water vapor during the campaign that extend much lower into the atmosphere than what only cWASPAM can measure.

As mentioned in Sections 7.2 and 7.3 there are a lot of open questions concerning the behavior above Zugspitze. Some of these questions are primarily due to a too short

dataset, and are expected to be better understood as the dataset increases. For instance the unresolved issue of the annual behavior — is there a semi-annual component, and how strong is it compared to the annual? A shortage of data is also a burden for the tide detection which affect the possibility for an in-depth quantitative investigation. However, for every month the tidal detection dataset is expanded and increase the possibility to conduct a proper seasonal investigation.

The long term dataset acquired over ALOMAR has gone into its second solar cycle and the dataset is continuously being extended. These measurements can soon be correlated to measurements carried out by almost identical instruments at a number locations in Europe. This opens for possibilities to correlate the behavior at each location and constrain transport mechanisms. At a first instance there is the north-south line ALOMAR-Kühlungsborn-Zugspitze which can help us understand the meridional transport processes and speeds. There is also a discussion with the University of Bern to conduct an in-depth analysis of the last years sudden stratospheric warmings. Depending on time of the SSW the number of involved instruments would differ. Although there are observations from at least 2 different locations for each incident. In the case of the SSW discussed in Section 5.4 the locations already covering the event would be extended by a radiometer in Finland (approximately same latitude as ALOMAR but 10 degrees more eastward), as well as a number of instruments in Bern (pointing north-northeast). Such extended coverage is expected to greatly improve the possibility to constrain and follow the transport mechanisms responsible for the increase of water vapor in the middle atmosphere during such an event.

A A technical description of the frontend

A.1 The instrument dewar

The dewar itself is an aluminum cube measuring 50 x 60 x 68.5 cm. On the front there are three PTFE (Teflon®) windows, one for each load and one for the antenna. PTFE was chosen because of its high transparency in the 22 GHz frequency range. Although PTFE has a very high transparency reflections occur in the air/PTFE interfaces. In order to minimize the attenuating effects of the internal reflections the window thickness has been tuned by high-precision milling (with an accuracy of ∼2 μm rms)(Seele 1999). Behind each window there are three infrared filters [1] which serve to reduce the impact of the incoming room temperature infrared radiation affecting the loads and the antenna. In addition the loads are encapsulated in metal cylinders to further block thermal infrared radiation from the dewar walls. The calibration loads are made out of pourable lossy magnetic material, C-RAM[2], and are cast in a pyramidal shape in order to reduce reflections from the load surface.

A rotating mirror switches the incoming signal between the calibration loads or the atmosphere, and reflects it into the cooled horn antenna. The received signal is directly split into its horizontal and vertical polarization, and hereafter amplified by the HEMTs. In order to suppress the lower sideband the incoming signal is filtered by a bandpass filter with 1.5 GHz bandwidth, centered at 22 GHz. The filter characteristics can be seen in Figure A.1. The mixing frequency of the LO is 20.885 GHz which place the lower sideband at at 19.535 GHz. At this frequency is the suppression ∼-45 dB. It is marked as 'Mkr 2' in the above mentioned figure. The input frequency of the CTS is 1.35 GHz, which is also the resulting IF-frequency after down-conversion.

A.1.1 Cooling and vacuum

By cooling the first stage in the instrument the thermal noise in the system can be greatly reduced. If cooled to below 20 K the indium phosphate (InP) HEMT amplifiers have a noise temperature of ∼15 K (roughly equal to a noise factor of 0.3 dB) and an amplification of 32 dB. According to Friis equation (Eq. A.1) a very high gain and low noise in the

[1] (Zytex®)
[2] KR-112 from Cuming Microwave Corp.

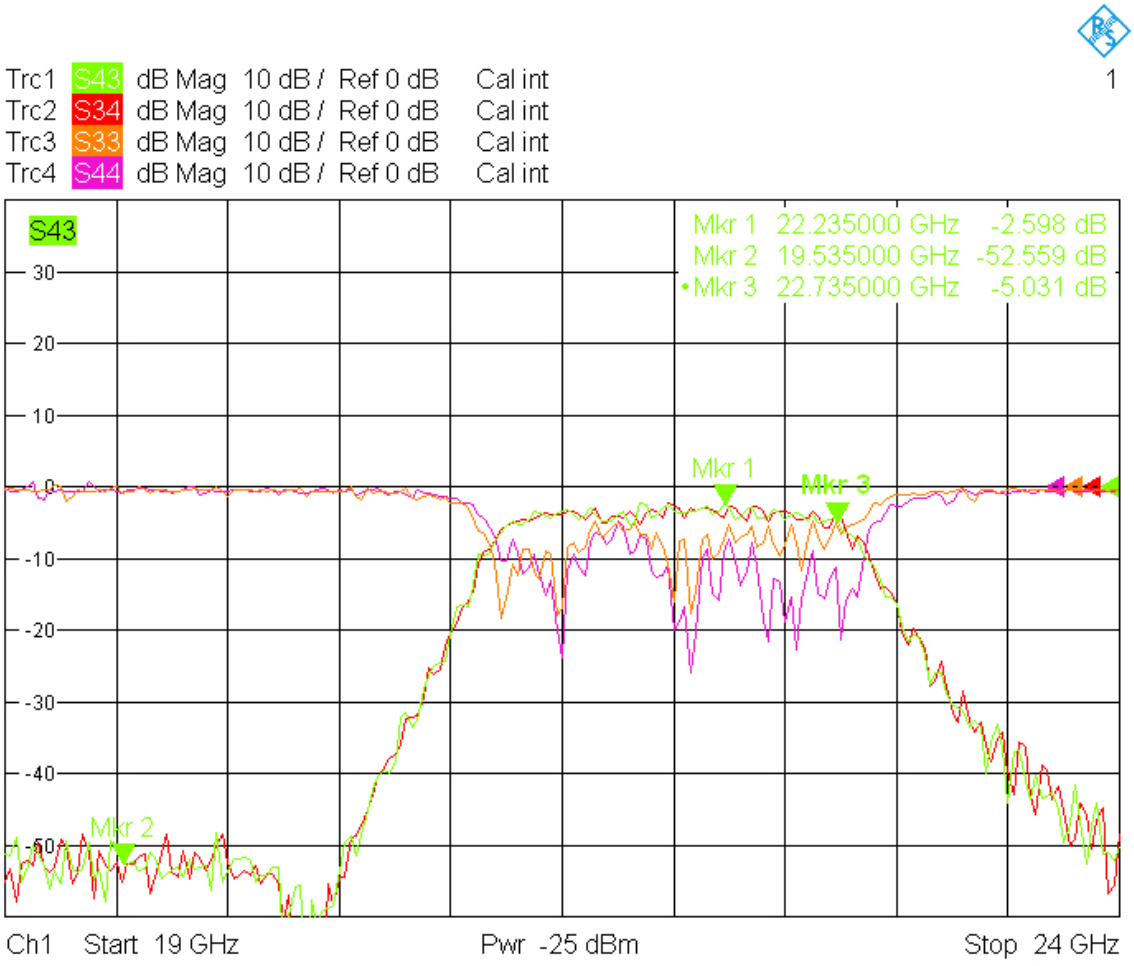

Figure A.1: The measured sideband suppression of the first bandpass filter, which is the first component on the IF electronics box. Marker (Mkr) 1 is located at the frequency of the water vapor transition we are measuring and shows the corresponding attenuation whereas marker 2 is located at the lower sideband (19.535 GHz). The sideband suppression can be read out and is ∼-45dB.

first stage reduce the impact of later noise.

$$F = F_1 + \frac{F_2 - 1}{G_1} + \frac{F_3 - 1}{G_1 \cdot G_2} + \frac{F_4 - 1}{G_1 \cdot G_2 \cdot G_3} \ldots, \tag{A.1}$$

where F gives the total noise of the chain. F_i is the noise factor at each step and G_i is the corresponding gain, both given as linear ratios. By calculating the total noise figure we find that approximately 99% of the total noise is introduced at the LNA-stage.

An 8 kW helium cooling compressor is used to cool the system. It is a Gifford McMahon type 3-phase compressor from Sumitomo HI[3] with a cooling capacity at the first stage of 35 W at 45 K and 6.3 W at 10 K at the second stage. The model is a stable closed loop system which requires minimal maintenance. The actual cold finger is mounted inside the dewar where the antenna and the OMT/HEMT amplifier bundle are directly connected to

[3]The coldhead is the RDK408S2-model and the compressor itself is CSA-71A, an air-cooled indoor model.

it (see Figure 3.4). The calibration loads are kept at a higher temperature than the antenna bundle and are connected to the first cooling stage by copper braids with different thermal resistance in order to achieve different load temperatures.

To avoid air condensing and freezing (the main issue being water, carbon dioxide and nitrogen) on the antenna and other cold components in the dewar it is evacuated and kept under vacuum at all times. A diaphragm pump is used in series with a molecular turbo pump to assure that the low pressure is kept. Under normal operating conditions it is on the order of 10^{-7} mbar.

A.2 Chopper Controller

Between each step in the measurement cycle the mirror is rotated so that the spectrum is taken either from a calibration load or the sky. A "chopper controller" is responsible for a fast and correct rotation of the mirror. The positions for the calibration loads and the correct elevation angle are preset by three different potentiometers. A fourth reference position is also available for calibration against liquid nitrogen. By switching between different "master" potentiometers, the viewing angle of the mirror can be changed. When the controlling potentiometer is changed a voltage difference between the mirror potentiometer and the position potentiometer arise. A control-loop with a PID regulator feed an analog DC motor which rotates the mirror until the sought position is reached. The time needed to change between different viewing angles of the mirror is on the order of a few hundred milliseconds, depending on the rotation angle. Command control of the rotation is carried out by the process-control computer during normal operation. A local control mode is available to simplify calibration.

A.3 Wobbling table

Reflections between the load and antenna windows in the dewar occur because the transparency is not 100% at 22 GHz. Such reflections give rise to standing waves between the windows, which interfere with the measurements and should therefore be minimized.

To reduce standing waves the mirrors are mounted on a movable table. The table itself can be moved back and forth by a computer-controlled stepper motor. By carefully controlling the pathlength difference, a destructive interference can be created and the standing waves reduced (Gustincic 1977). The geometric length of the movement is a multiple of the transition frequency wavelength (1.35 cm). A movement with distance d will result in a pathlength difference of $2d$ due to the optical setup. For detailed calculations on the needed pathlength variations of the movement see Appendix B. This method reduces the inference of standing waves in the baseline by one or two orders of magnitude.

The movement is synchronized with the spectrometers, *i.e.* one measurement of the atmosphere will take place at the same time as the table moves forward. Consequently, during load measurements, the table will move the same distance backwards and end up at the initial position, ready for a new atmospheric measurement.

A.3.1 Wobbler control

Low-latency of the process-control computer is vital for the control of the wobbler for two reasons, 1) the synchronization with the CTSs as no actual sync signal is sent between the processes, and 2) the wobbling movement is controlled by sending TTL signals through the parallel port. One square wave is translated by the stepper controller to one step by the motor. The repeatability of the stepper itself is ±0.01 mm. Accurate movement of the optical table is crucial for a correct removal of the standing waves, thus the wobbler-control software is specially developed to be real-time proof (see Section 3.3).

B Wobbling equations

B.1 General approach

The following equation can be set up for a power spectrum received by a radiometer system, including general parameters for echoes in the signal:

$$g(t) = \sqrt{1-a}f(t) + \sqrt{a}f(t-\tau), \tag{B.1}$$

where τ is the delay time between original signal and the echo, and a denotes the amplitude relation between the echo and the original signal. $a = 1$ means that all the power in the signal is contained in the echo and consequentially $a = 0$ means that all the power is in the original signal (no echo).

Equation B.1 is transformed into the frequency domain according to:

$$G(\omega) = \frac{1}{\sqrt{2\pi}} \int_{-\infty}^{+\infty} g(t)e^{-i\omega t}d \tag{B.2a}$$

$$= \dots \tag{B.2b}$$

$$= \sqrt{1-a}F(\omega) + \sqrt{a}\frac{1}{\sqrt{2\pi}} \int_{-\infty}^{+\infty} f(t-\tau)e^{-i\omega t}dt. \tag{B.2c}$$

By substituting $t - \tau$ to x this leads to:

$$G(\omega) = \sqrt{1-a}F(\omega) + \sqrt{a}\frac{1}{\sqrt{2\pi}} \int_{-\infty}^{+\infty} f(x)e^{-i\omega(x+tau)}dx \tag{B.3a}$$

$$= \dots \tag{B.3b}$$

$$= (\sqrt{1-a} + \sqrt{a}e^{-iw\tau})F(w). \tag{B.3c}$$

$\mid G(\omega)^2 \mid$ is obtained by multiplying Equation B.3 with its conjugate complex:

$$\mid G(\omega)^2 \mid = (\sqrt{1-a} + \sqrt{a}e^{-iw\tau})(\sqrt{1-a} + \sqrt{a}e^{+iw\tau}) \mid F(\omega) \mid^2 \tag{B.4a}$$

$$= \dots \tag{B.4b}$$

$$= (1 + \sqrt{1-a}\sqrt{a}2\cos(\omega\tau)) \mid F(\omega) \mid^2 . \tag{B.4c}$$

The right hand side of Equation B.4, $(1 + \sqrt{1-a}\sqrt{a}2\cos(\omega\tau))$ describes a sine-like modulation of the true power spectrum $\mid F(\omega) \mid^2$ with a period $2\pi/\tau$.

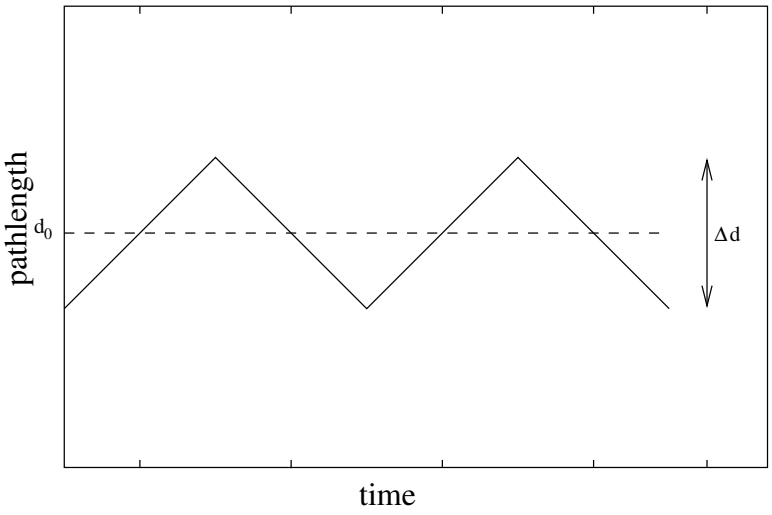

Figure B.1: Sawtooth-like pathlength variation

B.2 System specific approach

The basic idea behind pathlength wobbling is that for a certain frequency, f, there should exist a corresponding optic pathlength modulation which, if periodically applied, will reduce the baseline ripples of the power spectrum.

To find the pathlength variation that would reduce the baseline ripple to zero the following equation needs to be solved:

$$\frac{1}{\Delta t}\int_0^{\Delta t}\cos(\omega\tau(t))dt = 0 \tag{B.5}$$

Using a linear wobbling mechanism a sawtooth-like pattern for the pathlength variation will appear, see Figure B.1. Denoting the period $2T$ the function can be written as:

$$\tau(t) = \tau_0 + \frac{\Delta\tau}{T}t \tag{B.6}$$

Thus,

$$\frac{1}{\Delta t}\int_0^{\Delta t}\cos(\omega(\tau_0 + \frac{\Delta\tau}{T}t)dt = 0, \tag{B.7}$$

needs to be solved. Substitute according to:

$$x = \frac{\Delta\tau}{T}t \;\Rightarrow\; dt = \frac{T}{\Delta\tau}dx, \tag{B.8}$$

and integrate over a half a period, $\Delta\tau = T$, leads to:

$$\frac{1}{T}\frac{T}{\Delta\tau}\int_0^{T}\cos(\omega(\tau_0 + x))dx. \tag{B.9}$$

Trigonometric formulae leads to:

$$\frac{1}{\Delta\tau}\int_0^{T}[\cos(\omega\tau_0)\cos(\omega x) - \sin(\omega\tau_0)\sin(\omega x)]dx, \tag{B.10}$$

and

$$\frac{1}{\Delta\tau}\left[\frac{\cos(\omega\tau_0)}{\Delta\tau}\int_0^{\Delta\tau}\cos(\omega x)dx - \frac{\sin(\omega\tau_0)}{\Delta\tau}\int_0^{\Delta\tau}\sin(\omega x)dx\right]. \tag{B.11}$$

Solving the terms separately leads to:

$$\frac{1}{\Delta\tau\omega}[\cos(\omega\tau_0)\cdot\sin(\omega\Delta\tau)], \tag{B.12}$$

and

$$\frac{\sin(\omega\tau_0)}{\Delta\tau}\left[\frac{1}{\omega}\cos(\omega\Delta\tau) - \frac{1}{\omega}\right]. \tag{B.13}$$

Adding Equations B.12 and B.13 and collecting terms, with respect to sin, gives:

$$\frac{1}{\omega\Delta\tau}\left[\sin(\omega\tau_0 + \omega\Delta\tau) - \sin(\omega\tau_0)\right]. \tag{B.14}$$

When Equation B.14 equals zero a complete reduction of the ripples is reached (the trivial solution). The non-trivial solution can be found by solving

$$\sin(\omega\tau_0 + \omega\Delta\tau) = \sin(\omega\tau_0). \tag{B.15}$$

Using, $\omega = 2\pi f$, $\Delta\tau = d/c$ and $\lambda = c/f$ this leads to:

$$\sin\left(\frac{2\pi d_0}{\lambda} + \frac{2\pi\Delta d}{\lambda}\right) = \sin\left(\frac{2\pi d_0}{\lambda}\right), \tag{B.16}$$

where d is the pathlength in m.
This is true for:

$$\frac{\Delta d}{\lambda} = 1 \quad \Rightarrow \Delta d = n\cdot\lambda, \tag{B.17}$$

thus for maximum suppression of standing waves in the optical path the pathlength should be varied by a multiple of the wavelength.

C The optimal estimation method

A more rigorous description of the optimal estimation method will be given in following Section.

C.1 Mathematical description of the optimal estimation method

We start by referring to Equation 2.10, which is the forward model in vector form, see Section 2.1.1:

$$\boldsymbol{y} = \boldsymbol{K} \cdot \boldsymbol{x}. \tag{C.1}$$

If Equation C.1 is instead seen as a sum we can note it as

$$y_j = \sum_{i=1}^{n} K_{ij} x_i. \tag{C.2}$$

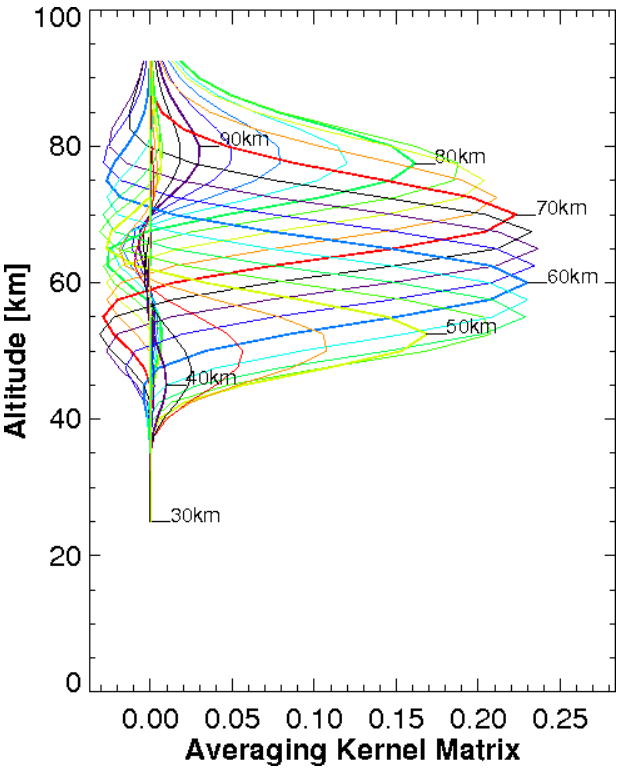

Figure C.1: A typical averaging kernel matrix. This one in particular is from a spectra with 24 hour integration time. The observation was conducted on May the 2nd, 2009, by cWASPAM1 at ALOMAR.

It can be understood that the number of spectral channels, j, needed for a unique solution needs to be larger, or at least as large as the number of layers, i, in the modeled atmosphere. With modern spectrometers, having thousands of channels, this is however rarely a problem. But, on the other hand experimental noise is inevitably present and we can in general not expect to be able to find a unique solution. The approach to use is to look for a "best approximation" of the true solution. A *least squares* solution tries to find the minimum according to:

$$(\boldsymbol{y} - \boldsymbol{K} \cdot \hat{\boldsymbol{x}})^2 = \text{minimum}. \tag{C.3}$$

Including error covariance matrices, S_y, this results in:

$$\hat{\boldsymbol{x}} = (\boldsymbol{K}^T \boldsymbol{S}_y^{-1} \boldsymbol{K})^{-1} \boldsymbol{K}^T \boldsymbol{S}_y^{-1} \boldsymbol{y}, \tag{C.4}$$

with the covariance as

$$\hat{\boldsymbol{S}} = (\boldsymbol{K}^T \boldsymbol{S}_y^{-1} \boldsymbol{K})^{-1}. \tag{C.5}$$

This will numerically give a very good solution, however the resulting profile is completely useless. In essence the algorithm will fit small scale noise as part of the true line which introduce a strong oscillation in the retrieved profile. For a rigorous discussion on the cause for this behavior see Jarchow (1998).

The *Optimal Estimation Method* (OEM) is can be used to constrain the solution and overcome this problem. It is essentially based on the optimal way of combining two independent measurements, x_1 and x_2, of the same parameter, by taking the average of the variances as weights (cf. Equation 4.1),

$$\hat{x} = \left(\frac{1}{\sigma_1^2} + \frac{1}{\sigma_2^2}\right)^{-1} \left(\frac{x_1}{\sigma_1^2} + \frac{x_2}{\sigma_2^2}\right), \tag{C.6}$$

with $\hat{x}$ as the estimate of the combined measurements. The variances of each measurement are denoted $1/\sigma_1$ and $1/\sigma_2$, giving the variance of $\hat{x}$

$$\hat{\sigma}^2 = \left(\frac{1}{\sigma_1^2} + \frac{1}{\sigma_2^2}\right)^{-1}. \tag{C.7}$$

This can easily be applied to vector quantities $\boldsymbol{x}_i$ with corresponding covariances $\boldsymbol{S}_i$:

$$\hat{\boldsymbol{x}} = (\boldsymbol{S_1}^{-1} + \boldsymbol{S_2}^{-1})^{-1} \cdot (\boldsymbol{S_1}^{-1} \cdot \boldsymbol{x_1} + \boldsymbol{S_2}^{-1} \cdot \boldsymbol{x_2}), \tag{C.8}$$

and covariance according to

$$\hat{\boldsymbol{S}} = (\boldsymbol{S_1}^{-1} + \boldsymbol{S_2}^{-1})^{-1}. \tag{C.9}$$

We insert the least squares solution found in Equation C.4 and C.5, as well as the corresponding covariance for the measured profile as $\boldsymbol{x_2}$. We introduce an independent measurement as $\boldsymbol{x_1}$. It is independent in the sense that there is no correlation between the error covariances of $\boldsymbol{x_1}$ and $\boldsymbol{x_2}$. The origin, or method of finding $\boldsymbol{x_1}$ is irrelevant and it can in this case be thought of as a *virtual* measurement. The a priori profile with a corresponding

estimated covariance can therefor be used. Following the original notation by Rodgers (1976) where the a priori is denoted $\boldsymbol{x_0}$ we obtain:

$$\hat{\boldsymbol{x}} = (\boldsymbol{S_0}^{-1} + \boldsymbol{K}^T\boldsymbol{S_y}^{-1}\boldsymbol{K})^{-1}(\boldsymbol{S_0}^{-1}\boldsymbol{x_0} + \boldsymbol{K}^T\boldsymbol{S_y}^{-1}\boldsymbol{y}), \tag{C.10}$$

with covariance

$$\hat{\boldsymbol{S}} = (\boldsymbol{S_0}^{-1} + \boldsymbol{K}^T\boldsymbol{S_y}^{-1}\boldsymbol{K})^{-1}. \tag{C.11}$$

The combination of profiles can be thought of as if the a priori profile provides a smooth fine structure whereas the measured profile will provide a gross behavior. This way the result will never be worse than the a priori profile, hence it will always produce a reasonable profile. During bad observational conditions the measurements will inevitably have a worse variance and the result will tend to the a priori. It is then obvious that the choice of the a priori profile affect the result and it should therefore be carefully chosen, see the discussion in Section 4.2.5.1. To quantify the weights, that is how much information in the resulting profile is taken from the a priori and how much from the measurement we define the contribution function $\boldsymbol{D}$ as:

$$\boldsymbol{D} \equiv \frac{\partial \hat{\boldsymbol{x}}}{\partial \boldsymbol{y}} = (\boldsymbol{S_0}^{-1} + \boldsymbol{K}^T\boldsymbol{S_y}^{-1}\boldsymbol{K})^{-1} \cdot \boldsymbol{K}^T\boldsymbol{S_y}^{-1}, \tag{C.12}$$

and the averaging kernel $\boldsymbol{A}$ as:

$$\boldsymbol{A} \equiv \boldsymbol{D} \cdot \boldsymbol{K}. \tag{C.13}$$

Equation C.10 can now be rewritten as:

$$\begin{aligned}
\hat{\boldsymbol{x}} &= (\boldsymbol{S_0}^{-1} + \boldsymbol{K}^T\boldsymbol{S_y}^{-1}\boldsymbol{K})^{-1}(\boldsymbol{S_0}^{-1}\boldsymbol{x_0} + \boldsymbol{K}^T\boldsymbol{S_y}^{-1}\boldsymbol{y}) && \text{(C.14a)}\\
&= (\boldsymbol{S_0}^{-1} + \boldsymbol{K}^T\boldsymbol{S_y}^{-1}\boldsymbol{K})^{-1}(((\boldsymbol{S_0}^{-1} + \boldsymbol{K}^T\boldsymbol{S_y}^{-1}\boldsymbol{K}) - \boldsymbol{K}^T\boldsymbol{S_y}^{-1}\boldsymbol{K})\boldsymbol{x_0} + \boldsymbol{K}^T\boldsymbol{S_y}^{-1}\boldsymbol{y}) && \text{(C.14b)}\\
&= (1 - (\boldsymbol{S_0}^{-1} + \boldsymbol{K}^T\boldsymbol{S_y}^{-1}\boldsymbol{K})^{-1}\boldsymbol{K}^T\boldsymbol{S_y}^{-1}\boldsymbol{K})\boldsymbol{x_0} + (\boldsymbol{S_0}^{-1} + \boldsymbol{K}^T\boldsymbol{S_y}^{-1}\boldsymbol{K})^{-1}\boldsymbol{K}^T\boldsymbol{S_y}^{-1}\boldsymbol{y} && \text{(C.14c)}\\
&= (1 - \boldsymbol{D}\boldsymbol{K})\boldsymbol{x_0} + \boldsymbol{D}\boldsymbol{y}. && \text{(C.14d)}
\end{aligned}$$

Recalling Equation 2.10 and adding an error, ϵ_y, to the measurement we have:

$$\begin{aligned}
\hat{\boldsymbol{x}} &= (1 - \boldsymbol{D}\boldsymbol{K})\boldsymbol{x_0} + \boldsymbol{D}(\boldsymbol{K}\boldsymbol{x} + \epsilon_y) && \text{(C.15a)}\\
&= (1 - \boldsymbol{D}\boldsymbol{K})\boldsymbol{x_0} + \boldsymbol{D}\boldsymbol{K}\boldsymbol{x} + \boldsymbol{D}\epsilon_y && \text{(C.15b)}\\
&= (1 - \boldsymbol{A})\boldsymbol{x_0} + \boldsymbol{A}\boldsymbol{x} + \boldsymbol{D}\epsilon_y && \text{(C.15c)}
\end{aligned}$$

The measurement $\boldsymbol{y}$ is now split into the true spectrum $\boldsymbol{K}\boldsymbol{y}$ and the measurement error ϵ_y. Furthermore, the role of the averaging kernel $\boldsymbol{A}$ as a measure of the quality of the profile is clarified. Ideally $\boldsymbol{A}$ is the identity matrix $\mathbf{1}$, where every change in layer n in the true profile would be transferred to an equal change in the measured profile. For ground-based microwave spectroscopy $\boldsymbol{A}$ is however often very different from the identity matrix $\mathbf{1}$, a consequence of the low vertical resolution. In reality, when layer n change in the true profile the information will get smeared out over several layers by the averaging kernel. For a discussion on the relationship between the vertical resolution and integration time

see Section 4.2.4. If we reformulate Equation C.15c to include the absolute error, $(\hat{\boldsymbol{x}} - \boldsymbol{x})$, we get

$$\hat{\boldsymbol{x}} = (1 - \boldsymbol{A})\boldsymbol{x}_0 + \boldsymbol{A}\boldsymbol{x} + \boldsymbol{D}\boldsymbol{\epsilon}_y \tag{C.16a}$$

$$= (1 - \boldsymbol{A})\boldsymbol{x}_0 + 1\boldsymbol{x} - 1\boldsymbol{x} + \boldsymbol{A}\boldsymbol{x} + \boldsymbol{D}\boldsymbol{\epsilon}_y \tag{C.16b}$$

$$(\hat{\boldsymbol{x}} - \boldsymbol{x}) = (1 - \boldsymbol{A})(\boldsymbol{x}_0 - \boldsymbol{x}) + \boldsymbol{D}\boldsymbol{\epsilon}_y. \tag{C.16c}$$

Now the two error terms can be distinguished; the *measurement noise error* ϵ_y, with the corresponding covariance $\boldsymbol{D}\boldsymbol{S}_y\boldsymbol{D}^T$, and the difference between the a priori profile and the true profile $(\boldsymbol{x_0} - \boldsymbol{x})$. The latter term is introduced by Rodgers (1990) and denoted *null space error*. A more detailed discussion on those two terms can be found in the same paper. The covariance matrix of the null space error is $(1 - \boldsymbol{A})\boldsymbol{S_0}(1 - \boldsymbol{A})^T$ and the covariance matrix for the full inversion can now be described as:

$$\hat{\boldsymbol{S}} = (1 - \boldsymbol{A})\boldsymbol{S_0}(1 - \boldsymbol{A}^T) + \boldsymbol{D}\boldsymbol{S}_y\boldsymbol{D}^T. \tag{C.17}$$

D Climatology of water vapor above ALOMAR

With the large dataset discussed in Section 5.3.2 it was possible to construct a climatology for ALOMAR. Figure 5.5 shows how the water vapor have changed during the time we have observed water vapor above ALOMAR. The mean behavior for the same time-span at different altitudes can be seen in Figure 5.6. The full dataset, of which Figure 5.6 only shows four distinct layers, is given in Table D.1. It contains the altitudes we are sensible to (40 – 85 km). Even though the upper- and lowermost layers are heavily influence by the a priori profile they are included for completeness. The background atmosphere used in the retrieval assume a layered structure with 2.5 km altitude difference between each layer thus the retrieved profile will be built on a similar layer setup. The water vapor values in the table are in ppmv and the time as the week of the year.

Table D.1: A water vapor climatology for ALOMAR, collected between 1996 – 2009. The water vapor values are given as ppmv.

Week / Z[km]	40.00	42.50	45.00	47.50	50.00	52.50	55.00	57.50	60.00	62.50	65.00	67.50	70.00	72.50	75.00	77.50	80.00	82.50	85.00
1	7.12	7.12	6.92	6.57	6.21	5.94	5.78	5.66	5.44	5.03	4.38	3.57	2.78	2.15	1.72	1.42	1.15	0.86	0.54
2	7.12	7.12	6.93	6.61	6.26	5.96	5.72	5.48	5.18	4.74	4.12	3.36	2.60	1.99	1.57	1.28	1.03	0.76	0.46
3	7.12	7.15	6.98	6.63	6.25	5.94	5.71	5.47	5.11	4.61	3.95	3.24	2.61	2.14	1.80	1.53	1.26	0.95	0.61
4	7.15	7.19	7.00	6.58	6.08	5.61	5.24	4.92	4.59	4.19	3.68	3.14	2.63	2.22	1.92	1.67	1.40	1.08	0.71
5	7.15	7.25	7.15	6.82	6.31	5.76	5.28	4.92	4.64	4.29	3.82	3.24	2.63	2.10	1.69	1.38	1.11	0.82	0.52
6	7.16	7.23	7.08	6.72	6.25	5.80	5.46	5.22	4.97	4.60	4.03	3.30	2.56	1.97	1.58	1.32	1.09	0.84	0.55
7	7.20	7.28	7.10	6.71	6.22	5.74	5.33	4.95	4.57	4.10	3.52	2.91	2.38	1.99	1.75	1.57	1.37	1.09	0.76
8	7.18	7.26	7.11	6.77	6.35	5.91	5.49	5.11	4.72	4.25	3.68	3.04	2.44	1.94	1.58	1.32	1.09	0.84	0.55
9	7.20	7.27	7.11	6.74	6.25	5.77	5.38	5.09	4.80	4.42	3.91	3.29	2.67	2.15	1.76	1.47	1.21	0.94	0.63
10	7.17	7.23	7.08	6.72	6.23	5.71	5.30	5.03	4.81	4.47	3.92	3.21	2.51	1.96	1.60	1.35	1.13	0.89	0.61
11	7.18	7.24	7.08	6.72	6.25	5.82	5.49	5.29	5.11	4.77	4.20	3.42	2.63	2.02	1.62	1.36	1.15	0.93	0.66
12	7.20	7.31	7.23	6.97	6.60	6.19	5.86	5.64	5.47	5.18	4.67	3.94	3.13	2.43	1.90	1.53	1.23	0.96	0.66
13	7.25	7.38	7.28	6.96	6.54	6.12	5.81	5.62	5.47	5.15	4.57	3.80	3.00	2.35	1.87	1.52	1.24	0.97	0.68
14	7.20	7.31	7.27	7.06	6.73	6.33	5.97	5.68	5.44	5.10	4.54	3.78	2.95	2.26	1.77	1.44	1.21	0.99	0.73
15	7.18	7.30	7.27	7.08	6.77	6.41	6.05	5.77	5.53	5.20	4.68	3.95	3.11	2.35	1.78	1.39	1.12	0.91	0.67
16	7.20	7.33	7.32	7.16	6.88	6.53	6.19	5.91	5.68	5.38	4.89	4.23	3.48	2.79	2.22	1.76	1.39	1.08	0.78
17	7.21	7.35	7.36	7.21	6.93	6.59	6.22	5.90	5.62	5.28	4.80	4.19	3.47	2.81	2.27	1.87	1.55	1.25	0.91
18	7.21	7.36	7.37	7.21	6.91	6.54	6.18	5.92	5.73	5.54	5.19	4.66	3.97	3.28	2.68	2.18	1.77	1.39	0.99
19	7.20	7.34	7.32	7.13	6.80	6.39	6.02	5.77	5.65	5.57	5.38	5.01	4.48	3.90	3.35	2.84	2.35	1.83	1.30
20	7.21	7.36	7.37	7.22	6.93	6.56	6.22	5.98	5.86	5.76	5.59	5.28	4.88	4.45	3.98	3.46	2.86	2.21	1.55
21	7.21	7.37	7.39	7.26	6.97	6.61	6.24	5.99	5.89	5.90	5.88	5.74	5.46	5.08	4.62	4.05	3.35	2.56	1.78
22	7.21	7.36	7.38	7.25	6.98	6.62	6.26	6.02	5.93	5.97	6.04	6.00	5.81	5.48	4.99	4.34	3.56	2.70	1.87
23	7.21	7.38	7.42	7.31	7.08	6.76	6.45	6.23	6.15	6.17	6.19	6.13	5.96	5.71	5.31	4.69	3.84	2.89	1.96
24	7.22	7.40	7.46	7.38	7.16	6.84	6.51	6.26	6.15	6.18	6.25	6.27	6.16	5.91	5.47	4.80	3.90	2.91	1.95
25	7.22	7.40	7.47	7.40	7.19	6.89	6.58	6.37	6.32	6.37	6.43	6.40	6.24	5.99	5.60	5.00	4.14	3.11	2.09
26	7.20	7.37	7.42	7.36	7.18	6.93	6.66	6.46	6.38	6.37	6.36	6.29	6.13	5.89	5.49	4.86	3.98	2.95	1.97
27	7.22	7.40	7.48	7.43	7.24	6.94	6.62	6.40	6.37	6.51	6.73	6.89	6.85	6.58	6.02	5.19	4.16	3.05	2.03
28	7.22	7.41	7.48	7.43	7.25	7.00	6.73	6.55	6.52	6.62	6.78	6.90	6.86	6.65	6.16	5.35	4.29	3.12	2.06
29	7.21	7.40	7.47	7.43	7.26	7.02	6.78	6.63	6.60	6.69	6.80	6.86	6.78	6.55	6.07	5.27	4.24	3.09	2.04
30	7.22	7.40	7.48	7.44	7.30	7.09	6.86	6.70	6.65	6.72	6.82	6.89	6.85	6.67	6.21	5.44	4.38	3.20	2.11
31	7.22	7.40	7.48	7.43	7.26	7.00	6.72	6.54	6.51	6.65	6.85	6.99	6.96	6.74	6.23	5.40	4.32	3.16	2.09
32	7.21	7.38	7.44	7.39	7.24	7.02	6.79	6.62	6.58	6.67	6.81	6.91	6.88	6.71	6.29	5.53	4.49	3.31	2.20
33	7.21	7.39	7.45	7.39	7.22	6.98	6.75	6.63	6.74	6.86	6.90	6.90	6.77	6.52	6.02	5.23	4.21	3.10	2.07
34	7.22	7.39	7.44	7.36	7.15	6.87	6.65	6.56	6.64	6.82	6.95	6.92	6.71	6.35	5.80	5.02	4.07	3.03	2.06
35	7.22	7.39	7.44	7.34	7.12	6.81	6.53	6.40	6.45	6.63	6.79	6.78	6.60	6.21	5.62	4.83	3.91	2.94	2.02
36	7.21	7.41	7.46	7.38	7.16	6.86	6.57	6.43	6.49	6.69	6.87	6.89	6.70	6.26	5.60	4.75	3.79	2.81	1.92
37	7.24	7.43	7.48	7.37	7.12	6.82	6.59	6.55	6.69	6.88	6.94	6.74	6.29	5.65	4.89	4.06	3.21	2.39	1.64
38	7.22	7.38	7.40	7.27	7.08	6.93	6.86	6.87	6.92	6.89	6.66	6.21	5.57	4.86	4.13	3.43	2.74	2.07	1.43
39	7.21	7.39	7.46	7.45	7.34	7.18	7.04	6.96	6.90	6.77	6.48	5.98	5.32	4.54	3.72	2.94	2.26	1.66	1.12
40	7.24	7.43	7.47	7.40	7.27	7.17	7.10	7.04	6.91	6.59	6.03	5.22	4.31	3.47	2.78	2.22	1.76	1.34	0.92
41	7.21	7.36	7.36	7.27	7.15	7.05	6.95	6.79	6.48	5.97	5.32	4.55	3.77	3.08	2.51	2.05	1.64	1.25	0.86
42	7.21	7.30	7.18	6.90	6.60	6.36	6.16	5.92	5.58	5.06	4.40	3.62	2.88	2.28	1.85	1.53	1.26	0.97	0.67
43	7.19	7.29	7.20	6.93	6.57	6.21	5.91	5.64	5.34	4.90	4.35	3.72	3.11	2.60	2.18	1.84	1.51	1.17	0.80
44	7.13	7.12	6.85	6.38	5.86	5.46	5.23	5.12	4.99	4.73	4.27	3.66	3.04	2.52	2.12	1.79	1.49	1.15	0.79
45	7.13	7.10	6.76	6.21	5.65	5.23	5.01	4.89	4.71	4.39	3.87	3.27	2.69	2.23	1.89	1.63	1.36	1.06	0.73
46	7.15	7.10	6.76	6.25	5.74	5.37	5.14	4.95	4.65	4.22	3.64	3.05	2.54	2.15	1.86	1.61	1.34	1.04	0.69
47	7.13	7.08	6.74	6.21	5.69	5.35	5.17	5.01	4.73	4.28	3.67	3.03	2.46	2.04	1.75	1.52	1.27	0.98	0.65
48	7.07	6.91	6.42	5.72	5.05	4.59	4.34	4.14	3.84	3.39	2.80	2.21	1.76	1.50	1.36	1.25	1.11	0.88	0.59
49	7.14	7.08	6.76	6.27	5.78	5.38	5.10	4.86	4.56	4.15	3.59	2.97	2.41	1.98	1.68	1.45	1.21	0.93	0.60
50	7.15	7.14	6.91	6.56	6.20	5.90	5.68	5.44	5.11	4.64	4.00	3.29	2.64	2.13	1.77	1.50	1.23	0.92	0.59
51	7.16	7.16	6.95	6.62	6.27	5.97	5.73	5.47	5.11	4.59	3.89	3.10	2.39	1.87	1.54	1.31	1.10	0.85	0.55
52	7.04	6.99	6.77	6.44	6.14	5.92	5.71	5.41	4.94	4.39	3.70	2.98	2.34	1.88	1.56	1.33	1.11	0.84	0.54

Bibliography

Backus, G., Gilbert, F., 1970, Uniqueness in the Inversion of Inaccurate Gross Earth Data, Royal Society of London Philosophical Transactions Series A, 266, 123–192

Beaudin, G., Gulkis, S., Frerking, M., Hartogh, P., Allen, M., Bockelee-Morvan, D., Crovisier, J., Despois, D., Encrenaz, P., Encrenaz, T., Germain, B., Hofstadter, M., Ip, W., Janssen, J., Lellouch, E., Mann, I., Muhleman, D., Rauer, H., Schloerb, F. P., Spilker, T., 1998, A microwave radiometer/spectrometer for the ROSETTA orbiter, in Proceedings of the 2nd ESA Workshop on Millimetre Wave Technology and Applications: Antennas, Circuits and Systems, (Eds.) J. Mallat, A. Räisänen, J. Tuovinen, ESA WPP-149, pp. 43–48, ESA Publ. Div., ESPOO, Finland

Berger, U., 2008, Modeling of middle atmosphere dynamics with LIMA, Journal of Atmospheric and Solar-Terrestrial Physics, 70, 1170–1200

Chandrasekhar, S., 1960, Radiative Transfer, Dover, New York

Chapman, S., Lindzen, R., 1970, Atmospheric tides. Thermal and gravitational, Dordrecht: Reidel

Curtis, A. R., Goody, R. M., 1956, Thermal Radiation in the Upper Atmosphere, Royal Society of London Proceedings Series A, 236, 193–206

Darlington, S., 1964, Demodulation of wideband, low–power FM signals., Bell Syst. Tech. J., 43

Dlugokencky, E. J., Houweling, S., Bruhwiler, L., Masarie, K. A., Lang, P. M., Miller, J. B., Tans, P. P., 2003, Atmospheric methane levels off: Temporary pause or a new steady-state?, Geophysical Research Letters, 30

Dlugokencky, E. J., Bruhwiler, L., White, J. W. C., Emmons, L. K., Novelli, P. C., Montzka, S. A., Masarie, K. A., Lang, P. M., Crotwell, A. M., Miller, J. B., Gatti, L. V., 2009, Observational constraints on recent increases in the atmospheric CH_4 burden, Geophysical Research Letters, 36, 18 803–+

Forbes, J. M., 1982a, Atmospheric tides. I - Model description and results for the solar diurnal component., Journal of Geophysical Research, 87, 5222–5241

Forbes, J. M., 1982b, Atmospheric tides. II - The solar and lunar semidiurnal components, Journal of Geophysical Research, 87, 5241–5252

Forbes, J. M., 1995, The upper Mesosphere and Lower Thermosphere: A Review of Experiment and Theory, Geophysical Monograph 87, chap. Tidal and Planetary Waves, pp. 67–+

Fritts, D. C., Alexander, M. J., 2003, Gravity wave dynamics and effects in the middle atmosphere, Reviews of Geophysics, 41, 1003–+

Fritts, D. C., Vincent, R. A., 1987, Mesospheric momentum flux studies at Adelaide, Australia - Observations and a gravity wave-tidal interaction model, Journal of Atmospheric Sciences, 44, 605–619

Gadsden, M., Schröder, W., 1989, Noctilucent clouds (Physics and Chemistry in Space), Springer

Garcia, R. R., Marsh, D. R., Kinnison, D. E., Boville, B. A., Sassi, F., 2007, Simulation of secular trends in the middle atmosphere, 1950-2003, Journal of Geophysical Research (Atmospheres), 112, 9301–+

Geller, M. A., 1979, Dynamics of the middle atmosphere, Journal of Atmospheric and Terrestrial Physics, 41, 683 – 705, ISSN 0021-9169

Gulkis, S., Allen, M., Backus, C., Beaudin, G., Biver, N., Bockelée-Morvan, D., Crovisier, J., Despois, D., Encrenaz, P., Frerking, M., Hofstadter, M., Hartogh, P., Ip, W., Janssen, M., Kamp, L., Koch, T., Lellouch, E., Mann, I., Muhleman, D., Rauer, H., Schloerb, P., Spilker, T., 2007, Remote sensing of a comet at millimeter and submillimeter wavelengths from an orbiting spacecraft, Planetary and Space Science, 55, 1050–1057

Gustincic, J. J., 1977, A quasi optical receiver system, in IEEE Conference Proceeding on MTT, pp. 99–100

Haefele, A., Hocke, K., Kämpfer, N., Keckhut, P., Marchand, M., Bekki, S., Morel, B., Egorova, T., Rozanov, E., 2008, Diurnal changes in middle atmospheric H_2O and O_3: Observations in the Alpine region and climate models, Journal of Geophysical Research (Atmospheres), 113, 17 303–+

Haefele, A., De Wachter, E., Hocke, K., Kämpfer, N., Nedoluha, G. E., Gomez, R. M., Eriksson, P., Forkman, P., Lambert, A., Schwartz, M. J., 2009, Validation of ground-based microwave radiometers at 22 GHz for stratospheric and mesospheric water vapor, Journal of Geophysical Research (Atmospheres), 114, 23 305–+

Hagan, M. E., Forbes, J. M., 2002, Migrating and nonmigrating diurnal tides in the middle and upper atmosphere excited by tropospheric latent heat release, Journal of Geophysical Research (Atmospheres), 107, 4754–+

Hagan, M. E., Forbes, J. M., 2003, Migrating and nonmigrating semidiurnal tides in the upper atmosphere excited by tropospheric latent heat release, Journal of Geophysical Research (Space Physics), 108, 1062–+

Hallgren, K., Hartogh, P., Jarchow, C., 2010, A New, High-performance, Heterodyne Spectrometer for Ground-based Remote Sensing of Mesospheric Water Vapour, vol. 19, pp. 569–578, World Scientific Publishing Co.

Hartogh, P., Hartmann, G. K., 1990, A high-resolution chirp transform spectrometer for microwave measurements., Measurement Science and Technology, 1, 592–595

Hartogh, P., Jarchow, C., 1995a, Groundbased microwave detection of middle atmospheric ozone, in Global Process Monitoring and Remote Sensing of Ocean and Sea Ice, EUROPTO-Series 2586, pp. 206–214, SPIE, Bellingham

Hartogh, P., Jarchow, C., 1995b, Groundbased detection of middle atmospheric water vapor, in Global Process Monitoring and Remote Sensing of Ocean and Sea Ice, EUROPTO-Series 2586, pp. 188–195, SPIE, Bellingham

Hartogh, P., Jarchow, C., Sonnemann, G. R., Grygalashvyly, M., 2004, On the spatiotemporal behavior of ozone within the upper mesosphere/mesopause region under nearly polar night conditions, Journal of Geophysical Research (Atmospheres), 109, 18 303–+

Hartogh, P., Sonnemann, G. R., Grygalashvyly, M., Song, L., Berger, U., Lübken, F., 2010, Water vapor measurements at ALOMAR over a solar cycle compared with model calculations by LIMA, Journal of Geophysical Research (Atmospheres), 115, 0–+

Hedin, A. E., 1991, Extension of the MSIS thermosphere model into the middle and lower atmosphere, Journal of Geophysical Research, 96, 1159–1172

Hochschild, G., Gross, J., Hoffman, P., Kopp, G., 2008, Observation of stratospherical trace gases by millimeter wave radiometry in tropical south america.

Holton, J. R., Haynes, P. H., McIntyre, M. E., Douglass, A. R., Rood, R. B., Pfister, L., 1995, Stratosphere-troposphere exchange, Reviews of Geophysics, 33, 403–439

Ingold, T., Peter, R., Kämpfer, N., 1998, Weighted mean tropospheric temperature and transmittance determination at millimeter-wave frequencies for ground-based applications, Radio Science, 33, 905–918

Jack, M., Paige, E., 1978, Fourier Transformation Processors Based on Surface Acoustic Wave Chirp Filters, Wave Electronics, 3, 229 – 247

Jack, M., Grant, P., Collins, J., 1980, The theory, design, and applications of surface acoustic wave fourier-transform processors, Proceedings of the IEEE, 68, 450–468, ISSN 0018-9219

Janssen, M. A. (Ed.), 1993, Atmospheric Remote Sensing By Microwave Radiometry. Editor, Michael A. Janssen; Wiley, New York, NY, 1993. LC # QC871 .J26 1993. ISBN # 0471628913.

Jarchow, C., 1998, Bestimmung atmosphärischer Wasserdampf- und Ozonprofile mittels bodengebundener Millimeterwellen-Fernerkundung, Ph.D. thesis, Universität Bremen, Bremen

Jarchow, C., Hartogh, P., 1995, Retrieval of data from ground-based microwave sensing of the middle atmosphere: Comparison of two inversion techniques, in Global Process Monitoring and Remote Sensing of Ocean and Sea Ice, EUROPTO-Series 2586, pp. 196–205, SPIE, Bellingham

Klauder, J. R., Price, A. C., Darlington, S., Albersheim, W. J., 1960, The theory and design of chirp radars., Bell Syst. Tech. J., 39, 745–808

Lambert, A., Read, W. G., Livesey, N. J., Santee, M. L., Manney, G. L., Froidevaux, L., Wu, D. L., Schwartz, M. J., Pumphrey, H. C., Jimenez, C., Nedoluha, G. E., Cofield, R. E., Cuddy, D. T., Daffer, W. H., Drouin, B. J., Fuller, R. A., Jarnot, R. F., Knosp, B. W., Pickett, H. M., Perun, V. S., Snyder, W. V., Stek, P. C., Thurstans, R. P., Wagner, P. A., Waters, J. W., Jucks, K. W., Toon, G. C., Stachnik, R. A., Bernath, P. F., Boone, C. D., Walker, K. A., Urban, J., Murtagh, D., Elkins, J. W., Atlas, E., 2007, Validation of the Aura Microwave Limb Sounder middle atmosphere water vapor and nitrous oxide measurements, Journal of Geophysical Research (Atmospheres), 112, 24–+

Laštovička, J., 2009, Global pattern of trends in the upper atmosphere and ionosphere: Recent progress, Journal of Atmospheric and Solar-Terrestrial Physics, 71, 1514–1528

Liebe, H. J., 1989, MPM - An atmospheric millimeter-wave propagation model, International Journal of Infrared and Millimeter Waves, 10, 631–650

Liebe, H. J., Hufford, G. A., Cotton, M. G., Y. P. Yee, R. A. Sutherland, & J. L. Cogan (Eds.), 1993, Propagation modeling of moist air and suspended water/ice particles at frequencies below 1000 GHz

Lindzen, R. A., 2005, Dynamics in Atmospheric Physics, Cambridge University Press

Lossow, S., Urban, J., Gumbel, J., Eriksson, P., Murtagh, D., 2008, Observations of the mesospheric semi-annual oscillation (MSAO) in water vapour by Odin/SMR, Atmospheric Chemistry & Physics, 8, 6527–6540

Lossow, S., Urban, J., Schmidt, H., Marsh, D. R., Gumbel, J., Eriksson, P., Murtagh, D., 2009, Wintertime water vapor in the polar upper mesosphere and lower thermosphere: First satellite observations by Odin submillimeter radiometer, Journal of Geophysical Research (Atmospheres), 114, 10 304–+

Lübken, F., 1999, Thermal structure of the arctic summer mesosphere, Journal of Geophysical Research, 104, 9135–9150

Lübken, F., Höffner, J., 2004, Experimental evidence for ice particle interaction with metal atoms at the high latitude summer mesopause region, Geophysical Research Letters, 31, 8103–+

Lübken, F.-J., Höffner, J., 2010, First measurements of thermal tides in the summer polar mesopause region, Geophysical Research Letters, Submitted

Manney, G. L., Schwartz, M. J., Krüger, K., Santee, M. L., Pawson, S., Lee, J. N., Daffer, W. H., Fuller, R. A., Livesey, N. J., 2009, Aura Microwave Limb Sounder observations of dynamics and transport during the record-breaking 2009 Arctic stratospheric major warming, Geophysical Research Letters, 36, 12 815–+

Manson, A. H., Meek, C. E., 1986, Dynamics of the middle atmosphere at Saskatoon (52 deg N, 107 deg W) - A spectral study during 1981, 1982, Journal of Atmospheric and Terrestrial Physics, 48, 1039–1055

Matsuno, T., 1971, A Dynamical Model of the Stratospheric Sudden Warming., Journal of Atmospheric Sciences, 28, 1479–1494

Mayr, H. G., Mengel, J. G., 2005, Interannual variations of the diurnal tide in the mesosphere generated by the quasi-biennial oscillation, Journal of Geophysical Research (Atmospheres), 110, 10 111–+

Mayr, H. G., Mengel, J. G., Chan, K. L., Porter, H. S., 2001, Mesosphere dynamics with gravity wave forcing: Part I. Diurnal and semi-diurnal tides, Journal of Atmospheric and Solar-Terrestrial Physics, 63, 1851–1864

McLandress, C., 1997, Seasonal variability of the diurnal tide: Results from the Canadian middle atmosphere general circulation model, Journal of Geophysical Research, 102, 29 747–29 764

McPherson, R. D., Bergman, K. H., Kistler, R. E., Rasch, G. E., Gordon, D. S., 1979, The NMC Operational Global Data Assimilation System, Monthly Weather Review, 107, 1445–+

Nedoluha, G. E., Bevilacqua, R. M., Michael Gomez, R., Waltman, W. B., Hicks, B. C., Thacker, D. L., Andrew Matthews, W., 1996, Measurements of water vapor in the middle atmosphere and implications for mesospheric transport, Journal of Geophysical Research, 101, 21 183–21 194

Paganini, L., Hartogh, P., 2007, Description of a new 400 mhz bandwidth chirp transform spectrometer, in Advances in Geosciences: Planetary Science, (Ed.) A. e. a. Bhardwaj, vol. 7, pp. 55–68, World Scientific Publishing Co.

Paganini, L., Hartogh, P., 2009, Analysis of nonlinear effects in microwave spectrometers, Journal of Geophysical Research (Atmospheres), 114, 13 305–+

Pickett, H. M., Poynter, I. R. L., Cohen, E. A., Delitsky, M. L., Pearson, J. C., Muller, H. S. P., 1998, Submillimeter, millimeter and microwave spectral line catalog., Journal of Quantitative Spectroscopy and Radiative Transfer, 60, 883–890

Portnyagin, Y., Solovjova, T., Makarov, N., Merzlyakov, E., Manson, A., Meek, C., Hocking, W., Mitchell, N., Pancheva, D., Hoffmann, P., Singer, W., Murayama, Y., Igarashi, K., Forbes, J., Palo, S., Hall, C., Nozawa, S., 2004, Monthly mean climatology of the prevailing winds and tides in the Arctic mesosphere/lower thermosphere, Annales Geophysicae, 22, 3395–3410

Randel, W. J., Wu, F., Vömel, H., Nedoluha, G. E., Forster, P., 2006, Decreases in stratospheric water vapor after 2001: Links to changes in the tropical tropopause and the Brewer-Dobson circulation, Journal of Geophysical Research (Atmospheres), 111, 12 312–+

Rapp, M., Lübken, F.-J., 2004, Polar mesosphere summer echoes (pmse): review of current observations and understanding, Atmospheric Chemistry and Physics, pp. 2601–2633

Rees, D., Barnett, J. J., Labitzke, K., 1990, COSPAR International Reference Atmosphere: 1986. Pt. 2: Middle atmosphere models, Advances in Space Research, 10

Rigby, M., Prinn, R. G., Fraser, P. J., Simmonds, P. G., Langenfelds, R. L., Huang, J., Cunnold, D. M., Steele, L. P., Krummel, P. B., Weiss, R. F., O'Doherty, S., Salameh, P. K., Wang, H. J., Harth, C. M., Mühle, J., Porter, L. W., 2008, Renewed growth of atmospheric methane, Geophysical Research Letters, 35, 22 805–+

Rodgers, C. D., 1976, Retrieval of Atmospheric Temperature and Composition From Remote Measurements of Thermal Radiation, Reviews of Geophysics and Space Physics, 14, 609–+

Rodgers, C. D., 1990, Characterization and error analysis of profiles retrieved from remote sounding measurements, Journal of Geophysical Research, 95, 5587–5595

Rosenlof, K. H., Reid, G. C., 2008, Trends in the temperature and water vapor content of the tropical lower stratosphere: Sea surface connection, Journal of Geophysical Research (Atmospheres), 113, 6107–+

Seele, C., 1999, Bodengebundene Mikrowellenspektroskopie von Wasserdampf in der polaren mittleren Atmosphäre, Ph.D. thesis, Universität Bonn

Seele, C., Hartogh, P., 1999, Water vapor of the polar middle atmosphere: Annual variation and summer mesosphere conditions as observed by ground-based microwave spectroscopy., Geophysical Research Letters, 26, 1517–1520

Seele, C., Hartogh, P., 2000, A case study on middle atmospheric water vapor transport during the february 1998 stratospheric warming, Geophysical Research Letters, 26, 3309–3312

Shepherd, G. G., Roble, R. G., Zhang, S., McLandress, C., Wiens, R. H., 1998, Tidal influence on midlatitude airglow: Comparison of satellite and ground-based observations with TIME-GCM predictions, Journal of Geophysical Research, 103, 14 741–14 752

Shepherd, T. G., 2000, The middle atmosphere, Journal of Atmospheric and Solar-Terrestrial Physics, 62, 1587–1601

Siskind, D. E., Coy, L., Espy, P., 2005, Observations of stratospheric warmings and mesospheric coolings by the TIMED SABER instrument, Geophysical Research Letters, 32, 9804–+

Sonnemann, G. R., Grygalashvyly, M., Berger, U., 2005, Autocatalytic water vapor production as a source of large mixing ratios within the middle to upper mesosphere, Journal of Geophysical Research (Atmospheres), 110, 15 303–+

Sonnemann, G. R., Hartogh, P., Grygalashvyly, M., Li, S., Berger, U., 2008, The quasi 5-day signal in the mesospheric water vapor concentration at high latitudes in 2003-a comparison between observations at ALOMAR and calculations, Journal of Geophysical Research (Atmospheres), 113, 4101–+

Sonnemann, G. R., Hartogh, P., Li, S., Grygalashvyly, M., Berger, U., 2009, A QBO-signal in mesospheric water vapor measurements at ALOMAR (69.29° N, 16.03° E) and in model calculations by LIMA over a solar cycle, Atmospheric Chemistry & Physics Discussions, 9, 883–903

Straub, C., 2008, Development of a 22 GHz correlating Radiometer for the observation of Stratospheric Water Vapor, Diploma, IAP Bern

Thomas, G. E., 1996, Is the polar mesosphere the miner's canary of global change, Advances in Space Research, 18, 149–158

Thomas, G. E., Olivero, J. J., DeLand, M., Shettle, E. P., 2003, Comment on "Are Noctilucent Clouds Truly a 'Miner's Canary' for Global Change?", EOS Transactions, 84, 352–353

Ulaby, F., Moore, R., Fung, A., 1981, Microwave remote sensing, Addison-Wesley Publishing Co

Villanueva, G., 2004, The High-Resolution Spectrometer for SOFIA-GREAT: Instrumentation, Atmospheric Modeling and Observations, Ph.D. thesis, Albert-Ludwigs-Universität zu Freiburg,

Vincent, R. A., Tsuda, T., Kato, S., 1988, A comparative study of mesospheric solar tides observed at Adelaide and Kyoto, Journal of Geophysical Research, 93, 699–708

Volland, H., 1988, Atmospheric Tidal and Planetary Waves, Atmospheric Sciences Library, Kluwer Academic Publishers

von Zahn, U., 2003, Are noctilucent clouds truly a "miner's canary" for global change?, EOS, 84

von Zahn, U., Berger, U., 2003, Persistent ice cloud in the midsummer upper mesosphere at high latitudes: Three dimensional modeling and cloud interactions with ambient water vapor, Journal of Geophysical Research, 108

von Zahn, U., Fiedler, J., Naujokat, B., Langematz, U., Krüger, K., 1998, A note on record-high temperatures at the northern polar stratopause in winter 1997/98, Geophysical Research Letters, 25, 4169–4172

Wang, D., Fritts, D. C., 1991, Evidence of Gravity Wave-Tidal Interaction Observed near the Summer Mesopause at Poker Flat, Alaska., Journal of Atmospheric Sciences, 48, 572–583

Waters, J. W., 1976, Absorption and emission by atmospheric gases., in Astrophysics. Part B: Radio Telescopes, pp. 142–176

Waters, J. W., Froidevaux, L., Harwood, R. S., Jarnot, R. F., Pickett, H. M., Read, W. G., Siegel, P. H., Cofield, R. E., Filipiak, M. J., Flower, D. A., Holden, J. R., Lau, G. K., Livesey, N. J., Manney, G. L., Pumphrey, H. C., Santee, M. L., Wu, D. L., Cuddy, D. T., Lay, R. R., Loo, M. S., Perun, V. S., Schwartz, M. J., Stek, P. C., Thurstans, R. P., Boyles, M. A., Chandra, K. M., Chavez, M. C., Chen, G., Chudasama, B. V., Dodge, R., Fuller, R. A., Girard, M. A., Jiang, J. H., Jiang, Y., Knosp, B. W., Labelle, R. C., Lam, J. C., Lee, A. K., Miller, D., Oswald, J. E., Patel, N. C., Pukala, D. M., Quintero, O., Scaff, D. M., Vansnyder, W., Tope, M. C., Wagner, P. A., Walch, M. J., 2006, The Earth Observing System Microwave Limb Sounder (EOS MLS) on the Aura Satellite, IEEE Transactions on Geoscience and Remote Sensing, 44, 1075–1092

Woods, T. N., Tobiska, W. K., Rottman, G. J., Worden, J. R., 2000, Improved solar Lyman α irradiance modeling from 1947 through 1999 based on UARS observations, Journal of Geophysical Research, 105, 27 195–27 216

Zhang, X., Forbes, J. M., Hagan, M. E., 2010a, Longitudinal variation of tides in the MLT region: 1. Tides driven by tropospheric net radiative heating, Journal of Geophysical Research (Space Physics), 115, 6316–+

Zhang, X., Forbes, J. M., Hagan, M. E., 2010b, Longitudinal variation of tides in the MLT region: 2. Relative effects of solar radiative and latent heating, Journal of Geophysical Research (Space Physics), 115, 6317–+